# Spectral photon-counting computed tomography in cardiovascular imaging

Salim Si-Mohamed

N°d'ordre NNT :
2020LYSE1335

**THESE de DOCTORAT DE L'UNIVERSITE DE LYON**
opérée au sein de
**l'Université Claude Bernard Lyon 1**

**Ecole Doctorale** N° 205
**Interdisciplinaire Sciences-Santé (EDISS)**

**Spécialité de doctorat** :
Génie biomédical

Soutenue publiquement le 18/12/2020 par :
**Salim Aymeric SI-MOHAMED**

---

# Spectral Photon-Counting Computed Tomography in Cardiovascular Imaging

---

Devant le jury composé de :

| | | |
|---|---|---|
| Fabien HYAFIL | Professeur, Université Paris Descartes | Rapporteur |
| Christian MOREL | Professeur, Université Aix-Marseille | Rapporteur |
| Jean-Paul BEREGI | Professeur, Université Montpellier-Nîmes | Examinateur |
| Emmanuelle CANET-SOULAS | Professeure, Université Lyon 1 | Examinatrice |
| David Peter CORMODE | Professeur, Université de Philadelphie | Examinateur |
| Hélène KOVACSIK | Professeure, Université Montpellier-Nîmes | Examinatrice |
| Philippe Charles DOUEK | Professeur, Université Lyon 1 | Directeur de thèse |
| Monica SIGOVAN | Docteure, Université Lyon 1 | Co-directrice de thèse |
| Loic BOUSSEL | Professeur, Université Lyon 1 | Co-directeur de thèse, Invité |
| Didier REVEL | Professeur, Université Lyon 1 | Invité |

# UNIVERSITE CLAUDE BERNARD – LYON 1

| | |
|---|---|
| Administrateur provisoire de l'Université | M. Frédéric FLEURY |
| Président du Conseil Académique | M. Hamda BEN HADID |
| Vice-Président du Conseil d'Administration | M. Didier REVEL |
| Vice-Président du Conseil des Etudes et de la Vie Universitaire | M. Philippe CHEVALLIER |
| Vice-Président de la Commission de Recherche | M. Jean-François MORNEX |
| Directeur Général des Services | M. Pierre ROLLAND |

## COMPOSANTES SANTE

| | |
|---|---|
| Département de Formation et Centre de Recherche en Biologie Humaine | Directrice : Mme Anne-Marie SCHOTT |
| Faculté d'Odontologie | Doyenne : Mme Dominique SEUX |
| Faculté de Médecine et Maïeutique Lyon Sud - Charles Mérieux | Doyenne : Mme Carole BURILLON |
| Faculté de Médecine Lyon-Est | Doyen : M. Gilles RODE |
| Institut des Sciences et Techniques de la Réadaptation (ISTR) | Directeur : M. Xavier PERROT |
| Institut des Sciences Pharmaceutiques et Biologiques (ISBP) | Directrice : Mme Christine VINCIGUERRA |

## COMPOSANTES & DEPARTEMENTS DE SCIENCES & TECHNOLOGIE

| | |
|---|---|
| Département Génie Electrique et des Procédés (GEP) | Directrice : Mme Rosaria FERRIGNO |
| Département Informatique | Directeur : M. Behzad SHARIAT |
| Département Mécanique | Directeur M. Marc BUFFAT |
| Ecole Supérieure de Chimie, Physique, Electronique (CPE Lyon) | Directeur : Gérard PIGNAULT |
| Institut de Science Financière et d'Assurances (ISFA) | Directeur : M. Nicolas LEBOISNE |
| Institut National du Professorat et de l'Education | Administrateur Provisoire : M. Pierre CHAREYRON |
| Institut Universitaire de Technologie de Lyon 1 | Directeur : M. Christophe VITON |
| Observatoire de Lyon | Directrice : Mme Isabelle DANIEL |
| Polytechnique Lyon | Directeur : Emmanuel PERRIN |
| UFR Biosciences | Administratrice provisoire : Mme Kathrin GIESELER |
| UFR des Sciences et Techniques des Activités Physiques et Sportives (STAPS) | Directeur : M. Yannick VANPOULLE |
| UFR Faculté des Sciences | Directeur : M. Bruno ANDRIOLETTI |

**TITRE EN ANGLAIS**

Spectral photon-counting computed tomography in cardiovascular imaging

**RESUME EN ANGLAIS**

The advent of new X-ray detectors, i.e. photon-counting detectors, introduced in spectral photon-counting computed tomography (SPCCT) systems allow analysis of the energy composition of the transmitted X-ray spectrum. By dividing the spectrum into well-chosen energy-based datasets, the specific and quantitative « multicolor » imaging of materials (such as gadolinium and gold), also known as K-edge imaging, is possible with such systems. Meanwhile, the field of nanoparticle contrast agents for CT has expanded rapidly over the past decade, with the greatest number of publications focusing on gold nanoparticles (AuNP). It turns out that AuNP are a good candidate for K-edge imaging, du to their high K-edge energy (~80.3 keV). In addition, they have the potential to circulate longer than iodinated contrast agents for improved blood pool imaging and to be highly biocompatible. The main objective of this thesis work is to evaluate *in vitro* and *in vivo* K-edge imaging using a preclinical prototype SPCCT system in combination with pegylated AuNP and clinically approved contrast agents based on iodine and gadolinium for imaging of the lumen and arterial wall in healthy and atherosclerotic rabbits. Our main contribution is to demonstrate that K-edge imaging is feasible *in vivo* in combination with AuNP to improve the specific assessment of the atherosclerotic arterial wall in comparison to conventional imaging via the quantification of its macrophage burden, as well as to perform « bicolor » imaging (i.e. simultaneous imaging of two agents) for specific differentiation between enhancement of the lumen with one iodinated contrast agent and enhancement of the aortic wall with K-edge AuNP.

**MOTS-CLES EN ANGLAIS**

Spectral Photon-Counting Computed Tomography; Photon-counting detector; K-edge imaging; Cardiovascular disease; Atherosclerosis; Contrast agent; Gold nanoparticle; Molecular macrophage imaging.

**TITRE EN FRANCAIS**

Apport de l'imagerie spectrale tomodensitométrique à comptage photonique pour l'imagerie cardiovasculaire

**RESUME EN FRANCAIS**

L'avènement de nouveaux détecteurs, dits à comptage photonique, appliqués à la tomodensitométrie aux rayons X permet l'analyse de la composition énergétique du spectre de rayons X transmis. En divisant le spectre en plusieurs fenêtres énergétiques, l'imagerie « multicouleur » spécifique et quantitative de matériaux (tels que le gadolinium et l'or), également appelée imagerie K-edge, est possible. Parallèlement, les nanoparticules d'or (AuNP) s'avèrent de bonnes candidates pour l'imagerie K-edge en raison de leur énergie K-edge élevée (~80.3 keV). De plus, elles ont le potentiel de circuler plus longtemps que les agents de contraste iodés pour une meilleure imagerie du compartiment vasculaire et d'être biocompatibles pour des applications *in vivo*. L'objectif principal de ce travail de thèse est d'évaluer l'imagerie K-edge *in vitro* et *in vivo*, permise par un prototype préclinique de tomodensitométrie spectrale à comptage photonique, en combinaison avec des AuNP pégylées et des produits de contraste approuvés cliniquement à base d'iode et de gadolinium pour l'imagerie de la lumière et de la paroi artérielle chez le lapin sain et athéromateux. Notre principale contribution a été de démontrer que l'imagerie K-edge est réalisable *in vivo* en combinaison avec des nanoparticules d'or pour améliorer l'évaluation spécifique de la paroi artérielle athéromateuse en comparaison à l'imagerie conventionnelle via la quantification de sa charge macrophagique, ainsi que pour réaliser une imagerie spécifique « bicouleur » de la lumière artérielle marquée par un produit de contraste iodé et la plaque marquée par les AuNP.

**MOTS-CLES EN FRANCAIS**

Tomodensitométrie spectrale à comptage photonique; Détecteur à comptage photonique; Imagerie K-edge; Maladie cardiovasculaire; Athérosclérose; Agent de contraste; Nanoparticule d'or; Imagerie moléculaire macrophagique.

**INTITULE ET ADRESSE DU LABORATOIRE**

Université de Lyon, CREATIS ; CNRS UMR5220 ; Inserm U1044 ; INSA-Lyon ; Université Lyon 1, 7 Av. Jean Capelle, 69621 VILLLEURBANNE, France.

**TABLE OF CONTENTS**

# French Summary

La tomodensitométrie (TDM) aux rayons X a fait l'objet de nombreux développements technologiques au cours de ces 20 dernières années avec notamment le développement des systèmes multibarettes de TDM et des modes de reconstruction itérative. Plus récemment, l'apparition des systèmes de TDM double énergie a permis une exploitation dite spectrale des informations contenues dans le spectre des rayons X après leurs interactions avec la matière. La TDM spectrale est en train de franchir une nouvelle étape grâce au développement de nouveaux détecteurs dits à comptage photonique équippant des systèmes TDM dits spectraux à comptage photonique ("Spectral Photon-Counting Computed Tomography" ou SPCCT en anglais) actuellement au stade de recherche et de développement. Ces derniers, outre de permettre une amélioration substantielle de la résolution spatiale et une diminution des doses de rayons X, sont capables de résoudre spécifiquement l'énergie des photons et de les compter individuellement permettant de mettre en évidence des phénomènes jusqu'à alors non accessibles avec les détecteurs à intégration équippant les systèmes de TDM standard et à double énergie. Le comptage de photons permet dès lors la reconstruction d'une imagerie spécifique et quantitative d'un atome, dite au K-edge, dont les perpectives et le potentiel sont de permettre une imagerie moléculaire "froide", en utilisant un rayonnement X et des agents de contraste non radioactifs contrairement à l'imagerie "chaude" en médecine nucléaire.

Les maladies cardiovasculaires représentent la principale cause de mortalité dans les pays développés. Leur prise en charge nécessite l'utilisation de modalités d'imagerie non invasive capables d'aider à leur prévention, leur diagnostic et leur traitement tout en combinant une imagerie rapide, adaptée et accessible comme l'est la TDM dans de nombreuses applications cardiovasculaires. Cependant, outre l'apport morphologique bien reconnu de la TDM grâce à sa haute résolution spatiale et sa rapidité d'acquisition, celle-ci ne permet pas en clinique une imagerie spécifique moléculaire ou cellulaire des phénomènes physiopathologiques notamment impliqués dans l'athérosclérose, contrairement à l'IRM ou encore mieux la TEP-TDM. Ceci est principalement expliqué par la plus faible sensibilité de la TDM et l'absence de spécificité des agents de contraste iodés contrairement à l'IRM et la TEP-TDM avec respectivement l'utilisation d'agents de contraste à base de nanoparticules superparamagnétiques d'oxyde de fer (USPIO) ou le 18 fluoro-désoxy-glucose (FDG) par exemple.

Tandis que les agents de contraste iodés et gadolinés, non dénués d'effets secondaires, sont utilisés cliniquement au quotidien en TDM et en IRM, de nouveaux agents de contraste dérivés des nanobiotechnologies font actuellement l'objet de développements leur permettant

d'être candidats à l'imagerie TDM spectrale à comptage photonique. Le principe en est de permettre l'inclusion au sein de nanoparticules de nombreux atomes à numéro atomique élevé, c'est-à-dire à forte contribution spectrale, afin de permettre une imagerie spécifique et quantitative grâce à l'atténuation au K-edge de ces atomes. Malgré les actuelles limites physiques liées à la sensibilité encore faible des détecteurs à comptage photonique et biochimiques liées à la difficulté d'obtenir une forte concentration d'atomes dans une nanoparticule de petite taille, nous avons exploré les potentialités diagnostiques de l'imagerie TDM spectrale à comptage photonique moléculaire en particulier par des études *in vitro* et *in vivo* chez l'animal.

C'est par une démarche de recherche translationelle appliquée à l'athérosclérose accompagnant les développements technologiques en imagerie TDM spectrale à comptage photonique que s'inscrivent les travaux présentés dans la thèse. L'objectif a été le développement et la caractérisation de l'imagerie K-edge permise par un prototype de TDM spectrale à comptage photonique à usage préclinique en combinaison avec des agents de contraste dédiés à l'évaluation de la lumière artérielle et de la charge macrophagique dans l'athérosclérose.

Cette thèse débute par un chapitre d'introduction générale intégrant un travail de revue de la technologie [1] et des applications cardiovasculaires suivi par l'exposé de la recherche effectuée. Les travaux sont présentés de manière consécutive tel que l'a été le déroulement de la thèse, débutant par les études de faisabilité et d'évaluation de l'imagerie K-edge acquise à partir d'un prototype expérimental préclinique *in vitro* [2], puis *in vivo* sur modéles animaux sains [3, 4] et athéromateux [5]. Trois autres travaux annexes sont associés à la thèse pour documenter la recherche [6–8].

Le premier chapitre de la thèse est structuré en 2 parties. La première partie présente l'état actuel de la technologie, ses principes, avantages et limites. La deuxième partie propose des perspectives de recherche et d'application en imagerie cardiovasculaire illustrées par des travaux annexes à la thèse publiés et/ou présentés lors de congrés s'intégrant dans la problématique du projet européeen SPCCT H2020, ainsi que par l'expérience d'autres équipes et constructeurs.

Les détecteurs à comptage photonique (PCD en anglais pour Photon Counting Detectors) initalement utilisés en médecine nucléaire sont actuellement développés dans le domaine des

rayons X, radiographie et tomodensitométrie, et ont pour but d'améliorer les principales limites majeures des actuels détecteurs dits à intégration (EID en anglais pour Energy Integrating Detectors): (A) un contraste insuffisant des tissus mous, (B) une imagerie non spécifique des tissus, (C) une relative haute dose de rayons X des procédures actuelles, (D) une valeur des pixels basée sur l'échelle de gris des images TDM, qui est le reflet de l'atténuation linéaire des tissus, apportant une information peu spécifique.

L'architecture des PCDs comprend un composant semi-conducteur d'une épaisseur de 2 à 3 mm absorbant l'énergie utilisée en TDM, c'est-à-dire entre 20 et 140keV. Les détecteurs sont assemblés en une couche présentant des anodes pixélisées. Les détecteurs sont fabriqués à partir soit de Cadmium Telluride (CdTe), soit Cadmium Zinc Telluride (CZT), soit Silicium (Si), des matériaux également retrouvés dans les détecteurs à intégration. Cependant dans les PCDs, cette couche d'anode est reliée et connectée à un circuit intégré (en anglais ASICs pour Application-Specific Integrated Circuit). Ce dernier est composé de canaux montés en parallèle qui vont successivement amplifier le signal, modéliser l'impulsion, comparer et classer les énergies en fonction des fenêtres énergétiques du système. Ces détecteurs ont la capacité de discrimination énergétique basée sur l'analyse de l'énergie des photons recueillis, par l'intermédiaire de la mesure de hauteur d'une "impulsion" ("pulse" en anglais), cette dernière étant le résultat de l'interaction entre le photon transmis et le semi-conducteur constituant les PCDs, via le phénomène de création de paires électron-trou. Ainsi ces détecteurs comptent le nombre de photons transmis, les classant dans deux à huit fenêtres énergétiques en fonction des constructeurs (cinq disponibles avec le systéme utilisé dans les travaux de la thèse). Cependant, la performance de ces détecteurs n'est pas parfaite compte tenu du nombre important de photons recueillis (*"count rate"*) en TDM ce qui pourra expliquer des imperfections de discrimination et de quantification spectrale.

Parmi les avantages de l'imagerie TDM spectrale à comptage photonique particulièrement avancés dans la thèse :

**A) amélioration de la résolution spatiale** permise grâce à la taille des pixels des PCD de l'ordre de 0,2-0,5 mm, contrastant avec la taille élémentaire des détecteurs à intégration de l'ordre de 0,6 mm-1,4 mm. Cette caractéristique technologique est nécessaire afin de pallier au flux important des photons retrouvé en TDM (de l'ordre de $10^{6 \text{ à } 7}$ $s^{-1}$/ $mm^{-2}$ pour l'imagerie thoracique par exemple).

**B) imagerie dite au K-Edge**, véritable signature physique d'un atome permettant une imagerie spécifique et quantitative d'un élément basée sur son énergie K-edge,. Le K-edge représente l'énergie de liaison d'un électron de la couche électronique K avec le noyau d'un

atome. Les photons ayant une énergie égale à celle de l'énergie K-edge seront fortement atténués, créant ainsi un pic d'atténuation spécifique d'un élément que les PCDs seront capables de discriminer. De la même façon, des pics d'atténuation correspondants aux couches L, M seront présents dans le spectre détecté mais à des énergies beaucoup plus basses ne permettant pas une discrimination optimale en imagerie clinique. Dans le corps humain, les photons de basse énergie sont absorbés par les premiers centimètres des tissus et il n'est donc possible de mettre en évidence que les photons de haute énergie. Ainsi des atomes à K-edge élevé, comme le Gadolinium, l'Or, l'Ytterbium, le Platinum pourront être étudiés à l'aide de cette technologie innovante. A noter que l'Iode présente une énergie K-edge trop basse (33.3 keV) pour être observable en TDM à comptage photonique clinique contrairement aux sytèmes dédiés pour le petit animal ou pour la mammographie. De plus, les PCDs offrent la possibilité de quantifier le nombre de photons correspondant à une énergie K-edge spécifique d'un matériel.

**C) imagerie multi-contraste**, se définissant comme une imagerie spécifique et quantitative différentiant deux (imagerie dite bi-couleur) ou plusieurs agents (imagerie dite multi-couleur) de contraste au sein d'un même tissu et même voxel. Celle-ci est rendue possible par le système de détection des PCDs capable de discriminer plusieurs énergies K-edge simultanément et par conséquent capable de détecter les différents atomes correspondants.

Le deuxième chapitre est consacré à démontrer la faisabilité *in vitro* de l'imagerie spécifique mono-contraste (dite mono-couleur) et multi-contraste (dite multi-couleur) de deux produits de contraste approuvés pour l'usage clinique (à base d'iode et gadolinium) et d'une nanoparticule pégylée à base d'or. L'objectif de cette étude a été d'évaluer tout d'abord les performances de discrimination qualitative et de quantification du prototype pour chaque agent de contraste dans des tubes de concentration croissante; puis par un mélange de deux agents de contraste dans des tubes de concentration variable avec comme pre-requis une atténuation globale identique dans les différents tubes. La reconstruction de chaque matériaux basée à partir des effets photo-électrique, Compton et K-edge a été réalisée par une décomposition soit en deux bases pour l'iode (eau, iode), soit trois bases pour l'or ou le gadolinium (eau, iode, agent K-edge), soit quatre bases pour l'or et le gadolinium simultanément (eau, iode, gadolinium, gold). Il est à noter que le modéle de décomposition inclut systématiquement deux bases non dépendantes de l'effet K-edge comme l'eau et l'iode ou l'effet photoélectrique et Compton et qu'en fonction des agents K-edge présents il sera rajouté leurs bases respectives. Nous avons ainsi évalué la précision de quantification, le

bruit, le contraste-à-bruit et la cross-contamination (définie comme la présence du signal d'une base dans une image d'une autre base) pour ces différents atomes dans des paramètres d'acquisition et de reconstruction fixes (acquisition axiale, 120 kVp, 100 mAs; taille du pixel 0,4 x 0,4 mm, épaisseur de coupe à 2 mm, filtre gaussian avec un rayon et sigma à 2 pixels). Les résultats de cette étude ont démontré la haute précision de quantification des trois agents de contraste (coefficient de détermination $R^2$>0.98). On notait cependant une légère sous-estimation pour les agents de contraste K-edge (or, gadolinium) isolément, ainsi qu'une cross-contamination des agents K-edge dans les images d'iode. Ces effets étaientt accentués lors de la décomposition en quatre bases pour la quantification des mixtures d'or et de gadolinium ce qui certainement expliqué par une statistique de photons plus faible et un modéle spectral moins adapté comparativement à la décomposition en deux ou trois bases. Toutefois seule l'imagerie K-edge permettait une évaluation spécifique des agents K-edge ne recueillant de signal ni au sein du fantôme (fait de polyoxyméthylène) ni au sein des tubes contrôles (solution aqueuse). Les contrastes-à-bruit ("contrast-to-noise ratio" ou CNR) pour 1 mg/mL d'atomes par produit de contraste étaient plus élevés consécutivement pour l'iode ($CNR_{Iodine}$ = 3.45), le gadolinium ($CNR_{Gd}$ = 3.11) et l'or ($CNR_{Gold}$ = 2.80) séparément puis l'iode et gadolinium mixés ($CNR_{Iodine}$ = 3.20, $CNR_{Gd}$ = 2.80) que l'or et le gadolinium mixés ($CNR_{Gd}$ = 1.67, $CNR_{Gold}$ = 1.37) permettant d'en déduire des seuils de sensibilité consécutivement plus élevés pour l'iode (0.58 mg/mL), le gadolinium (0.64 mg/mL) et l'or (0.71 mg/mL) pour un CNR à 2, et ce, dans les conditions d'acquisition et de reconstruction utilisées. La faisabilité de l'imagerie K-edge avec un agent de contraste approuvé en clinique (à base de gadolinium) et avec des nanoparticules à base d'or a ainsi été montré par cette évaluation. La sensibilité du prototype était cependant limitée liée à une chaine de detection encore imparfaite mais présentant des performances autorisant l'utilisation *in vivo* chez le petit et moyen animal. En parallèle et s'inscrivant toujours dans la problématique de sensibilité de l'imagerie K-edge, nous avons évalué d'autres agents de contraste candidats à l'imagerie K-edge dans le cadre d'une collaboration avec l'équipe de David Cormode de l'Université de Philadelphie [6]. Les résultats ont mis en évidence une sensibilité variable des atomes en fonction de l'énergie du spectre incident et plus élevée pour les atomes à énergie K-edge proche de 60 keV en raison d'un flux de photons plus important autour de cette énergie lié au spectre du tube à rayons X de voltage fixe à 120 kVp. L'Ytterbium (K-edge : 61.3 keV) présentait notamment la plus forte sensibilité en imagerie K-edge. Cette étude permettait ainsi de mettre en évidence l'intérêt d'optimisation des protocoles d'acquisition aux agents de contraste ciblés. Le deuxième résultat important était la présence d'imperfections du modéle

spectral et du bruit dans les images, ouvrant la voie aux développements méthodologiques dans le domaine de la reconstruction du signal. Dans ce cadre, une collaboration avec l'équipe quatre du laboratoire CREATIS (Cyril Mory, Simon Rit, Bruno Sixou) a permis d'évaluer et mettre en place une méthode de reconstruction spectrale dite "one-step" générant directement des cartes matériaux à partir des comptes de photons bruts [8].

Le troisième chapitre regroupe trois travaux d'imagerie TDM spectrale à comptage photonique *in vivo* chez le lapin, tous trois en combinaison avec les nanoparticules pégylées à base d'or. Le choix s'est porté sur les nanoparticules d'or compte-tenu de la faisabilité *in vitro* de l'imagerie K-edge de l'or avec de bonnes performances qualitatives et quantitatives ainsi que des propriétés de biocompatibilité et de biodistribution des nanoparticules d'or.

Le premier travail est une preuve de concept de l'imagerie statique et dynamique mono-couleur et multi-couleur au cours de l'injection successive de nanoparticules d'or puis d'un produit de contraste iodé par voie intraveineuse. La différentiation entre les deux agents de contraste est basée sur la décomposition en matériaux en trois bases (eau, iode, K-edge de l'or). L'analyse qualitative et quantitative de la biodistribution de chaque agent de contraste a été réalisée de manière successive dans plusieurs organes d'intérêts, et comparée à celle attendue des deux agents de contraste. Dans le cas des nanoparticules d'or, nous avons démontré l'effet de rémanence vasculaire dit de "blood pool" spécifique (pas de signal provenant des autres tissus) et quantitative (quantification des concentrations en mg/mL), comme en témoignaient les concentrations stable dans le compartiment sanguin au cours des premières heures. Ce phénomène est principalement expliqué par la pégylation des nanoparticules les protégeant de la phagocytose immédiate macrophagique mais aussi par leur taille à 18 nm (diamètre hydrodynamique) expliquant l'absence d'excrétion rénale au cours du temps (seuil critique autour des 5.5 nm sans compter l'impact du coating). Dans le cas du produit de contraste iodé, nous avons suivi sa biodistribution vasculaire et interstitielle au sein des organes d'intérêts, ainsi que son élimination rénale tout en détectant simultanément et spécifiquement la présence de nanoparticules d'or. L'imagerie de l'iode a confirmé par ailleurs l'absence de discrimination des éléments de numéro atomique intermédiaire comme le calcium (Z=20) et donc l'intérêt de la spécificité apportée par l'utilisation d'un agent K-edge. Ce travail a permis enfin de mettre en évidence la faisabilité de l'imagerie bi-couleur pour l'angiographie avec une résolution temporelle adaptée à l'imagerie vasculaire (0.75 secondes d'acquisition avec un délai de 2 secondes entre chaque acquisition) confirmant le potentiel pour l'imagerie de la lumière artérielle.

Le second travail consiste en un suivi longitudinal sur six mois en imagerie K-edge de la biodistribution des nanoparticules d'or chez le lapin en comparaison avec la méthode de référence quantitative *ex vivo* à la fin du suivi (spectrométrie de masse). Au cours des imageries successives, l'imagerie K-edge a permis de mettre en évidence une biodistribution au sein des organes du système réticulo-endothélial (foie, rate, moelle osseuse, ganglion), et ce, de manière non décelable sur l'imagerie conventionnelle au sein de la moelle osseuse du fait de la présence de l'os masquant leur présence, confirmant sa spécificité. Les résultats en microscopie électronique ont confirmé la présence des nanoparticules quasi-exclusivement dans les macrophages du système réticulo-endothélial. Il n'a pas été noté de nanoparticules dans les échantillons réalisés dans un grand nombre d'organes (cerveau, rein, coeur) ni de manière libre au sein de l'espace extracellulaire. La comparaison entre la quantification en imagerie K-edge et la quantification en spectrométrie de masse sur les organes *ex vivo* a démontré une bonne corrélation linéaire (coefficient de détermination $R^2$ = 0.93) avec un biais de mesure faible (0,11 mg/mL sur l'analyse Bland-Altman). L'or était cependant sous-estimée en imagerie K-edge : ceci peut être expliqué soit par une sous-estimation systématique du modéle spectral soit par une limite de la comparaison de tissus *ex vivo* et de la mesure *in vivo*. Ces résultats permettent de valider ainsi la faisabilité de l'imagerie K-edge à l'échelle cellulaire, c'est à dire de détecter, caractériser et quantifier un processus à l'échelle d'une cellule, ici le macrophage. Se servant de l'imagerie TDM spectrale à comptage photonique, nous avons par ailleurs prolongé ce travail par le suivi de nanoparticules à base d'autres atomes à haut numéro atomique dans le cadre du projet européeen SPCCT H2020 en collaboration avec d'autre biochimistes du consortium (études non présentées dans la thèse).

L'ensemble des connaissances acquises au cours des premières années de la thèse nous a permis d'évaluer l'imagerie K-edge en combinaison avec les nanoparticules d'or au sein de la plaque d'athérosclérose *in vivo* chez un modéle de lapin athéromateux dans le dernier travail présenté. L'hypothèse principale était de pouvoir démontrer par une imagerie spécifique et quantitative des nanoparticules d'or, phagocytées par les macrophages, la charge macrophagique de la plaque d'athérosclérose connue pour être un facteur de risque de vunérabilité et de rupture de la plaque. Nous avons réalisé des acquisitions SPCCT répétées et des reconstructions au K-edge de l'or sur un modèle de lapin athéromateux au cours des deux premiers jours après injection intraveineuse des nanoparticules. Le choix du modéle d'athérosclérose s'est porté sur le lapin mâle athéromateux de souche New Zealand White compte tenu des niveaux d'Apo B et d'une activité de la protéine de transfert du cholestérol estérifié élevée (CETP) comparable à l'homme, de la forte proportion de macrophages

spumeux au sein des plaques d'athérosclérose, de la taille de l'aorte similaire à celle d'une artère coronaire humaine, de la taille de l'animal, de la littérature abondante portant sur ce modéle et de la maîtrise du modèle que j'ai acquise pendant la thèse. Du fait de la faible concentration de cholestérol total dans le plasma et que le HDL soit la lipoproteine prédominante, le lapin NZW ne développe pas de lésion spontanée (contrairement au lapin génétiquement modifié de type Watanabe Heritable Hyper Lipidemic par exemple). Seule la combinaison d'un régime riche en cholestérol et d'une angioplastie de l'aorte pour une durée totale du modéle de douze semaines permet la mise en place de plaque riche en dépôt lipidiques, avec accumulation de macrophages spumeux et la développement d'une fibrose myointimale diffuse. Dans le cadre de notre travail, nous avons fait le choix de prolonger la durée totale du modéle au-delà de douze semaines afin de favoriser la présence de calcifications pariétales, comme fréquemment retrouvées au sein des plaques d'athérosclérose. L'évaluation du modéle avant injection de produit de contraste a mis en évidence la charge calcique étendue le long de l'aorte confirmant la réussite du modéle. L'imagerie après injection des nanoparticules et au cours du suivi longitudinal sur deux jours a mis en évidence un signal détectable en imagerie K-edge dès le premier jour puis plus important au deuxième jour, permettant la quantification des nanoparticules d'or au sein de la plaque. La comparaison de la concentration en or avec la surface des macrophages mesurée en immunohistochimie a mis en évidence une meilleure corrélation et précision avec l'imagerie K-edge contrairement à l'imagerie conventionnelle. Ce résultat est expliqué par la présence des calcifications qui se rajoutent en imagerie conventionnelle à l'atténuation liée aux nanoparticules d'or surestimant ainsi la charge macrophagique. Cet effet a bien été mis en évidence dans certaines plaques d'atténuation élevée mais de concentration en or faible en imagerie K-edge, confirmée par l'analyse immunohistochimique de la charge macrophagique. La confrontation de ces résultats à l'histologie, au marquage immunohistochimique des macrophages, à la microscopie électronique, à la spectroscopie à rayons X à dispersion d'énergie et à la spectrométrie de masse a permis de confirmer la présence de plaque athéromateuses, la présence d'une charge macrophagique importante répartie principalement proche du coeur lipidique dans l'intima, le présence de nanoparticules d'or au sein des macrophages spumeux et la présence en quantité importante de nanoparticules dans le tissu aortique *ex vivo*. La dernière étape de ce travail a été de réaliser une imagerie bicouleur de la lumière vasculaire via l'injection d'un produit de contraste iodé simultanément avec l'imagerie moléculaire de la plaque d'athérosclérose. Les résultats de cette imagerie bicouleur ont permis la visualisation simultanée anatomique du remodelage anévrismal de l'aorte combinée à la

détection de la charge macrophagique dans la paroi vasculaire. Ce travail a permis ainsi de mettre en évidence la faisabilité de l'imagerie K-edge contrairement à l'imagerie conventionnelle pour l'évaluation des mécanismes inflammatoires de la plaque d'athérosclérose via la quantification indirecte de la charge macrophagique et le potentiel élevé de cette modalité pour une approche complète anatomique et pathophysiologique par l'imagerie des maladies cardiovasculaires. Ce travail cloture ainsi la thèse et apporte de nombreuses perspectives et voies de recherche dans ce domaine.

Cette thèse a été réalisée au sein du Laboratoire CREATIS, Université Lyon 1, dans le cadre d'un projet Européen H2020, "SPCCT" coordonné par le directeur de la thèse, professeur Philippe Douek (http://www.spcct.eu/). Les travaux expérimentaux ont été réalisés au sein de la plateforme d'imagerie du vivant CERMEP sur le site de BRON. Les nanoparticules d'or ont été développées, synthétisées et fournies dans le cadre d'une collaboration avec l'Université de Philadelphie (sous la direction de David Cormode, professeur associé).

**REFERENCES**

1. Si-Mohamed S, Bar-Ness D, Sigovan M, et al (2017) Review of an initial experience with an experimental spectral photon-counting computed tomography system. Nucl Instrum Methods Phys Res Sect Accel Spectrometers Detect Assoc Equip. https://doi.org/10.1016/j.nima.2017.04.014

2. Si-Mohamed S, Tatard-Leitman V, Laugerette A, et al (2019) Spectral Photon-Counting Computed Tomography (SPCCT): in-vivo single-acquisition multi-phase liver imaging with a dual contrast agent protocol. Sci Rep 9:8458. https://doi.org/10.1038/s41598-019-44821-z

3. Cormode DP, Si-Mohamed S (first author with equal contribution), Bar-Ness D, et al (2017) Multicolor spectral photon-counting computed tomography: in vivo dual contrast imaging with a high count rate scanner. Sci Rep 7:4784. https://doi.org/10.1038/s41598-017-04659-9

4. Si-Mohamed S, Cormode DP, Bar-Ness D, et al (2017) Evaluation of spectral photon counting computed tomography K-edge imaging for determination of gold nanoparticle biodistribution in vivo. Nanoscale 9:18246–18257. https://doi.org/10.1039/c7nr01153a

5. Si-Mohamed SA, Sigovan M, Hsu JC, et al (2020) In vivo molecular K-edge imaging of vulnerable atherosclerotic plaque using spectral photon-counting CT. Radiol. Rev.

6. Kim J, Bar-Ness D, Si-Mohamed S, et al (2018) Assessment of candidate elements for development of spectral photon-counting CT specific contrast agents. Sci Rep 8:12119. https://doi.org/10.1038/s41598-018-30570-y

7. Sigovan M, Si-Mohamed S, Bar-Ness D, et al (2019) Feasibility of improving vascular imaging in the presence of metallic stents using spectral photon counting CT and K-edge imaging. Sci Rep 9:19850. https://doi.org/10.1038/s41598-019-56427-6

8. Mory C, Sixou B, Si-Mohamed S, et al (2018) Comparison of five one-step reconstruction algorithms for spectral CT. Phy Med Bio. https://doi.org/10.1088/1361-6560/aaeaf2

# Outline of the thesis

A state of the art introductory chapter is followed by the research work presented in two chapters written as published manuscripts (the first four studies) or submitted for publication (the last study) in scientific journals.

The first part of the introductory chapter will present the technical aspects and principles of multi-energy CT imaging, from dual energy to photon counting technology[1]. The second part is an overview of the potential of SPCCT in the field of cardiovascular imaging.

The research work studies are organized on two chapters.

The first chapter presents the results of an *in vitro* study [2]. The goal was to evaluate the feasibility of monocolor and multicolor imaging in order to detect and quantify different mixed contrast agents using a SPCCT system. Three contrast agents (iodine, gadolinium and gold based) distributed in tubes with mixtures of varying proportions were tested by reconstructing the specific images of each material, i.e. based on a two basis material decomposition (MD) for iodine, three basis MD for gadolinium or gold with or without iodine, and four basis MD for gadolinium and gold. We analyzed the accuracy of quantification, the contrast-to-noise ratios (CNR) relative to a PBS tube and the cross-contamination measured for each material as the root mean square errors (RMSE) of its concentration in the other material images, where no signal was expected. The mixtures were prepared such that the solutions could not be differentiated in conventional images. However, distinction was observed in the material images within the same samples, and the measured and prepared concentrations were strongly correlated ($R^2$ values $\geq$ 0.97, 0.81 $\leq$ slope $\geq$ 0.95, - 0.68 $\leq$ offset $\leq$ 0.89 mg/mL). Cross-contamination in the iodine images for the mixture of gold and gadolinium contrast agents (RMSE = 0.3 mg/mL). CNR for 1 mg/mL of contrast agent were better for the mixture of iodine and gadolinium ($CNR_{Iodine}$ = 3.2, $CNR_{Gd}$ = 2.8) than gold and gadolinium ($CNR_{Gd}$ = 1.7, $CNR_{Gold}$ = 1.4). In conclusion, this study confirms that SPCCT enables multicolor quantitative imaging *in vitro* but with some imperfections probably due to inaccuracies in the spectral model in particular in presence of two K-edge basis. These outcomes can be explained by the fact that including more components in the material decomposition process means more degrees of freedom for the maximum likelihood algorithm, leading to smaller signal per component, and therefore more noise and more noise induced bias. Altogether, there is room for quantification improvements as well as more accurate

models and further noise handling algorithms. In that framework, a collaboration with another team (Cyril Mory, Simon Rit, Bruno Sixou) has allowed the developement of a one-step algorithm that would mitigate the noise by using iterative regularization both in the material decomposition process and in the reconstruction process [3].

The second chapter presents the results of three *in vivo* studies [4–6].

The first study is a proof-of-concept that demonstrated for the first time the ability of a spectral photon-counting computed tomography system to simultaneously discriminate and quantify a blood pool agent (Au-NP) from an iodinated contrast agent, tissue, and calcium-rich matter on scans of phantoms and in rabbits. In this study, a dynamic imaging protocol (an axial acquisition each 2 seconds during 30 seconds) for angiography has been made feasible pointing to the interest for the morphologic evaluation of coronary artery diseas, e.g. lumen stenosis.

The second study evaluated the capabilities of the SPCCT scanner to quantify over 6 months the biodistribution of gold nanoparticles. The SPCCT system allowed repetitive and quick acquisitions *in vivo*, and follow-up of changes in the AuNP biodistribution over time. Measurements performed on gold images correlated with the inductively coupled plasma-optical emission spectrometry measurements in the organs of interest (slope = 0.77, intercept = 0.47, RMSE = 0.72, $R^2$ = 0.93). TEM agreed with the imaging and ICP-OES in that much higher concentrations of AuNP were observed in the liver, spleen, bone marrow and lymph nodes (mainly in macrophages). In conclusion, we demonstrated that the SPCCT is capable of repetitive and non invasive determination of the biodistribution of gold nanoparticles. Furthermore, we detected and quantified AuNP that accumulated in the mononuclear phagocyte system. This finding oprens the way for the macrophage burden imaging in atherosclerotic plaques.

The advances in knowledge, the developed tools in our previous works and the control of the atherosclerotic animal model allowed us to set the basis for the third study. The goal was to perform K-edge imaging in combination with AuNP to detect and quantify the macrophage burden within atherosclerotic aortas of rabbits. Macrophage burden is recognized as an important factor in the risk of atherosclerotic plaque rupture. Unlike conventional CT imaging, gold K-edge imaging in presence of PEG-coated gold nanoparticles shows greater specificity and quantifiability of the atherosclerotic plaque macrophage burden despite the presence of calcifications, confirming the possibility for K-edge SPCCT molecular imaging of inflammation

in atherosclerosis. These findings were confirmed by histological and electron microscopy studies. In addition, high resolution "bicolor imaging" enabled only by K-edge SPCCT imaging shows the feasibility to image simultaneously plaque inflammation and its consequence on coronary arteries lumen size, paving the way for diagnoses of coronary arteries with high risk atherosclerotic plaque rupture, using SPCCT.

This thesis was carried out within the CREATIS Laboratory, Université Lyon 1, within the framework of a European H2020 project, “SPCCT project”. The experimental work was carried out within the CERMEP platform on the BRON site. The gold nanoparticles were developed, synthesized and supplied by the University of Philadelphia in collaboration with David Cormode, associate professor.

**REFERENCES**

1. Si-Mohamed S, Bar-Ness D, Sigovan M, et al (2017) Review of an initial experience with an experimental spectral photon-counting computed tomography system. Nucl Instrum Methods Phys Res 873:27–35. https://doi.org/10.1016/j.nima.2017.04.014

2. Si-Mohamed S, Bar-Ness D, Boussel L, Douek P (2018) Multicolor imaging with SPCCT: an in vitro study. Eur Radiol Exp 1

3. Mory C, Sixou B, Si-Mohamed S, et al (2018) Comparison of five one-step reconstruction algorithms for spectral CT. Phys Med Biol 63:235001. https://doi.org/10.1088/1361-6560/aaeaf2

4. Si-Mohamed S, Cormode DP, Bar-Ness D, et al (2017) Evaluation of spectral photon counting computed tomography K-edge imaging for determination of gold nanoparticle biodistribution in vivo. Nanoscale 9:18246–18257. https://doi.org/10.1039/c7nr01153a

5. Cormode DP, Si-Mohamed S (first author with equal contribution), Bar-Ness D, et al (2017) Multicolor spectral photon-counting computed tomography: in vivo dual contrast imaging with a high count rate scanner. Sci Rep 7:4784. https://doi.org/10.1038/s41598-017-04659-9

6. Si-Mohamed S, Sigovan M, Hsu J. et al (2020) K-edge specific non-invasive macrophage spectral photon counting CT imaging in atherosclerosis using PEGylated gold nanoparticles. Radiology. Under review.

# Chapter I

# I. SPECTRAL PHOTON-COUNTING CT TECHNOLOGY

**Title: Review of an initial experience with an experimental spectral photon-counting computed tomography system**

S. Si-Mohamed[1,2], D. Bar-Ness[2], M.Sigovan[2], D.P. Cormode[3], P. Coulon[4], E. Coche[5], A. Vlassenbroek[5], G. Normand[6], L. Boussel[1,2], P. Douek[1,2]

1. Radiology Department, Hospices Civils de Lyon, France.
2. University Claude Bernard Lyon 1, CREATIS, CNRS UMR 5220, INSERM U1206, INSA-Lyon, France
3. Department of Radiology, University of Pennsylvania, Philadelphia, PA, USA.
4. CT Clinical Science, Philips, Suresnes, France.
5. Department of Radiology, Clinique Universitaire Saint Luc, Bruxelles, Belgique
6. Department of Nephrology, Hospices Civils de Lyon, France.

## ABSTRACT

Spectral photon-counting CT (SPCCT) is an emerging X-ray imaging technology that extends the scope of available diagnostic imaging tools. The main advantage of photon-counting CT technology is better sampling of the spectral information from the transmitted spectrum in order to benefit from additional physical information being produced during matter interaction, including photo-electric and Compton effects, and the K-edge effect. The K-edge, which is specific for a given element, is the increase in X-ray absorption of the element above the binding energy between its inner electronic shell and the nucleus. Hence, the spectral information contributes to better characterization of tissues and materials of interest, explaining the excitement surrounding this area of X-ray imaging. Other improvements of SPCCT compared with conventional CT, such as higher spatial resolution, lower radiation exposure and lower noise are also expected to provide benefits for diagnostic imaging. In this review, we describe the principles and technical aspects of multi-energy CT imaging, from dual energy to photon counting technology.

## I.1. Principles

Computed tomography (CT) is currently one of the key imaging modalities in clinical use. The number of CT scans performed worldwide per year is now numbered in the hundreds of millions [1]. It is available in standard and emergency settings nearly everywhere in the world, with applications in the diagnosis of many different conditions and injuries. It provides three-dimensional images of the linear attenuation coefficient distribution within a patient, accurately delineating organs and tissue. However, there are five major limitations to current CT technologies with current contrast agents:1) Spatial resolution (around 0.5 mm), even if better than other non-invasive technologies such as MRI or PET, is still a limitation for assessment of small structures such as the lumens of coronary arteries and atherosclerotic plaques. 2) Contrast between different tissues or materials is often insufficient, especially for soft tissue, because CT images are not tissue-type specific. Indeed different tissue types often have similar attenuation values.3) X-ray attenuation measured by CT and expressed in Hounsfield Units (HU) does not allow an absolute quantification of the contrast agent injected, e.g. iodine, since it combines the attenuation of the contrast material to be quantified and the attenuation of the underlying tissue. Furthermore, the attenuation of a material depends on the energy of the X-rays spectrum used.4) CT scanning is a relatively high radiation-dose procedure. In general, its use is therefore mostly for diagnostic imaging and is limited for screening of large populations or repeated examinations in the presence of a chronic disease.5) Iodine-based contrast agents currently in use are not specific and thus do not detect or monitor pathologic processes in patients in a targeted fashion. These limitations impair the diagnostic performance of CT in all medical fields where CT is applied.

A recent, notable development in the field of CT is the analysis of spectral information of the X-rays that have passed through the subject. Although this concept has been discussed since CT was invented [2–4], the technology to accurately record this information has only become available over the past decade. Conventional CT scanners integrate all the signals from the detected transmitted X-ray photons into a single attenuation signal without recording any information on their individual energies (Fig 1A). A variety of systems that are given the term dual-energy CT (DECT) and use energy-integrating detectors (EIDs) have been introduced clinically that begin to exploit the benefits of spectral detection by acquiring two energetically distinct datasets (Fig 1B,C). Nevertheless, DECT systems do not typically have improved spatial

resolution compared to single energy CT scanners, which is still limited by the scintillators used to convert photons into light that spread the signal spatially, and by the noise resulting from the signal integration process and the associated detection electronics. Furthermore, DECT systems only perform a two-point analysis of the X-ray attenuation, which improves tissue characterization and allows quite precise iodine quantification, but is insufficient to accurately discriminate between iodine and calcium, especially at low radiation dose. In addition, many DECT systems expose the patient to two energy beams that can result in potentially high radiation exposure, and motion can create issues for aligning the two datasets. Finally, no specific contrast agent has been developed for DECT due to the lack of sensitivity of such systems for specific material imaging [5].

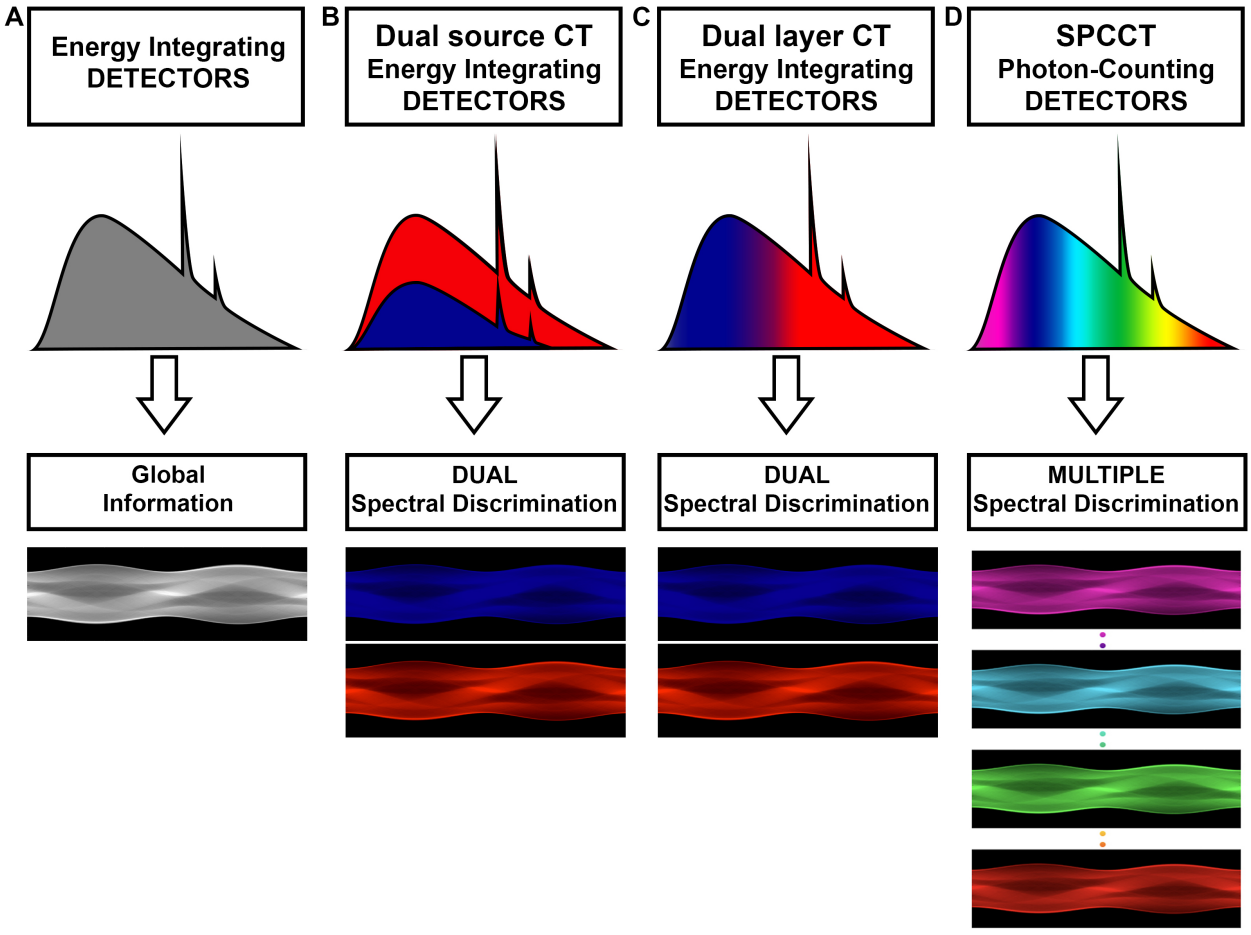


**Figure 1**. Representation of the information provided by the energy integrating detectors in single energy CT systems (A), dual source DECT systems (B) and dual-layer detector based

DECT systems (C), compared to SPCCT systems that allow several datasets to be derived from a transmitted spectrum (D).

Recently, systems based on photon counting detectors (PCDs), termed spectral photon-counting detectors CT (SPCCT) or multicolor SPCCT [6], have been introduced in the field of CT imaging (Fig. 1D). These PCDs are the subject of ongoing research and development in CT systems [5, 7–10]. They have the capability of energy discrimination based on analysis of the pulse height of each detected photon of the transmitted x-ray spectrum and the count of their number above different energy thresholds or in multiple energy windows [7]. The number of energy bins (windows) depends on the design of the detection chain of the PCDs, and the energy thresholds can be selected depending on the chosen application. Hence, the transmitted spectrum is divided into several energy bins leading to better sampling of the X-ray spectrum than DECT. This characteristic allows detection of K-edges within certain energy windows and to distinguish simultaneously between different attenuation profiles, for instance those specific to different contrast agents, allowing multi-contrast agent imaging [6]. In addition, due to their architecture and detection mechanism, PCDs can provide improved spatial resolution and reduced radiation dose compared to conventional CT [11]. Although all these advantages have the potential to improve the five intrinsic limitations of the conventional CT imaging described above, SPCCT systems face technical challenges such as handling the high photon flux used in CT (approximately $10^9$ counts/sec/mm$^2$) [5].

## I.2. Technical aspects

With single energy CT imaging systems, tissues and materials can have the same attenuation values (i.e. Hounsfield unit values) despite having different compositions, based on their mass density [12], leading to a potential misclassification of pathologies, e.g. in differentiation between hemorrhage and tissue in a kidney cyst, or in separating calcified plaques from the lumen of vessels filled with iodine. Pitfalls such as these have encouraged the development of multi-energy CT imaging techniques, based on acquiring more than one dataset from energetically distinct X-ray spectra. The first technology based on a multi-energy approach that has been translated to clinical use is DECT imaging. SPCCT is a next generation, multi-energy

technology that is being seriously considered for clinical translation, with the first report of SPCCT scans of patients being recently published [13].

*DECT systems*

This term is typically used for techniques making use of two datasets that are derived from energetically distinct X-ray spectra in order to differentiate between different materials. Well-known implementations include emission based dual energy CT: dual-source CT [14–16], various implementations of kVp-switching from view-to-view during the CT acquisition [17–19], and detection based dual energy CT: i.e. dual-layer detector CT [20]. All these forms of DECT use EIDs. DECT enables two-material basis set decomposition techniques and a number of applications inaccessible to conventional CT. New image types that are often available from DECT systems include basis material images of iodine and water, soft-tissue and bone-images, and virtual mono-energy (MonoE) images (Fig 2) [12, 21, 22].

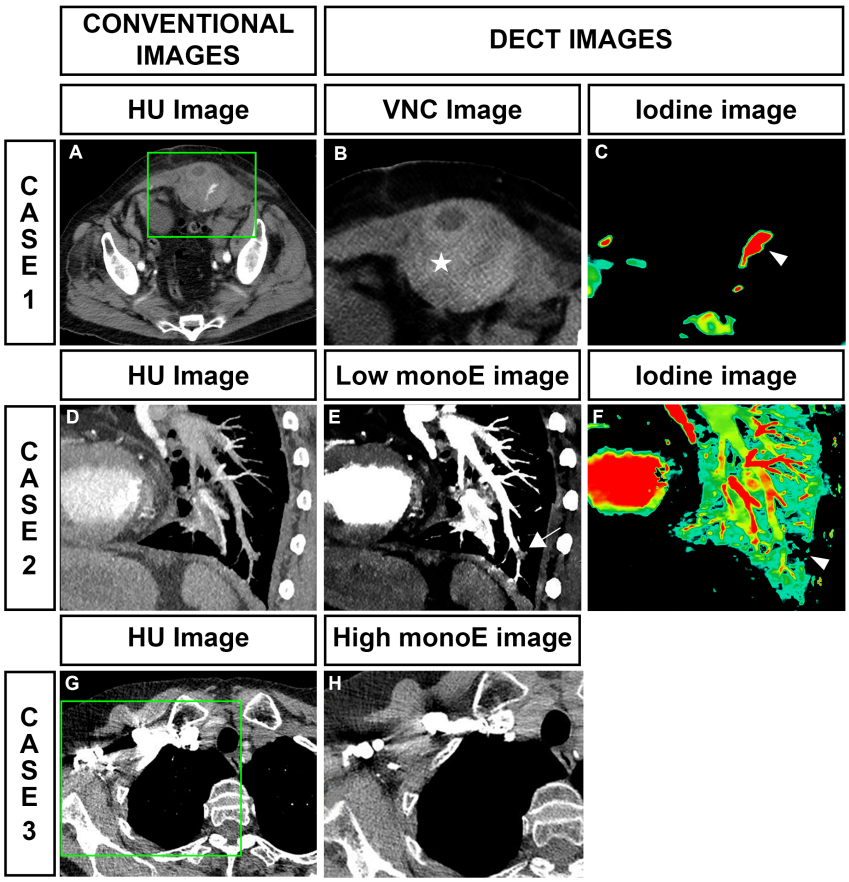

**Figure 2.** Examples of dual energy CT images. Case 1: In the conventional image (A) iodine cannot be discriminated from blood, but can be in the Virtual non enhanced (VNC) (B) and iodine images (C) where blood is highlighted with a star and iodine suffusion with an arrowhead. Case 2: The conventional image (D) didn't allow the diagnosis of a distal pulmonary artery thrombus due to imperfect opacification of the blood. However, the iodine image (E) revealed a defect of perfusion in the lung (arrowhead) indicating a pulmonary embolism, confirmed by the low kV (40 kV) monoenergetic images (F) that showed the thrombus due to stronger contrast in the pulmonary arteries (arrow). Case 3: The conventional image (G) has a substantial beam hardening artifact from the opacification of the subclavian vein, whereas the high (140 keV) mono-energetic image allowed a reduction of this artifact (arrowhead).

Iodine/water basis images are better known in the community as iodine maps and virtual-non-contrast images (VNC) (Fig 2A-C). The latter basis pair ideally separates the attenuation caused by atoms with an attenuation behavior like iodine (high atomic number with high photoelectric/Compton ratio) from attenuation caused by tissue material with attenuation behaviors similar to water (low atomic number with low photoelectric/Compton ratio). Nevertheless, current dual energy techniques have two main limitations in the accurate formation of VNC/iodine map image pairs [23]: 1) the two energy spectra, emitted and/or detected, have significant overlap and only provide moderate energy resolution; 2) the two energy spectra are not necessarily acquired precisely the same time and/or spatial location (not taken at the same azimuthal or axial position), except for detection based DECT. Another important imperfection of dual-energy iodine maps is contamination with attenuation arising from calcium-rich structures such as bones or calcifications, resulting from the previously mentioned limitations of DECT and the material decomposition technique making calcium shared between iodine and water images due to its intermediate attenuation behavior. In particular, in coronary CT angiography, the issues with differentiation between the contrast agent filled lumen and heavily calcified plaque compromise diagnosis.

In clinical use, the main benefits of iodine/water material decomposition from DECT are currently the possibility to avoid the non-enhanced scan leading to a dose reduction by using VNC for some applications, and on the other hand to get direct quantification of iodine tissue perfusion independently of the tissue density. This enables many clinical applications such as better and easier pulmonary embolism detection through lung perfusion defect detection (Fig 2D-F), or tumor perfusion quantification for oncology follow-up. Some other material

characterization applications already in use include detection of uric acid and calcium for renal stone or gout analysis. Another major imaging functionality enabled by DECT is the display of virtual mono-chromatic CT images, i.e. images of the linear attenuation coefficient μ(E) at a single energy chosen by the radiologist (Fig 2). This functionality offers the possibility to increase iodine contrast with low energy virtual monoE images, to better detect some lesions or reduce the amount of iodine injected, or to reduce metal artifacts in the images using high energy monoE images (Fig 2G,H), and to reduce beam hardening artifacts [22].

In practice, and for all current dual-energy implementations, the 2D material decomposition from two energetically different measurements constitutes mathematically an ill-conditioned inverse problem in which higher imaging specificity is obtained at the cost of increased image noise [24]. This is a well-known and reported problem. Energy-resolving photon-counting detectors will not change the fact that spectral material-decomposition remains a weakly-conditioned inverse problem, but offer the potential to significantly improve the mathematical conditioning, which will result in lower basis material noise [25].

*SPCCT systems*

SPCCT can be considered an extension of the detection based dual-energy CT technology [12] (Fig 1C), but with completely different detector technology. In this system, each X-ray photon is absorbed in the sensor and produces a small charge cluster (~2 fC or 10 000 electrons with ~100 μm spread) that can be collected by pixelated electrodes connected to individual electronic readout channels in an application specific integrated circuit (ASIC). This technique has many advantages over conventional CT detectors, i.e. individual photon counting and photon energy discrimination, the absence of electronic noise (due to the lower threshold discriminating between electronic noise and X-ray pulses), the improved spatial resolution because of small charge cluster size and the absence of electronic noise allowing reduced pixel size, the size compared to scintillator and photodiode conventional CT detectors, the absence of dead space (or septa) between detectors [26].

Hence, SPCCT technology allows the discrimination of the energies of individual photons enabling advanced material characterization tasks, which are only partially provided by dual-energy techniques. While the number of independent readings per frame and detector pixel in conventional CT, or DECT is limited to one, or two respectively, in SPCCT it is mainly

limited by the number of energy thresholds implemented in the ASICs hardware per channel (Fig 1C). In practice the number of thresholds used in SPCCT systems that have been reported range from four to eight [13, 27]. This, of course, provides the ability to better differentiate between different tissue types, even if the number of thresholds needs to be adapted to the intrinsic energy resolution and low-energy tailing behavior of the spectral detectors. Thus, the biggest advantage of SPCCT over DECT is the improved spectral sampling because of intrinsic energy resolution and energy windowing functionality absent in all DECT [7, 12]. SPCCT is expected to outperform dual energy techniques because of the following potential benefits: 1) Better spatial resolution, with a higher modulation transfer function in the usual range 0-15 lp/cm and significant strength in the extension to 25 lp/cm because of the smaller pixel size of PCDs. Consequently, this is leading to sharper edges and better delineation of structures in reconstructed images, with the additional value of decreasing the partial volume effects from small objects. 2) Improved contrast-to-noise ratio images due to the reduction of noise at low dose since photon counting does not have a noise floor from electronics and lower statistical noise due to counting versus integration compared to the EIDs [27]. 3) Reduced radiation dose and/or contrast media volume, due to the improved contrast to noise ratio of contrast-enhanced tissues at a given dose.

In addition, SPCCT is expected to present the following new capabilities: 1) The possibility to decompose more than 2 basis materials from multiple energy bins, enabling simultaneous multi-agent imaging. 2) Absolute quantification of specific contrast materials. Indeed, PCDs allow an exact physical representation of pixel values, with quantitative information processed by the SPCCT system from the spectrum transmitted through the subject. This allows measurement of the absolute concentration of targeted or non-targeted contrast media in regions-of-interest. 3) The possibility to map K-edge materials by using specific reconstructed images [7, 28, 29]. Image reconstruction in SPCCT has been a topic of intense research in the last decade, in particular when it was realized that the discrimination of energies of individual photons allows not only to selectively image, but to also quantify the concentrations of contrast agents based on elements with high-atomic numbers. This approach, called K-edge imaging, is based on the detection of the strong attenuation variation due to photoelectric effect at the specific binding energy of the K shell electron of an atom (e.g. 50.2

keV for gadolinium, 80.7 keV for gold). K-edge imaging allows measuring the absolute concentration of the targeted material used.

Lastly, similar to DECT systems, SPCCT allows reconstruction of mono-energetic images at desirable energies leading to an increase of the contrast of high atomic number materials at low kilovoltage due to the photoelectric effect.

However, certain limitations that are intrinsic to this technology have to be considered. Photon-counting detectors cannot function accurately with high count rates. Indeed, high count rates (i.e. high photon flux) can result in frequent instances of 2 photons being absorbed very close together in time and being incorrectly counted as a single photon with an energy equal to the sum of the energy of both photons. This effect, called electronic pileup, results in reduction of the energy resolution and impacts image quality [5, 7, 30, 31]. Hence, it explains the interest in having fast readout electronics and small detector pixels in order to decrease the count rate per pixel. However, reducing the pixel size too much can lead to an increase of another limitation of PCDs that is called charge sharing, i.e. the electron charge cloud caused by photon absorption in the detector being shared between two nearby pixels, also causing distortions in the spectral response. Research teams and manufacturers have made some different technologic choices and compromises [7] in order to build SPCCT systems that are being investigated in the pre-clinical field such as the camera and the MARS spectral scanner [32] and the system developed by Danielsson et al. [9], or in the clinical field [27, 33, 34].

Over the past ten years, the field of SPCCT imaging has been subject of significant research and development. In 2007, Roessl and Proksa demonstrated the additional value of the spectral information using simulated images of an atherosclerotic coronary vessel filled with a gadolinium-based contrast agent [29]. In 2008, Shikhaliev showed the first experimental results using SPCCT using x-ray energy weighting to form images that confirmed the improvement of CNR [10] due to the intrinsic architecture of the photon-counting detectors as we discussed above. The same year, Feurlein *et al* demonstrated the potential for improved luminal depiction in vascular imaging with SPCCT using the additional values of the monoenergetic images and the K-edge imaging of gadolinium in vitro [35]. Meanwhile, Firsching *et al* demonstrated spectral discrimination of an iodine contrast agent in a small animal CT scanner using the Medipix2 PCD [36] supporting the feasibility of contrast agent imaging using SPCCT. In 2010, Fredenberg *et al* showed that contrast-enhanced spectral mammography was feasible and

beneficial by drastically improving the signal noise ratio of breast tissue-like phantom [37]. The same year, Cormode *et al* demonstrated the spectral capabilities of SPCCT by using gold nanoparticles and an iodine contrast agent simultaneously. The gold nanoparticles were targeted to the macrophages of atherosclerotic plaque due to a coating similar to HDL and were well visualized, accumulating in the plaques of a mouse model of atherosclerosis, whereas the iodine contrast agent could be discriminated in the blood and calcified structures also distinguished at the same time [6]. This study highlights the use of candidate contrast agents for SPCCT imaging, as Pan *et al* demonstrated with bismuth and ytterbium based nanoparticles [38, 39] and as Schirra *et al* confirmed with gold nanoparticles [40]. In addition, recently, SPCCT has been tested in vitro for dual contrast colonography using iodine-filled lumen and gadolinium-tagged polyps allowing a potential differentiation between polyps and tagged fecal material [41].

In this context, SPCCT is a promising new tool that could assess lesion characteristics beyond what is currently achievable with conventional CT or MRI, with accurate quantification and the possibility of using targeted contrast agents. Furthermore, the accurate absolute quantification opens the way to functional imaging. Recently, the first patients have been scanned using this technology for various applications imaging with an without out any use of contrast media [13, 42–45], endorsing the concept that PCDs have a role to play as a next generation of CT systems.

**In conclusion,** spectral photon-counting CT imaging represents an emerging field of CT, already existing for clinical use with the dual energy CT systems, and being investigated with the photon-counting CT systems. Preliminary studies show the spectral possibilities that the photon-counting technology offers, demonstrating potentially very compelling applications for cardiovascular diseases, organ perfusion and molecular imaging. Moreover, these findings point to preclinical and clinical applications using multiple types of contrast agents, and also for multi-phase imaging in a single scan. In addition, it highlights the need to develop SPCCT specific contrast agents, which could expand the field of CT-based molecular imaging and create new paradigms in diagnostic imaging.

**REFERENCES**

1. Health equipment - Computed tomography (CT) scanners - OECD Data. In: theOECD. http://data.oecd.org/healtheqt/computed-tomography-ct-scanners.htm. Accessed 22 Feb 2017

2. Lehmann LA, Alvarez RE, Macovski A, et al (1981) Generalized image combinations in dual KvP digital radiography. Med Phys 8:659–667. https://doi.org/10.1118/1.595025

3. Brody WR, Cassel DM, Sommer FG, et al (1981) Dual-energy projection radiography: initial clinical experience. AJR Am J Roentgenol 137:201–205. https://doi.org/10.2214/ajr.137.2.201

4. Alvarez RE, Macovski A (1976) Energy-selective reconstructions in X-ray computerized tomography. Phys Med Biol 21:733–744

5. Taguchi K, Frey EC, Wang X, et al (2010) An analytical model of the effects of pulse pileup on the energy spectrum recorded by energy resolved photon counting x-ray detectors. Med Phys 37:3957–3969

6. Cormode DP, Roessl E, Thran A, et al (2010) Atherosclerotic plaque composition: analysis with multicolor CT and targeted gold nanoparticles. Radiology 256:774–782. https://doi.org/10.1148/radiol.10092473

7. Taguchi K, Iwanczyk JS (2013) Vision 20/20: Single photon counting x-ray detectors in medical imaging. Med Phys 40:100901. https://doi.org/10.1118/1.4820371

8. Schmitzberger FF, Fallenberg EM, Lawaczeck R, et al (2011) Development of low-dose photon-counting contrast-enhanced tomosynthesis with spectral imaging. Radiology 259:558–564. https://doi.org/10.1148/radiol.11101682

9. Liu X, Persson M, Bornefalk H, et al (2015) Spectral response model for a multibin photon-counting spectral computed tomography detector and its applications. J Med Imaging Bellingham Wash 2:033502. https://doi.org/10.1117/1.JMI.2.3.033502

10. Shikhaliev PM (2008) Energy-resolved computed tomography: first experimental results. Phys Med Biol 53:5595–5613. https://doi.org/10.1088/0031-9155/53/20/002

11. McCollough CH, Chen GH, Kalender W, et al (2012) Achieving routine submillisievert CT scanning: report from the summit on management of radiation dose in CT. Radiology 264:567–580. https://doi.org/10.1148/radiol.12112265

12. McCollough CH, Leng S, Yu L, Fletcher JG (2015) Dual- and multi-energy CT: principles, technical approaches, and clinical applications. Radiology 276:637–653. https://doi.org/10.1148/radiol.2015142631

13. Pourmorteza A, Symons R, Sandfort V, et al (2016) Abdominal imaging with contrast-enhanced photon-counting CT: first human experience. Radiology 279:239–245. https://doi.org/10.1148/radiol.2016152601

14. Petersilka M, Bruder H, Krauss B, et al (2008) Technical principles of dual source CT. Eur J Radiol 68:362–368. https://doi.org/10.1016/j.ejrad.2008.08.013

15. Primak AN, Giraldo JCR, Eusemann CD, et al (2010) Dual-source dual-energy CT with additional tin filtration: Dose and image quality evaluation in phantoms and in vivo. AJR Am J Roentgenol 195:1164–1174. https://doi.org/10.2214/AJR.09.3956

16. Primak AN, Ramirez Giraldo JC, Liu X, et al (2009) Improved dual-energy material discrimination for dual-source CT by means of additional spectral filtration. Med Phys 36:1359–1369. https://doi.org/10.1118/1.3083567

17. Hsieh J (2009) Dual-energy CT with fast-KvP switch. Med Phys 36:2749–2749. https://doi.org/10.1118/1.3182432

18. Kalender WA, Perman WH, Vetter JR, Klotz E (1986) Evaluation of a prototype dual-energy computed tomographic apparatus. I. Phantom studies. Med Phys 13:334–339. https://doi.org/10.1118/1.595958

19. Lehmann LA, Alvarez RE, Macovski A, et al (1981) Generalized image combinations in dual KvP digital radiography. Med Phys 8:659–667. https://doi.org/10.1118/1.595025

20. Altman A, Carmi R (2009) A double-layer detector, dual-energy CT — principles, advantages and applications. Med Phys 36:2750–2750. https://doi.org/10.1118/1.3182434

21. Fleischmann D, Boas FE (2011) Computed tomography--old ideas and new technology. Eur Radiol 21:510–517. https://doi.org/10.1007/s00330-011-2056-z

22. Grajo JR, Patino M, Prochowski A, Sahani DV (2016) Dual energy CT in practice: Basic principles and applications. Appl. Radiol.

23. Dinkel J, Khalilzadeh O, Phan CM, et al (2015) Technical limitations of dual-energy CT in neuroradiology: 30-month institutional experience and review of literature. J Neurointerventional Surg 7:596–602. https://doi.org/10.1136/neurintsurg-2014-011241

24. Alvarez R, Seppi E (1979) A comparison of noise and dose in conventional and energy selective computed tomography. IEEE Trans Nucl Sci 26:2853–2856. https://doi.org/10.1109/TNS.1979.4330549

25. Roessl E, Herrmann C, Kraft E, Proksa R (2011) A comparative study of a dual-energy-like imaging technique based on counting-integrating readout. Med Phys 38:6416–6428. https://doi.org/10.1118/1.3651643

26. Iwanczyk JS, Nygård E, Meirav O, et al (2009) Photon counting energy dispersive detector arrays for x-ray imaging. IEEE Trans Nucl Sci 56:535–542. https://doi.org/10.1109/TNS.2009.2013709

27. Gutjahr R, Halaweish AF, Yu Z, et al (2016) Human imaging with photon counting-based computed tomography at clinical dose levels: contrast-to-noise ratio and cadaver studies. Invest Radiol 51:421–429. https://doi.org/10.1097/RLI.0000000000000251

28. Schlomka JP, Roessl E, Dorscheid R, et al (2008) Experimental feasibility of multi-energy photon-counting K-edge imaging in pre-clinical computed tomography. Phys Med Biol 53:4031–4047. https://doi.org/10.1088/0031-9155/53/15/002

29. Roessl E, Proksa R (2007) K-edge imaging in x-ray computed tomography using multi-bin photon counting detectors. Phys Med Biol 52:4679. https://doi.org/10.1088/0031-9155/52/15/020

30. Cammin J, Xu J, Barber WC, et al (2014) A cascaded model of spectral distortions due to spectral response effects and pulse pileup effects in a photon-counting x-ray detector for CT. Med Phys 41:041905. https://doi.org/10.1118/1.4866890

31. Wang AS, Harrison D, Lobastov V, Tkaczyk JE (2011) Pulse pileup statistics for energy discriminating photon counting x-ray detectors. Med Phys 38:4265–4275

32. Zainon R, Ronaldson JP, Janmale T, et al (2012) Spectral CT of carotid atherosclerotic plaque: comparison with histology. Eur Radiol 22:2581–2588. https://doi.org/10.1007/s00330-012-2538-7

33. da Silva J, Grönberg F, Cederström B, et al (2019) Resolution characterization of a silicon-based, photon-counting computed tomography prototype capable of patient scanning. J Med Imaging Bellingham Wash 6:043502. https://doi.org/10.1117/1.JMI.6.4.043502

34. Willemink MJ, Persson M, Pourmorteza A, et al (2018) Photon-counting CT: Technical Principles and Clinical Prospects. Radiology 289:293–312. https://doi.org/10.1148/radiol.2018172656

35. Feuerlein S, Roessl E, Proksa R, et al (2008) Multienergy photon-counting K-edge imaging: potential for improved luminal depiction in vascular imaging. Radiology 249:1010–1016. https://doi.org/10.1148/radiol.2492080560

36. Markus Firsching, Anthony P. Butler, Nicola Scott, et al (2009) Contrast agent recognition in small animal CT using the Medipix2 detector. Nucl. Instrum. Methods Phys. Res. Volume 607, Issue 1, Pages 179–182

37. Fredenberg E, Hemmendorff M, Cederström B, et al (2010) Contrast-enhanced spectral mammography with a photon-counting detector. Med Phys 37:2017–2029. https://doi.org/10.1118/1.3371689

38. Pan D, Roessl E, Schlomka J-P, et al (2010) Computed tomography in color: nanoK-enhanced spectral CT molecular imaging. Angew Chem Int Ed Engl 49:9635–9639. https://doi.org/10.1002/anie.201005657

39. Pan D, Schirra CO, Senpan A, et al (2012) An early investigation of ytterbium nanocolloids for selective and quantitative "multicolor" spectral CT imaging. ACS Nano 6:3364–3370. https://doi.org/10.1021/nn300392x

40. Schirra CO, Senpan A, Roessl E, et al (2012) Second generation gold nanobeacons for robust k-edge imaging with multi-energy ct. J Mater Chem 22:23071–23077. https://doi.org/10.1039/C2JM35334B

41. Muenzel D, Bar-Ness D, Roessl E, et al (2016) Spectral photon-counting CT: initial experience with dual-contrast agent K-edge colonography. Radiology 160890. https://doi.org/10.1148/radiol.2016160890

42. Symons R, Sandfort V, Mallek M, et al (2019) Coronary artery calcium scoring with photon-counting CT: first in vivo human experience. Int J Cardiovasc Imaging 35:733–739. https://doi.org/10.1007/s10554-018-1499-6

43. Symons R, Reich DS, Bagheri M, et al (2018) Photon-Counting Computed Tomography for Vascular Imaging of the Head and Neck: First In Vivo Human Results. Invest Radiol 53:135–142. https://doi.org/10.1097/RLI.0000000000000418

44. Symons R, Pourmorteza A, Sandfort V, et al (2017) Feasibility of dose-reduced chest CT with photon-counting detectors: initial results in humans. Radiology 285:980–989. https://doi.org/10.1148/radiol.2017162587

45. Symons R, Cork TE, Sahbaee P, et al (2017) Low-dose lung cancer screening with photon-counting CT: a feasibility study. Phys Med Biol 62:202–213. https://doi.org/10.1088/1361-6560/62/1/202

## II. POTENTIAL OF SPCCT FOR CARDIOVASCULAR IMAGING

In this review, we describe our preliminary experience as well as from others on cardiovascular imaging using the SPCCT technology. Our results were acquired using a prototype spectral photon-counting computed tomography system derived from a modified clinical CT with a small field-of-view at 168 mm. It allowed *in vivo* acquisitions with a temporal resolution of 0.75 second (Figure 1).

A

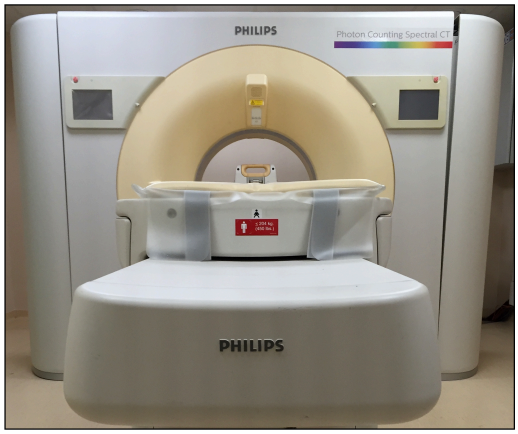


B

| Parameter | Scanner Specifications |
|---|---|
| Base Platform | iCT |
| Tube Voltage | 80, 100, 120 kVp |
| Tube Current | 10-100 mA |
| Acquisition Modes | Axial, Step and Shoot, Helical |
| Z-Coverage | 2 mm |
| FOV | 168 mm |
| Minimum Rotation Time | 0.75 sec/rotation |

**Figure 1.** (A) Photograph of the experimental SPCCT system. (B) Characteristics of the SPCCT system.

### II.1. Imaging of atherosclerosis

Atherosclerosis and its final complication, plaque ruptures and subsequent infarct in heart or brain is the main underlying pathology of cardiovascular diseases (CVD) and atherosclerosis is responsible for 70% of all cases of CVD. In order to reduce the risk of an acute event, unstable atherosclerosis has to be detected at an early stage of its development.A variety of factors contribute to the development and progression of atherosclerosis. The earliest steps in the development of coronary artery disease are thought to be the dysfunction of the endothelium. This initial process is followed by molecular mechanisms that contribute to plaque development and progression: inflammation, macrophage infiltration, lipid deposition, calcification, extracellular matrix degradation, oxidative stress, cell apoptosis, and thrombosis [1, 2]. However, atherosclerosis ultimately progresses to clinically over cardiovascular disease. These clinical

manifestations are most often the result of an atherosclerotic plaque rupture. Therefore, identification of plaques at high risk of rupture is thus a major clinical concern.

Current treatment strategies (including medication, stenting and surgical approach such as endarterectomy) rely on the measurement of the plaque-related stenosis of the considered artery [3, 4]. Standard and dual-energy CT are widely used to assess this degree of stenosis but their results are often impaired by their current spatial resolution (0.5 mm insufficient to image vessels smaller than 1 mm) and the presence of calcification within the plaque, particularly during coronary arteries examination. This excludes a large proportion of patients who are still referred to invasive techniques such as coronary angiography as MRI, which is less sensitive to calcification, cannot currently correctly assess the coronary arteries. In this field, the spectral analysis provided by SPCCT to separate between calcifications and contrast-enhanced vessel lumen could improve the quantification of the stenosis and strongly reduce the examination failure rate in patients with heavily calcified arterial wall, as previously suggested [5]. Similarly, SPCCT, by increasing the spatial resolution of the detectors by a factor of two, will strongly improve the accuracy of stenosis measurement in these small vessels, as previously demonstrated [6, 7].

Beside stenosis assessment, several clinical observations have emphasized the need for a more detailed analysis of the structure and biology of atherosclerotic plaques. The goal is to identify vascular remodeling and describe plaques with regard to specific criteria of vulnerability, such as a thin fibrous cap and a large lipid core. MR imaging approaches have been developed, and these approaches allow non-invasive characterization of the vessel wall but still with a lack of spatial resolution and a short anatomic coverage which limits the techniques to an analysis of a few plaques during the same examination. A preliminary *ex-vivo* study of coronary arteries on a preclinical limited field-of-view SPCCT prototype demonstrated a great potential for plaque component analysis (i.e. lipid, calcium and fibrosis) by individually analyzing photo-electric, Compton scattering and iodine concentration (after contrast injection with K-edge technique) of each plaque components [8](Figure 2). A second study *ex vivo* backed up the potential of SPCCT to differentiate atherosclerotic plaque components (lipids and calcification) based on their specific photo-electric and Compton effects [9]. In addition, a study have highlighted the interest of SPCCT for improving the ability to quantify the vasa vasorum density a marker of atherosclerotic plaque severity [10]. Finally, a recent study demonstrated the

improvement in the reproducibility of coronary calcium burden (Agatson calcium score) with low x-ray radiation dose protocol compared to standard dose CT, using SPCCT opposite to standard CT [11].

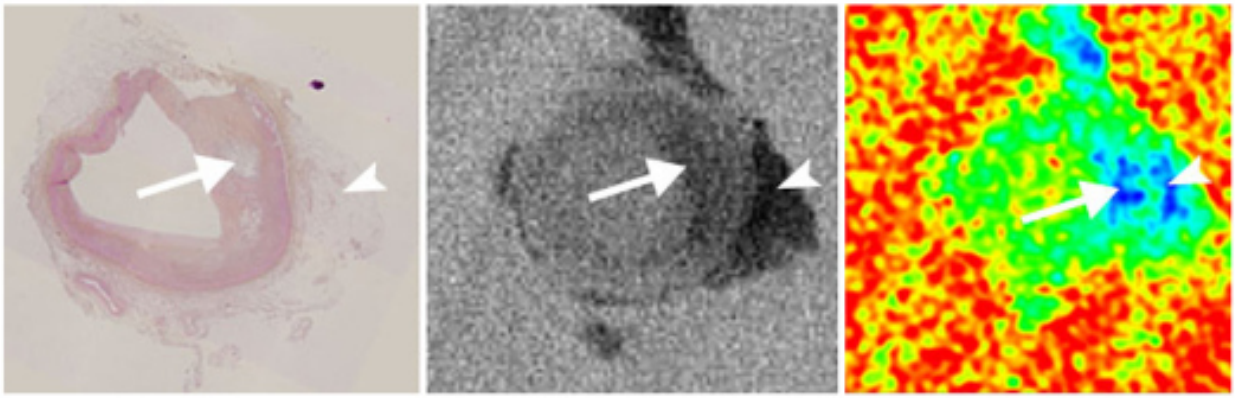

**Figure 2.** Slice of a coronary artery presenting with a lipid-rich plaque (white arrows): histological slice (left part) and photoncounting spectral CT images with CT-like image (centre) and color-coded iodine concentration (right part) maps [linear scale from black (0 $mmol^{-1}$) to white (70 $mmol^{-1}$)]. Surrounding perivascular fat is also present on the slices (arrow heads)[8].

In parallel, the explosive growth of biocompatible nanotechnologies now offers the possibility to build specific contrast agents embedding these atoms as a payload. For example, *Cormode et al.* have shown, using a similar prototype, that gold embedded in specific nanoparticles can be detected in unstable plaque [12](Figure 3). However, this prototype was not adequate for *in-vivo* applications because of its low count-rate capability, resulting in long scan times. But the technology has being scaled up recently to human sizes to prepare acquisition protocols for human scanning.

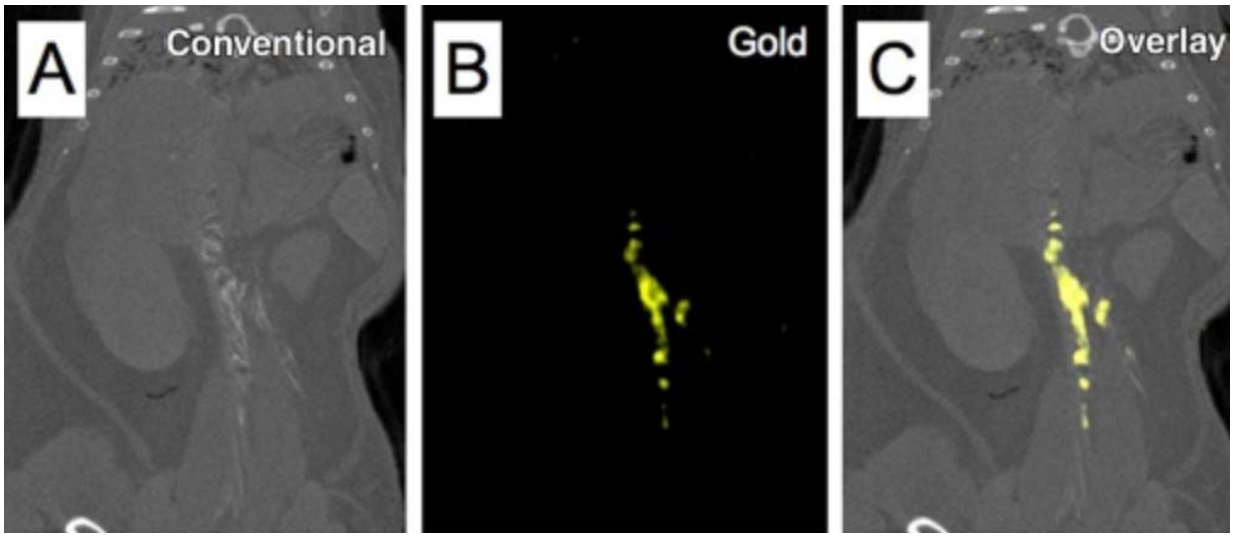


**Figure 3.** Spectral CT images of thorax and abdomen in apo E–KO mouse injected 24 hours earlier with Au-HDL.

This technology would then allow for better assessing atherosclerotic plaque components and the level of intra-plaque inflammation in order to adapt the preventive treatment for each patient. Furthermore, thrombus imaging and quantitative perfusion imaging allowed by SPCCT, will assist in the treatment decision in stroke or myocardial infarction, namely thrombolysis and reperfusion lesion prevention (i.e. by using cyclosporine) in emergency settings. Furthermore, monitoring tissue inflammation and perfusion recovery will allow to assess the therapeutic response in these patients. Thus, a significant impact on clinical decisions in cardiovascular diseases is expected thanks to a relatively affordable and widely available imaging technique.

### II.2.Lumen and stent imaging

Blooming artifacts in standard CT angiography images related to vascular calcifications and metallic stents impair correct visualization of the vascular lumen, reducing the possibility of diagnosis of coronary stenosis or in-stent restenosis. Indeed, blooming artifacts can cause under- or over-estimation of the vessel lumen because of the thicker appearance of highly attenuating materials [13]. Hence, there is a need for decreasing blooming artifacts, which are due mainly to highly attenuating material artifacts and the partial volume averaging effect. The higher spatial resolution inherent to SPCCT systems has the potential to reduce the partial volume effect and therefore might be expected to reduce blooming, as related recently by multiple studies *in vitro* (Figure 4) [6, 14–16]. But we investigated this capability also *in vivo*. Our results have

demonstrated that the apparent width of the metallic struts of different stents was smaller on SPCCT than on the standard CT (Figure 5) confirming the improvement in the visualization of stent architecture compared to a standard CT system [7].

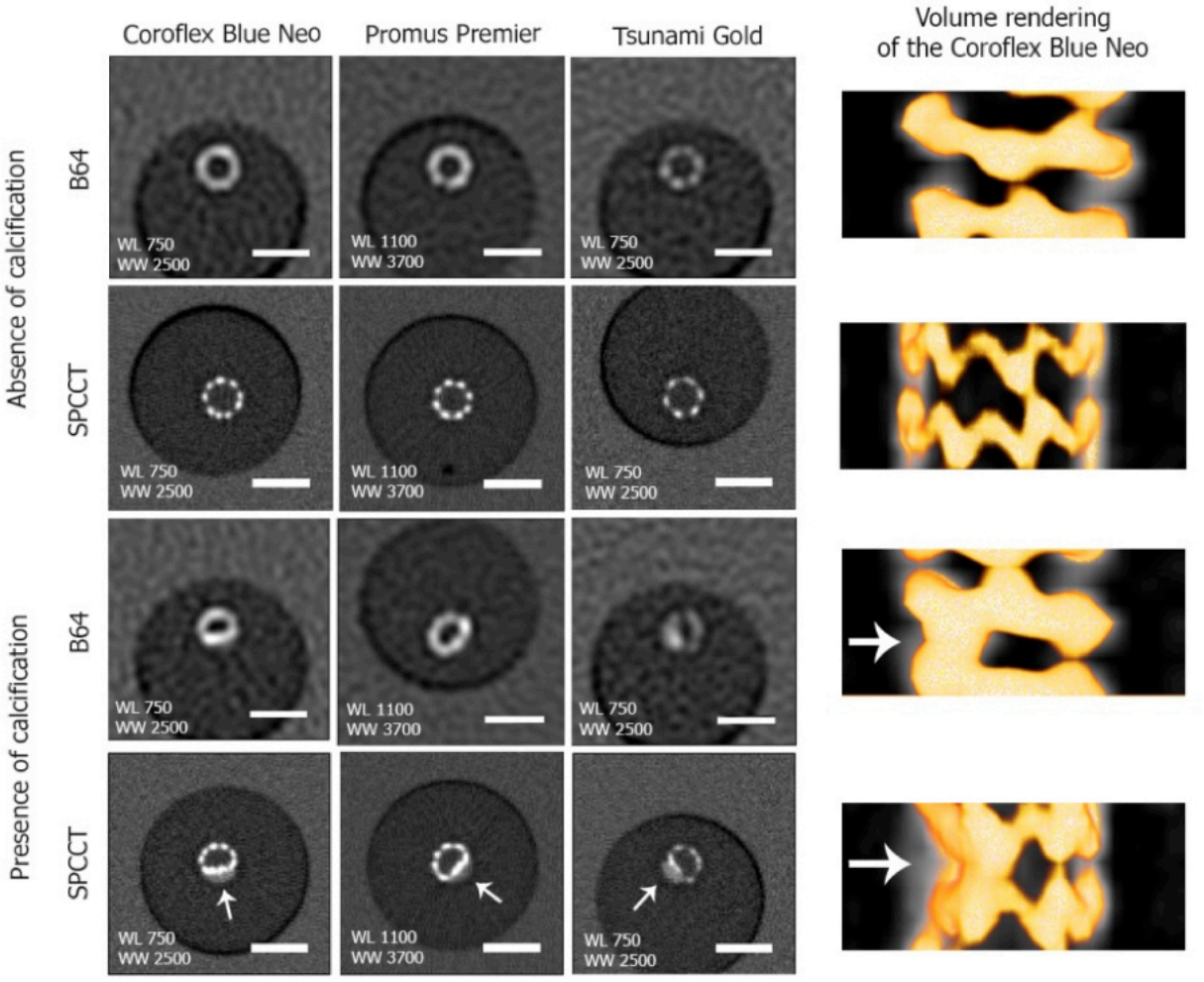


**Figure 4.** Representative conventional HU images acquired on the Brilliance 64 and on the SPCCT at similar locations in the stents in the absence (top) and presence of calcification (bottom)[15]. The smaller size of the photon counting detectors results in an improved visualization of the stent metallic struts. On the SPCCT images the stents can be visually separated from the calcification (white arrows), while this separation is not possible on the B64 images due to larger detector size. The improved quality of SPCCT images allows clear visualization by volume rendering (right for the Coroflex Blue Neo stent) of the metallic mesh of the stent and its deformation due to the presence of the calcification insert, while this is not possible for B64. A 5mm scale bar is shown on each conventional HU image.

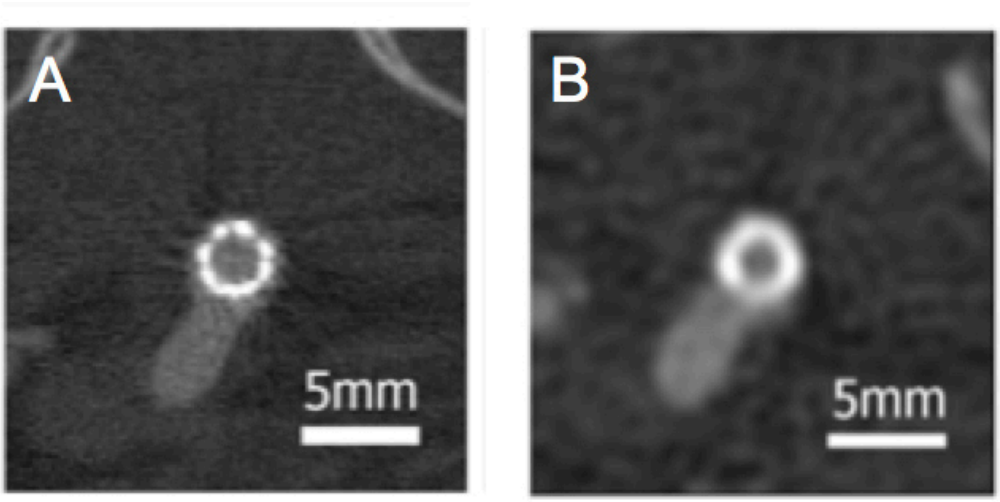


**Figure 5.** SPCCT (Philips, Haïfa, Israel)(A) and standard CT (Brilliance 64; Philips, Haïfa, Israel)(B) acquisitions of a stent placed in the aorta of a rabbit, under similar acquisition and reconstruction parameters [15].

In addition, given the great spatial resolution of the photon-counting detectors and their noise efficiency, the SPCCT technology presents the ability to improve the depiction of the lumen coronary arteries, even more in presence of vascular calcifications (Figure 6)[6, 7].

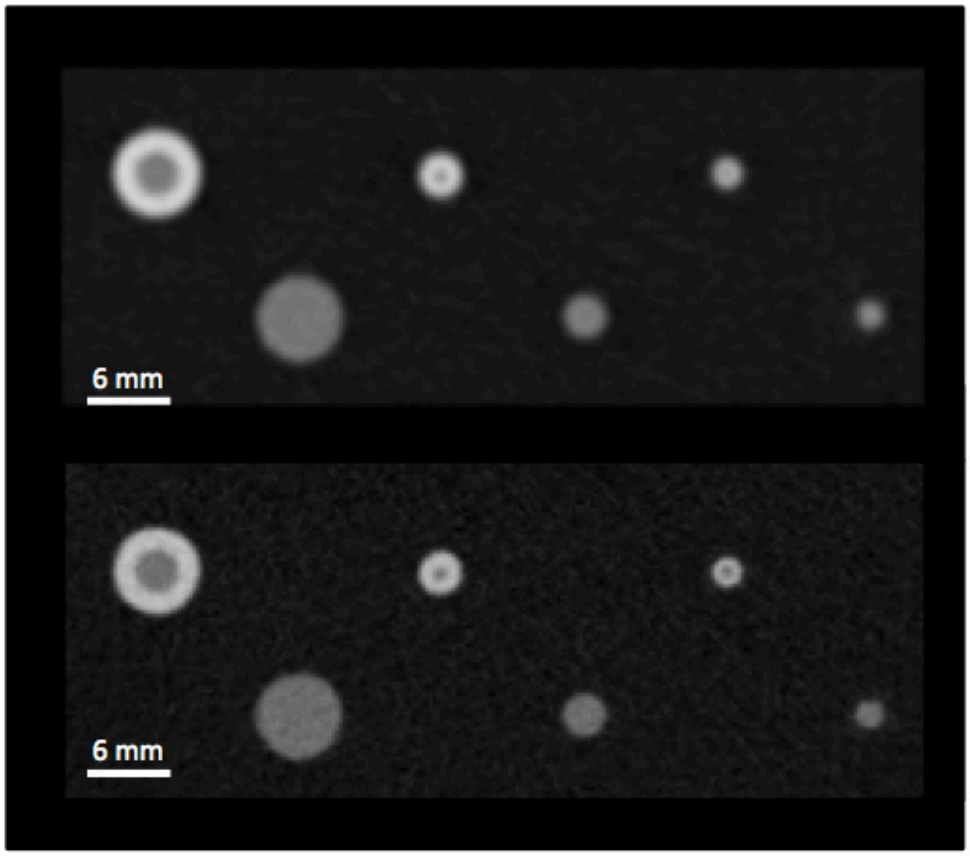


**Figure 6.** Representation of conventional images of a coronary phantom presenting a peripheral calcium-like ring and a lumen filling with an iodinated contrast agent (concentration at 21.4 mg/mL)(dual-layer dual-energy CT with high resolution on top row; SPCCT on the bottom row)[17]. The sharpness and depiction between the calcifications and the lumen are better on the SPCCT images compared to high resolution DECT in all the tubes even in the smaller one (0.5 mm diameter of the lumen).

It is also possible to anticipate the possibility to perform a coronary SPCCT angiography K-edge imaging using a gadolinated contrast agent as well as an aortic SPCCT angiography [18] (Figures 7 and 8). In an *ex vivo* coronary artery study, we demonstrated that SPCCT allowed a full 3D coronary SPCCT imaging with clear differentiation between calcification and gadolinium using spectral K-edge images. K-edge gadolinium images demonstrated exclusively the lumen with benefice of the removal of all the other structures, e.g. calcified plaque, soft tissue and with absence of blooming artefact. Mean lumen diameter measured on K-edge images were higher than measured on conventional CT images (2.0±0.13 cm vs 1.8±0.1 cm, $p<0.05$) in favor of

blooming artefact suppression. Hence, SPCCT with a K-edge contrast agent may be a promising tool for better depiction of the lumen diameter quantification.

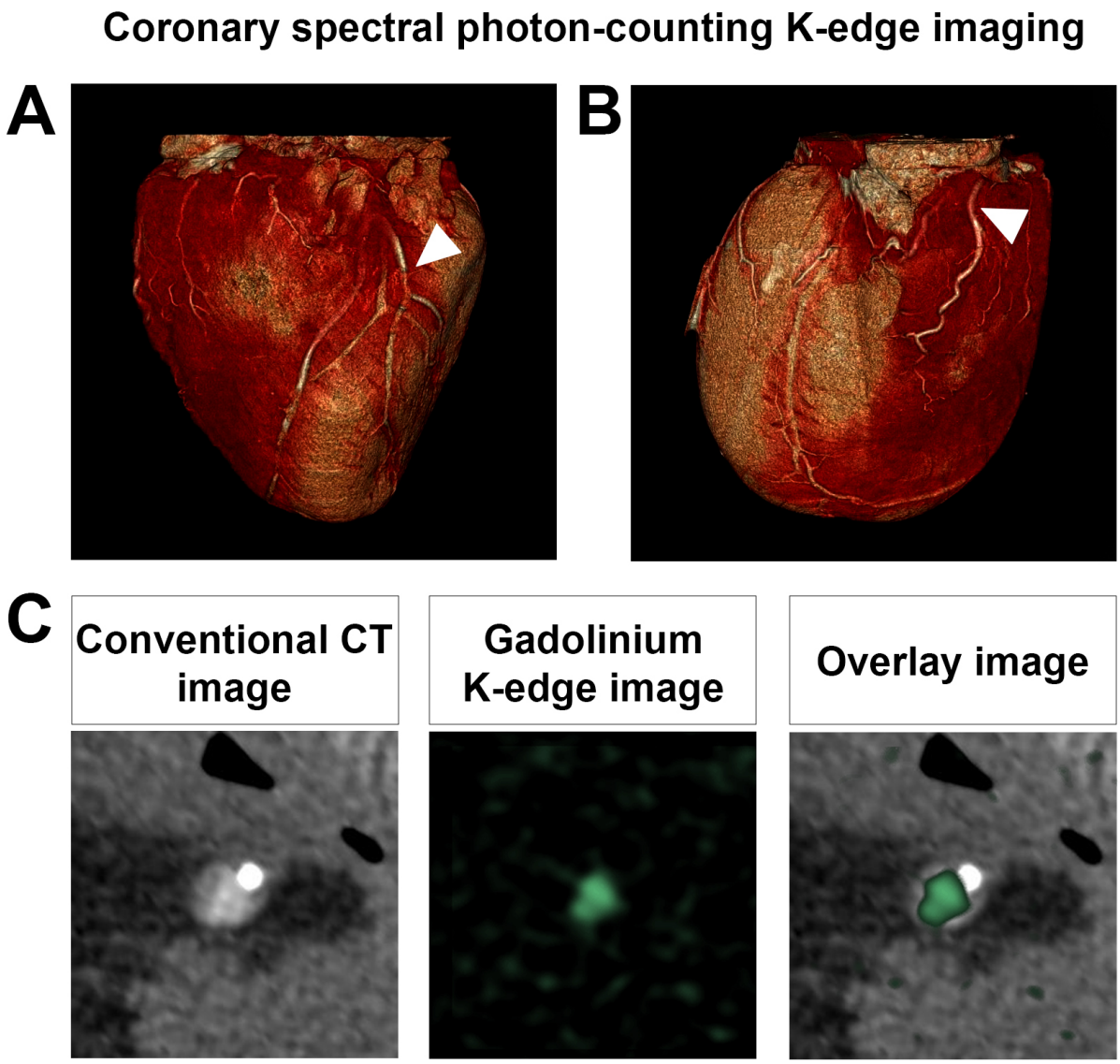


**Figure 7.** Representation of a full SPCCT acquisition of an *ex-vivo* heart with calcified coronary arteries. The injection of a gadolinated contrast agent demonstrated on the gadolinium images via the K-edge technique a better depiction for the lumen in presence of calcifications [5].

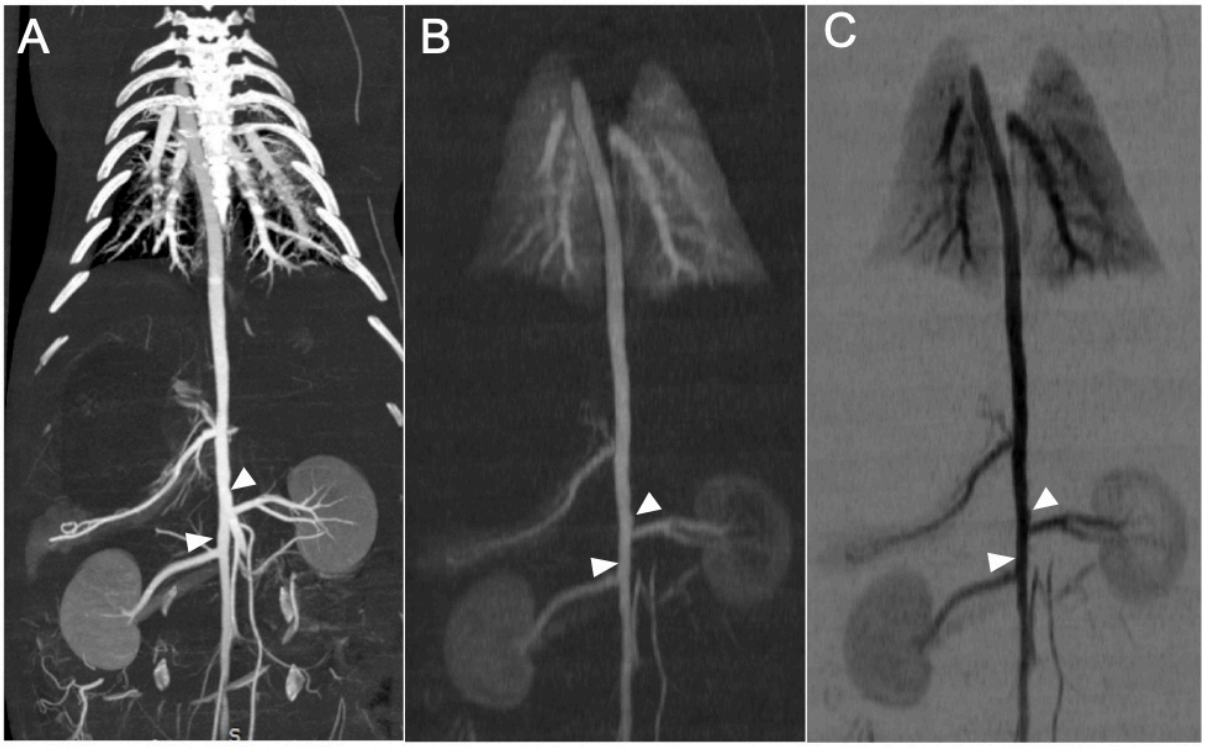


**Figure 8.** SPCCT enabled K-edge angiography in an atherosclerotic rabbit in combination with a gadolinated contrast agent (Prohance, Gadoteridol, BRACCO, ITALY). Injection protocol consisted in IV injection of 3.5 mL/kg of contrast agent at 2 mL/s of. Maximum-Intensity-Projection K-edge images (A: conventional image, B: K-edge image, C: negative K-edge image) of a whole atherosclerotic aorta showed ulceration and aneurysmal remodelling (white arrows). Note also the clear vizualisation of the lung microcirculation imaging, known as a surrogate marker for lung perfusion.

### II.3.Myocardial infarction imaging

Conventional and Dual-energy CT assembly with their superior quality for imaging coronary arteries and functional cardiac imaging capability, is increasingly used as a non-invasive imaging investigation. They have been proposed to detect myocardial perfusion defects, including following acute or chronic infarction [19]. However, studies using CT data are susceptible to beam-hardening artefacts that may mimic perfusion defect. Furthermore, CT, as MRI, allows a visualization of the perfusion defect but not a real quantification of the perfusion. This quantification can be performed with PET but again with a poor accessibility and a high cost. Finally, the radiation dose in perfusion CT is currently too high for a clinical application of CT perfusion. Similarly, studies in animals and humans indicate that myocardial perfusion studies performed with CT accurately detect myocardial ischemia and infarcts compared with single photon emission computed tomography (SPECT), but includes a rather high radiation exposure. Furthermore, the detection of myocardial late enhancement has been demonstrated with conventional CT[20]**.** However, because of the poor contrast between normal and abnormal myocardium in late enhancement studies with conventional CT limits its clinical use and its potential in determining precisely the different components of reperfusion myocardial lesions.

Hence, the SPCCT has the potential to overcome these limitations in perfusion and delayed enhancement imaging by obtaining artifact-free accurate material-decomposition images for quantitative iodine and Gadolinium contrast based perfusion measurement with K-edge imaging technique**.** We conducted a preliminary stuy in an occlusion-reperfusion rabbit model and confirmed the potential of specific and quantitative K-edge imaging of the infarction using a gadolinated contrast agent (Figure 9), but a full field-of-view prototype measurement is needed to fully validate these advantages. Other study presented also a proof-of-concept for vizualization simultaneaously of the blood pool, scar, and remote myocardium using a first-pass iodine and late gadolinium maps [21]. In this study, MRI and histology analysis confirmed accurate PCD CT delineation of scar.

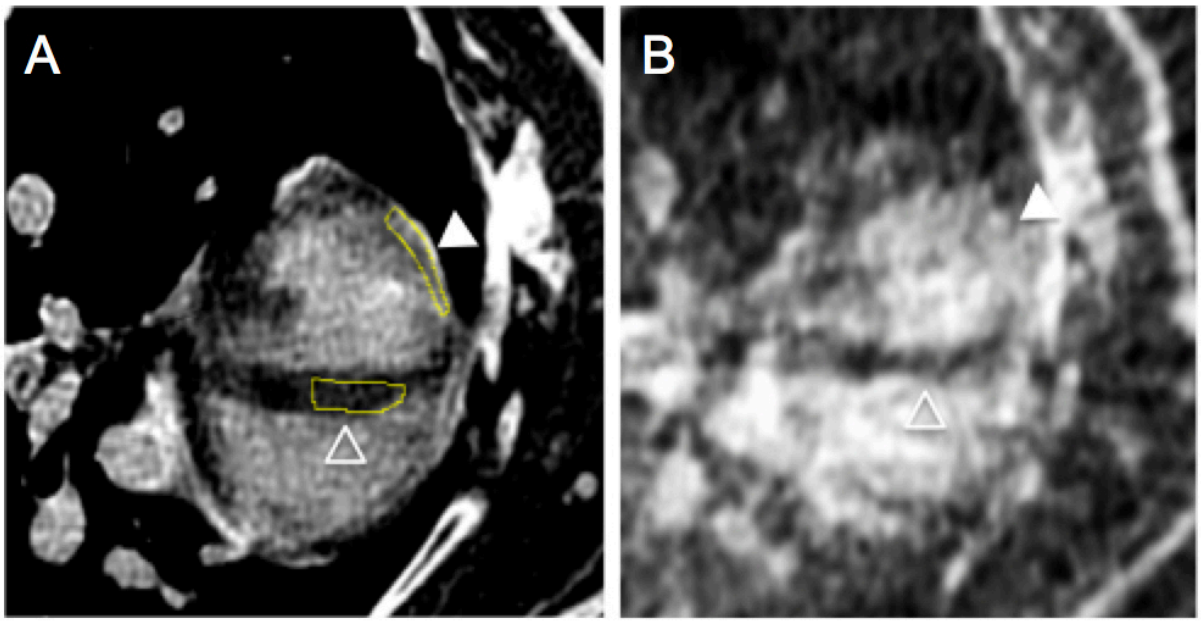


**Figure 9.** Late gadolinium enhancement SPCCT images of a rabbit myocardial infarction (A: conventional image, B: K-edge maps of gadolinium, empty head arrow: remote myocardium, full head arrow: infarcted myocardium). The K-edge images allow the quantification of the gadolinium in the infarcted zone for evaluation of the extra-cellular volume (Infarcted myocardium: 8.53±1.66 mg/ml versus remote myocardium: 4.9±1.56 mg/ml).

**In conclusion,** SPCCT has the potential for an innovative *in vivo* high-resolution spectral quantitative imaging of atherosclerotic coronary arteries, and myocardial tissue, with new photon counting detectors technology using standard and new specific contrast media at a potential lower X-ray dose in order to overcome the current limitations in CT imaging, mainly spatial and spectral resolution and radiation dose.

## REFERENCES

1. Libby P (2002) Inflammation in atherosclerosis. Nature 420:868–874. https://doi.org/10.1038/nature01323

2. Malek AM, Alper SL, Izumo S (1999) Hemodynamic shear stress and its role in atherosclerosis. JAMA 282:2035–2042

3. (1995) Endarterectomy for asymptomatic carotid artery stenosis. Executive Committee for the Asymptomatic Carotid Atherosclerosis Study. JAMA 273:1421–1428

4. (1998) Randomised trial of endarterectomy for recently symptomatic carotid stenosis: final results of the MRC European Carotid Surgery Trial (ECST). Lancet Lond Engl 351:1379–1387

5. Feuerlein S, Roessl E, Proksa R, et al (2008) Multienergy photon-counting K-edge imaging: potential for improved luminal depiction in vascular imaging. Radiology 249:1010–1016. https://doi.org/10.1148/radiol.2492080560

6. Bratke G, Hickethier T, Bar-Ness D, et al (2019) Spectral Photon-Counting Computed Tomography for Coronary Stent Imaging: Evaluation of the Potential Clinical Impact for the Delineation of In-Stent Restenosis. Invest Radiol. https://doi.org/10.1097/RLI.0000000000000610

7. Sigovan M, Si-Mohamed S, Bar-Ness D, et al (2019) Feasibility of improving vascular imaging in the presence of metallic stents using spectral photon counting CT and K-edge imaging. Sci Rep 9:19850. https://doi.org/10.1038/s41598-019-56427-6

8. Boussel L, Coulon P, Thran A, et al (2014) Photon counting spectral CT component analysis of coronary artery atherosclerotic plaque samples. Br J Radiol 87:20130798. https://doi.org/10.1259/bjr.20130798

9. Zainon R, Ronaldson JP, Janmale T, et al (2012) Spectral CT of carotid atherosclerotic plaque: comparison with histology. Eur Radiol 22:2581–2588. https://doi.org/10.1007/s00330-012-2538-7

10. Jorgensen SM, Korinek MJ, Vercnocke AJ, et al (2016) Arterial Wall Perfusion Measured with Photon Counting Spectral X-ray CT. Proc SPIE-- Int Soc Opt Eng 9967:. https://doi.org/10.1117/12.2238817

11. Symons R, Sandfort V, Mallek M, et al (2019) Coronary artery calcium scoring with photon-counting CT: first in vivo human experience. Int J Cardiovasc Imaging 35:733–739. https://doi.org/10.1007/s10554-018-1499-6

12. Cormode DP, Roessl E, Thran A, et al (2010) Atherosclerotic plaque composition: analysis with multicolor CT and targeted gold nanoparticles. Radiology 256:774–782. https://doi.org/10.1148/radiol.10092473

13. Mahnken AH (2012) CT Imaging of Coronary Stents: Past, Present, and Future. ISRN Cardiol 2012:. https://doi.org/10.5402/2012/139823

14. Mannil M, Hickethier T, von Spiczak J, et al (2017) Photon-Counting CT: High-Resolution Imaging of Coronary Stents. Invest Radiol. https://doi.org/10.1097/RLI.0000000000000420

15. Si-Mohamed S, Cormode, DP, Sigovan M, et al (2019) K-edge specific non-invasive macrophage spectral photon counting CT imaging in atherosclerosis using PEGylated gold nanoparticles. RSNA

16. Symons R, De Bruecker Y, Roosen J, et al (2018) Quarter-millimeter spectral coronary stent imaging with photon-counting CT: Initial experience. J Cardiovasc Comput Tomogr 12:509–515. https://doi.org/10.1016/j.jcct.2018.10.008

17. Sigovan M, Coulon P, Si-Mohamed S, Douek P (2017) Noninvasive evaluation of coronary artery stenosis : in vitro comparison of a Spectral Photon Counting CT and spectral Dual Layer CT. RSNA

18. Si-Mohamed S, Perrier L, Sigovan M, et al (2017) Potential for coronary K-edge imaging with Spectral Photon Counting CT. RSNA

19. Mewton N, Rapacchi S, Augeul L, et al (2011) Determination of the myocardial area at risk with pre- versus post-reperfusion imaging techniques in the pig model. Basic Res Cardiol 106:1247–1257. https://doi.org/10.1007/s00395-011-0214-8

20. Boussel L, Gamondes D, Staat P, et al (2008) Acute chest pain with normal coronary angiogram: role of contrast-enhanced multidetector computed tomography in the differential diagnosis between myocarditis and myocardial infarction. J Comput Assist Tomogr 32:228–232. https://doi.org/10.1097/RCT.0b013e3181452199

21. Symons R, Cork TE, Lakshmanan MN, et al (2017) Dual-contrast agent photon-counting computed tomography of the heart: initial experience. Int J Cardiovasc Imaging 33:1253–1261. https://doi.org/10.1007/s10554-017-1104-4

# Chapter II

*In vitro* spectral photon-counting CT imaging

# MONOCOLOR AND MULTICOLOR K-EDGE IMAGING *IN VITRO*

**Title: Multicolor imaging with spectral photon-counting computed tomography : a phantom study**

S. Si-Mohamed[1,2], D.Bar-Ness [1], M. Sigovan[1], V. Tatard-Leitman[1], D.P. Cormode[4], P.C. Naha[4], P. Coulon[5], L. Rascle[1], E. Roessl[6], M. Rokni[3], A. Altman[3], Y. Yagil[3], L. Boussel[1,2], P. Douek[1,2]

1. University Claude Bernard Lyon1, CREATIS, CNRS UMR 5220, INSERM U1206, INSA-Lyon, France
2. Radiology Department, Hospices Civils de Lyon, France.
3. Global Advanced Technologies, CT, Philips, Haifa, Israel
4. Department of Radiology, University of Pennsylvania, Philadelphia, PA, USA.
5. CT Clinical Science, Philips, Suresnes, France.
6. Philips GmbH Innovative Technologies, Research Laboratories, Hamburg, Germany.

## ABSTRACT

**Purpose.** To evaluate the feasibility of multicolor imaging with a spectral photon-counting computed tomography (SPCCT) in order to detect and quantify different mixed contrast agents.

**Methods**. Phantoms containing 11 tubes with mixtures of varying proportions of two contrast agents (i.e. two selected from gadolinium, iodine or gold nanoparticles) were prepared such as the attenuation of each tube was about 280 HU. Scans were acquired at 120 kVp and 100 mAs using a 5 bins SPCCT, generating conventional, water, iodine, gadolinium and gold images. The correlation between prepared and measured concentrations was assessed using linear regression. The cross-contamination was measured for each material as the root mean square errors (RMSE) of its concentration in the other material images, where no signal was expected. The contrast-to-noise ratios (CNR) relative to a PBS tube were calculated for each contrast agent.

**Results**. The solutions had similar attenuations (279±10 HU) and could not be differentiated in conventional images. However, distinction was observed in the material images within the same samples, and the measured and prepared concentrations were strongly correlated ($R^2$ values $\geq$ 0.97, 0.81 $\leq$ slope $\geq$ 0.95, - 0.68 $\leq$ offset $\leq$ 0.89 mg/mL). Cross-contamination in the iodine images for the mixture of gold and gadolinium contrast agents (RMSE = 0.34 mg/mL) was

observed. CNR for 1 mg/mL of contrat agent were better for the mixture of iodine and gadolinium ($CNR_{Iodine}$ = 3.20, $CNR_{Gd}$ = 2.80) than gold and gadolinium ($CNR_{Gd}$ = 1.67, $CNR_{Gold}$ = 1.37).

**Conclusion.** SPCCT enables multicolor quantitative imaging.

## INTRODUCTION

Since the emergence of clinical dual energy computed tomography (DECT) and spectral photon counting computed tomography (SPCCT), there has been increasing interest in using these systems to discriminate between different contrast agents, based on their specific X-ray attenuation characteristics (1–9). For example, DECT has recently been used for *in vivo* depiction of the small bowel wall and for the differentiation between a vascular and an enteric injury, using a combination of an intravenous iodinated contrast agent with an oral tantalum or tungsten-based contrast agent (10), and oral bismuth (11) respectively. However, because DECT is limited by its sampling capacity of only two predefined energy spectra, high (140 kVp) and low (80 kVp) (5,12,13), the attenuation model used for reconstruction is restrained to the material decomposition of only two base images (5,14); any other material is represented as an equivalent ratio of the two base materials. Moreover, the DECT material decomposition scheme doesn't contain the K-edge discontinuity, which has to be determined using data from an additional energy (5,15,16).

Unlike DECT, SPCCT uses energy resolving detectors that can simultaneously sample the energy spectrum at multiple regions. This allows higher spectral resolution, enabling the identification of material specific spectral characteristics, such as the K-edge signature of the contrast agent (5,15–18). This is particularly interesting as the K-edge energies of contrast agents that contain heavy elements such as gadolinium, ytterbium, bismuth, or gold are within the clinical X-ray tube spectrum (1,17,19–21). The material decomposition can then be extended to include the K-edge of the contrast agents as a separate basis, allowing for multicolor imaging (8,22).

However, despite its high spectral resolution, it is still unknown whether the SPCCT system can distinguish and quantify two contrast agents when they are mixed within the same volume (either one with high and the other with low K-edge energy, or both with high K-edge energies). In this study, we proposed to fill this gap in our knowledge by performing multicolor

imaging with SPCCT and detect as well as quantify iodine, gadolinium and gold in different mixtures, with a single scan.

## MATERIALS AND METHODS

*Spectral photon-counting computed tomography (SPCCT)*

The modified clinical base, small field-of-view (FOV) SPCCT prototype system (Philips Healthcare, Israel) is based on a semiconductor detector technology operated in single photon-counting mode with energy discrimination (15,23). The system is operated as a 9-row scanner with an effective z-collimation of about 2.5 mm in the iso-center and an imaging FOV of 168 mm in-plane. Axial scans over 360 degrees were performed at 100 mA tube current and 120 kVp tube voltage with a scanner rotation time of 1 s and 2400 projections per rotation. Each pixel in each projection reading consisted of a group of five integer numbers, representing the number of crossings (from low to high) of the analog pulse signal of predefined energy thresholds. For low flux and negligible pile-up, these numbers corresponded to the counts in single-ended pulse-height windows that resulted from the convolution of the x-ray spectrum and the detector response function. Due to the small FOV and the small z-collimation of the prototype, scatter effects were much smaller than for clinical CT. Thus, the detector of this prototype was not equipped with an anti-scatter grid. This system had 5 thresholds that could be adjusted in order to allow photon energy–based discrimination of an element. In the cases of gadolinium and gold, we set 2 thresholds just below and above their K-edges, at 50.2 keV and 80.7 keV respectively, as was detailed in the study of E. Roessl *et al* (24). One additional energy threshold served as a noise threshold and was set to 30 keV. Hence, the energy thresholds were set at 30, 51, 64, 72, 85 keV for the gadolinium study, at 30, 53, 78, 83, 98 keV for the gold study, at 30, 51, 78, 83, 98 keV for the gold and gadolinium mixture study and at 30, 51, 64, 72, 85 keV for the iodine and gadolinium mixture study (Figure 1A-B). The energy thresholds for the iodine study were set at 30, 51, 64, 72, 85 keV even though iodine could not be efficiently detected by the K-edge technique due to the low numbers of photons around its K-edge energy (33.2 keV) (25).

*Phantom preparation*

A custom made polyoxymethylene cylindrical phantom with a diameter of 13 cm and 12 holes 1.5 cm in diameter was used. The contrast agents used in this study were: gold nanoparticles (AuNP, 65 mg/mL, size 18 nm, synthesized in house) (26); an iodinated agent (Iomeron 400 mg/mL, Bracco, Milan, Italy); and a gadolinium chelate (Multihance 0.5mmoL/mL, 78.625 mg/mL, Bracco, Milan, Italy). The samples were loaded into the phantom using 1.5 mL polypropylene centrifuge tubes. Two sets of 11 tubes were prepared, each containing two contrast agents diluted in PBS and mixed in varying proportions, as previously described (8,21) **(Figure 1C-D)**. The mixed agents were either gadolinium mixed with iodine or gadolinium mixed with gold. Eleven samples each of unmixed AuNP, gadolinium and iodine were also prepared in order to examine the effects of mixing the contrast agents on the measurement of their concentrations. The proportions of each pair of contrast agents were adjusted using a proper MATLAB code that allows calculations based on data obtained from imaging unmixed contrast agents. The concentrations (mg/mL) of the mixtures depended on the corresponding attenuation at 120 kVp. The target attenuation for each solution was chosen within the clinical standard for CT angiography applications, *i.e.* 280 HU, approximately (27). Hence, the concentrations of gadolinium, AuNP and iodine varied between 0 - 7.45 mg/mL, 0 - 10.4 mg/mL, and 0 - 8 mg/mL, respectively. The contrast agents' concentrations are presented in **Table 1**.

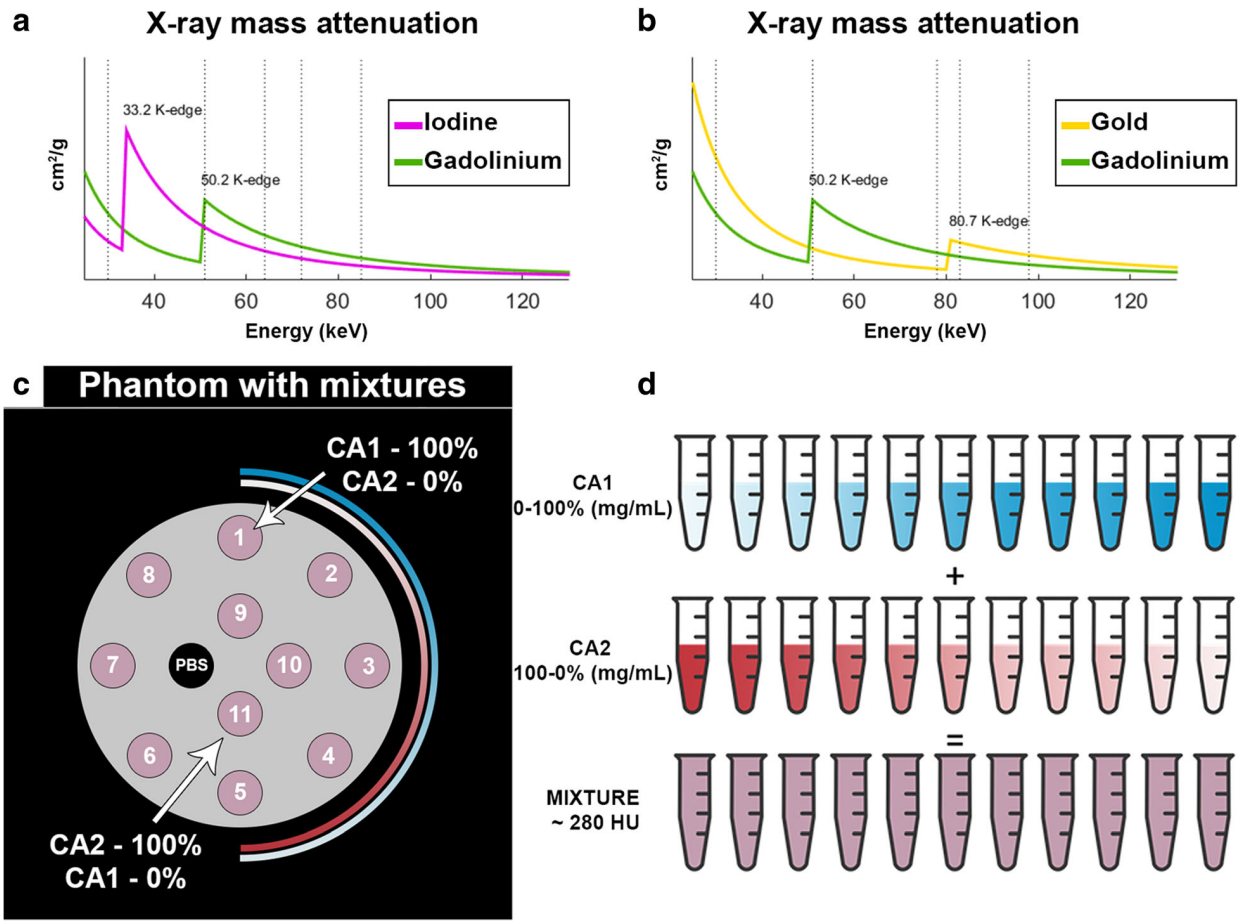


**Figure 1. (A-B) Representation of the K-edge energies and thresholds (dotted lines) used for the characterization of each element**. X-Ray mass attenuations of iodine (purple) and gadolinium (green) (A), as well as gold (yellow) and gadolinium (B) are shown with solid lines. **(C-D)** Eleven tubes of mixed contrast agents were prepared. The solutions were organized in a spiral, such that contrast agent 1 (in blue) was prepared at decreasing concentration while contrast agent 2 (in red) was prepared at increasing concentration. The tubes in the phantom have the same color on the schema because of their same-targeted CT attenuation values (~280 HU).

| Tube ID | Mixed gold and gadolinium | | Mixed iodine and gadolinium | | Gold only | Gadolinium only | Iodine only |
|---|---|---|---|---|---|---|---|
| | Gold (mg/mL) | Gadolinium (mg/mL) | Iodine (mg/mL) | Gadolinium (mg/mL) | Gold (mg/mL) | Gadolinium (mg/mL) | Iodine (mg/mL) |
| 1 | 0 | 7.46 | 8 | 0 | 0 | 0 | 8 |
| 2 | 0.98 | 6.67 | 7.2 | 0.79 | 0.98 | 0.79 | 7.2 |
| 3 | 1.95 | 5.89 | 6.4 | 1.57 | 1.95 | 1.57 | 6.4 |
| 4 | 3.25 | 5.1 | 5.6 | 2.36 | 3.25 | 2.36 | 5.6 |
| 5 | 4.22 | 4.32 | 4.8 | 2.75 | 4.22 | 2.75 | 4.8 |
| 6 | 5.2 | 3.53 | 4 | 3.53 | 5.2 | 3.53 | 4 |
| 7 | 6.17 | 2.75 | 3.2 | 4.32 | 6.17 | 4.32 | 3.2 |
| 8 | 7.15 | 2.36 | 2.4 | 5.1 | 7.15 | 5.1 | 2.4 |
| 9 | 8.13 | 1.57 | 1.6 | 5.89 | 8.13 | 5.89 | 1.6 |
| 10 | 9.43 | 0.79 | 0.8 | 6.67 | 9.43 | 6.67 | 0.8 |
| 11 | 10.4 | 0 | 0 | 7.07 | 10.4 | 7.07 | 0 |

**Table 1.** Concentrations of the three different contrast agents used in mixtures or individually diluted to obtain the 6 sets of 11 tubes.

*Data acquisition and spectral image reconstruction*

All solutions were scanned in the same phantom using the SPCCT prototype. The same SPCCT scan protocol was used, *i.e.* axial scan at a tube voltage of 120 kVp and tube current of 100 mAs, FOV 160 mm. For each pixel, a maximum likelihood estimator was used to derive an equivalent water-thickness per pixel from the photon counts in the five energy bins. Conventional images were then reconstructed from the water-thickness equivalent sinograms using a filtered back-projection algorithm. A material decomposition based on a forward projection model (per detector) and maximum likelihood, and using literature data (NIST) for the energy dependent attenuation of the base materials was used. For each phantom configuration, a specific material basis consisting of at least water and iodine, and - in case of their presence - gadolinium and gold was chosen. For example, a three-material water-iodine-gadolinium basis was used for the gadolinium-iodine study while a four-material water-iodine-gold-gadolinium basis was selected for the gadolinium-gold mixture study. The five multi-energy sinograms were then decomposed with a maximum-likelihood algorithm (16) into a set of up to four base material sinograms for the given material basis. Finally, the base material sinograms were individually reconstructed. The sinograms were individually reconstructed with a wedge reconstruction algorithm (28,29) on a $0.4 \times 0.4 \times 0.25$ $mm^3$ voxel grid. The reconstructed volume was then averaged over all eight slices to reduce noise. Hence, for each of the contrast agent's mixtures, a distinct set of contrast material images appropriate for each contrast agent

combination was generated within a few minutes for each slice, *i.e.* water, iodine, gadolinium and gold images. The water and iodine images were reconstructed for each solution no matter the content, and the gadolinium and gold images were reconstructed only in the presence of the material. The images were then analyzed without further post-processing apart from deringing, as well as smoothing of the contrast material images with a Gaussian kernel of 2 pixels width.

*Image analysis*

Image analysis was performed using MATLAB (R2015a, MathWorks, Inc.). The samples were automatically detected on conventional images and circular regions of interest (ROIs) were automatically drawn in the middle of each tube. The same ROIs were used on all images generated on a given data set and mean and standard deviation (SD) were computed for each ROI. Linear regression was performed between the prepared and measured concentrations for all solutions. The cross-contamination of the material decomposition, *i.e.* the amount of a measured material in other material image (*e.g.* amount of gadolinium and gold measured in water and iodine images), was measured for each material as the RMSE of its concentration in the other basis materials' ROIs, where no signal would be expected in the iodine image, and where mean value of 1000 mg/mL would be expected in the water image.

For each contrast agent in both unmixed and mixed solutions, the CNR relative to a homogeneous PBS tube was calculated according to the following equation:

$$\mathrm{CNR} = \frac{\left|\mathrm{mean\ concentration}_{\text{tube with contrast agent}} - \mathrm{mean\ concentration}_{\text{tube with PBS only}}\right|}{\mathrm{SD}_{\text{tube with PBS only}}}$$

In order to assess the impact of mixing the contrast agents, a reliability analysis between the non-mixed and the mixed measured concentrations was performed using intraclass correlation coefficients (ICC) and their 95 % confident intervals (CI). The statistical analyses were performed using SPSS statistical package version 24 (SPSS Inc, Chicago, IL) based on a mean rating for each contrast agent (k = 3 *e.g.* Gd, Gd+AuNP, Gd+I), 2-way mixed-effects model.

## RESULTS

As expected from the experimental design, different solutions of mixed contrast agents could not be differentiated on conventional images as all tubes had similar attenuations (279 ± 10 HU). However, we found that the contrast agents were accurately identified in the material images and that the water images showed only the material based water map in the solutions and in the phantom (**Figure 2).**

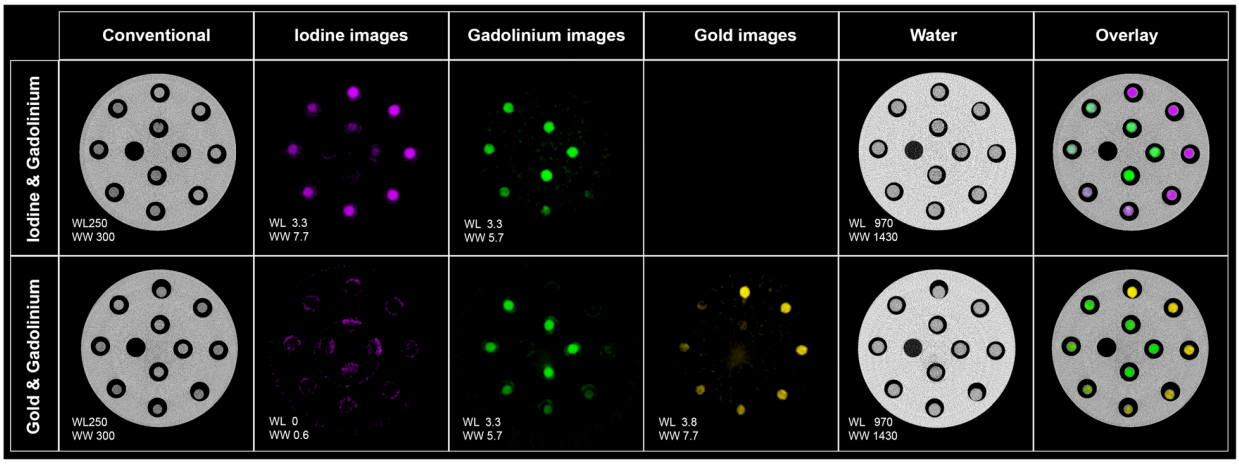


**Figure 2. Spectral photon-counting images of conventional, iodine (purple), gadolinium (green), gold (yellow) and water for both sets of mixed contrast agents.**
Top row: iodine – gadolinium mixture; bottom row: gold – gadolinium mixture; conventional image units are HU, and material images (water, iodine, gold, gadolinium) are mg/mL. Note that no gold image was generated from the material decomposition process for the iodine – gadolinium mixture, whereas an iodine image was generated from the material decomposition process for the gadolinium – gold mixture.

The correlations between the measured and prepared concentrations were strongly linear for all dilutions (all $R^2 \geq 0.97$). The slopes were close to one for the unmixed contrast agents' solutions ($0.98 \leq$ slope $\leq 1.04$), but were underestimated for the mixed contrast agents' solutions ($0.81 \leq$ slope $\leq 0.95$) (**Figures 3 and 4**). The underestimations were slightly more marked for the gadolinium – gold mixture (gadolinium slope = 0.81; gold slope = 0.90), than for the iodine – gadolinium mixture (gadolinium slope = 0.85; iodine slope = 0.95) (Figure 6). Additionally, the offset values were very low for single contrast agent solutions ($-0.13 \leq$ offset $\leq 0.22$ mg/mL) but most of the offset values were significantly different from zero when the contrast agents were mixed ($-0.68 \leq$ offset $\leq 0.89$ mg/mL) (**Table 2 and Figure 4**).

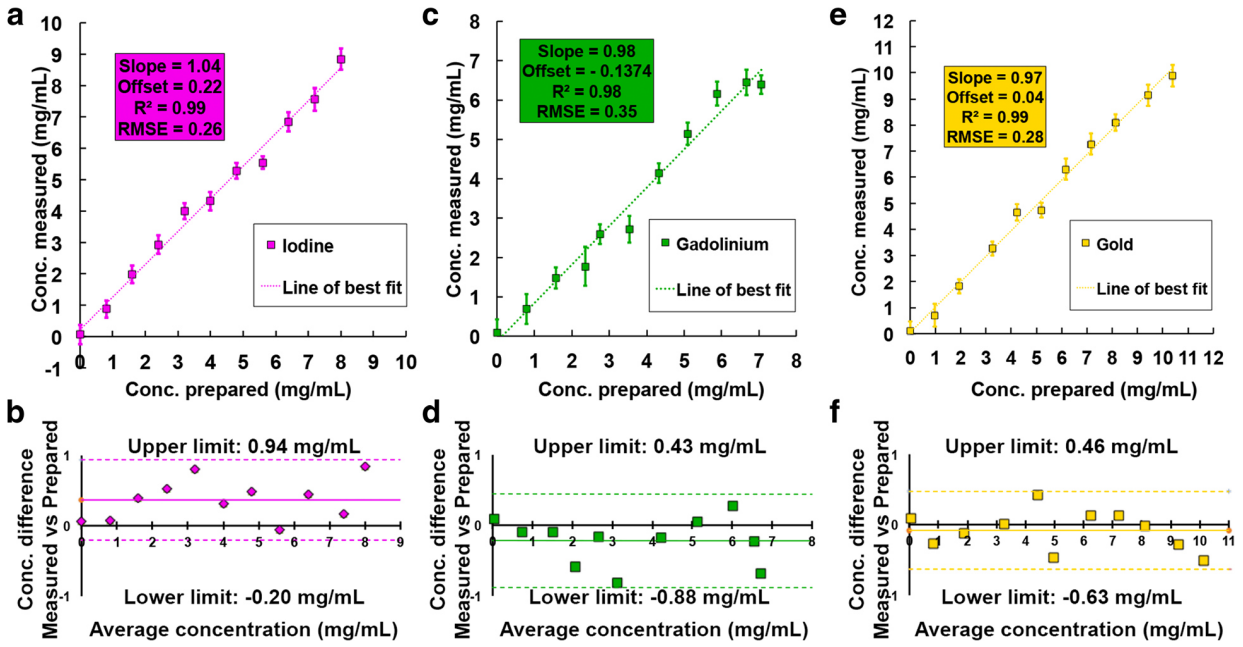


**Figure 3. Measurements of the concentrations of contrast agents in the unmixed solutions.** The concentrations of iodine (purple) (A, B), gadolinium (green) (C, D) and gold (yellow) (E, F) were measured in their respective unmixed solutions. A, C, E: Linear regression; B, D, F: Bland-Altman analysis. Note the linear correlations and the slope values approaching one for all contrast agents.

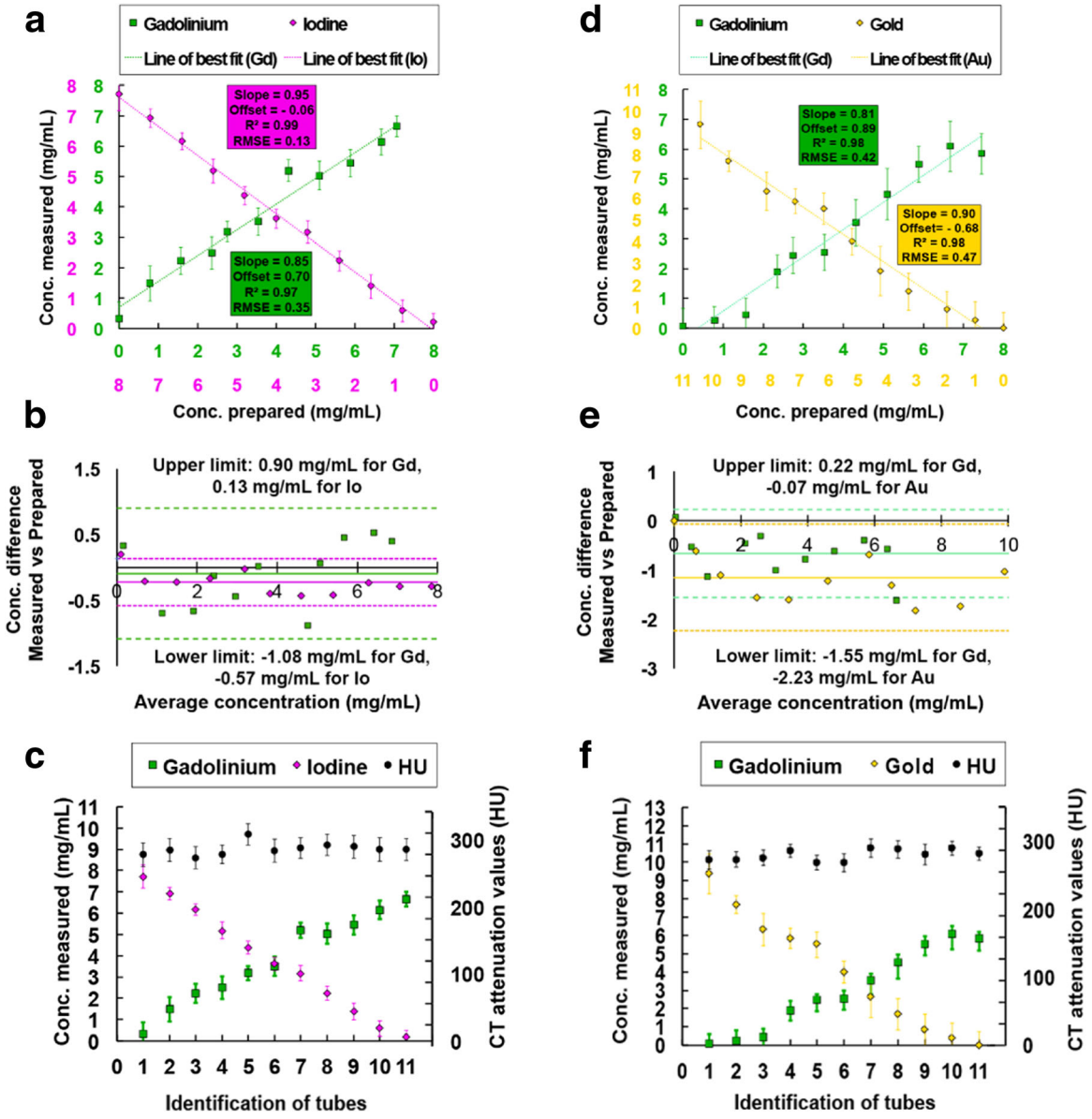


**Figure 4. Measurements of the concentrations of contrast agents and attenuation values in the mixed solutions.**

The concentrations of each contrast agent were measured within the gadolinium – iodine (A, B, C) and gadolinium – gold (D, E, F) mixtures. A, D: Linear regression; B, E: Bland-Altman analysis; C, F: graphs of the mean ± SD of attenuation values and concentrations. Note that, as expected, the measured concentrations in the tubes varied inversely between the two mixed contrast agents.

The ICC analysis showed a significant linear relation between prepared and measured concentrations indicating an excellent degree of reproducibility between each of the contrast agent measurements (gold single measure ICC = 0.987, 95% CI = 0.965 - 0.996; iodine single

measure ICC = 0.992, 95% CI = 0.978 - 0.998; gadolinium single measure ICC = 0.973, 95% CI = 0.929 - 0.992) (**Table 2**). Importantly, the linear relation indicates that offsets observed when contrast agents were mixed are not concentration dependent. These quantitative results are summarized in **Table 2 and 3**.

The water images did not show any cross-contamination neither for the unmixed or the mixed solutions, as confirmed by the very low RMSE values (RMSE ≤ 0.08 mg/mL). Similarly, the iodine images did not show any cross-contamination for the unmixed solutions, despite a RMSE at 0.33 mg/mL for the gadolinium dilutions due to negative iodine measured concentrations. Conversely, the iodine images showed some cross-contamination for the gold – gadolinium mixture, as confirmed by a RMSE at 0.34 mg/mL and by the measured concentrations of iodine. The cross-contamination in iodine image increased with increasing concentrations of gadolinium but not gold (**Table 3 and Figure 5).**

The CNR values observed for each contrast agent were higher for the unmixed solutions, in particular for the gold – gadolinium mixture (unmixed gold CNR slope = 2.80; unmixed gadolinium CNR slope = 3.11; gold – gadolinium mixture: gold CNR slope = 1.37, gadolinium CNR slope = 1.67) (**Figure 6**). Furthermore, the CNR slope for unmixed iodine was better than for the gadolinium – iodine mixture (unmixed iodine CNR slope = 3.45; gadolinium – iodine mixture: iodine CNR slope = 3.20).

| Image | Mixed gold and gadolinium | | Mixed iodine and gadolinium | | Gold only | Gadolinium only | Iodine only |
|---|---|---|---|---|---|---|---|
| | Gold | Gadolinium | Iodine | Gadolinium | Gold | Gadolinium | Iodine |
| Slope | 0.90 | 0.81 | 0.95 | 0.81 | 0.97 | 0.98 | 1.04 |
| Offset | -0.68 | 0.89 | -0.06 | 0.88 | 0.04 | -0.13 | 0.22 |
| $R^2$ | 0.98 | 0.98 | 0.99 | 0.98 | 0.99 | 0.98 | 0.99 |
| RMSE | 0.47 | 0.42 | 0.13 | 0.35 | 0.28 | 0.35 | 0.26 |
| 95% CI | 0.83–1 | 0.86–1.1 | 0.96–1 | 0.77–1 | 0.9–0.97 | 0.82–1 | 0.99–1 |

*RMSE* root mean square error, *CI* confidence interval

**Table 2.** Linear regression coefficients of each reconstructed image from the different CA mixture and of the CA only solutions.

| Image | Mixed gold and gadolinium | | Mixed iodine and gadolinium | Gadolinium | | Gold | | Iodine |
|---|---|---|---|---|---|---|---|---|
| | Water | Iodine | Water | Water | Iodine | Water | Iodine | Water |
| RMSE | 0.08 | 0.34 | 0.01 | 0.01 | 0.33 | 0.01 | 0.18 | 0.01 |

**Table 3** Root mean square errors coefficients of water and iodine reconstructed images from the different unmixed and mixed solutions.

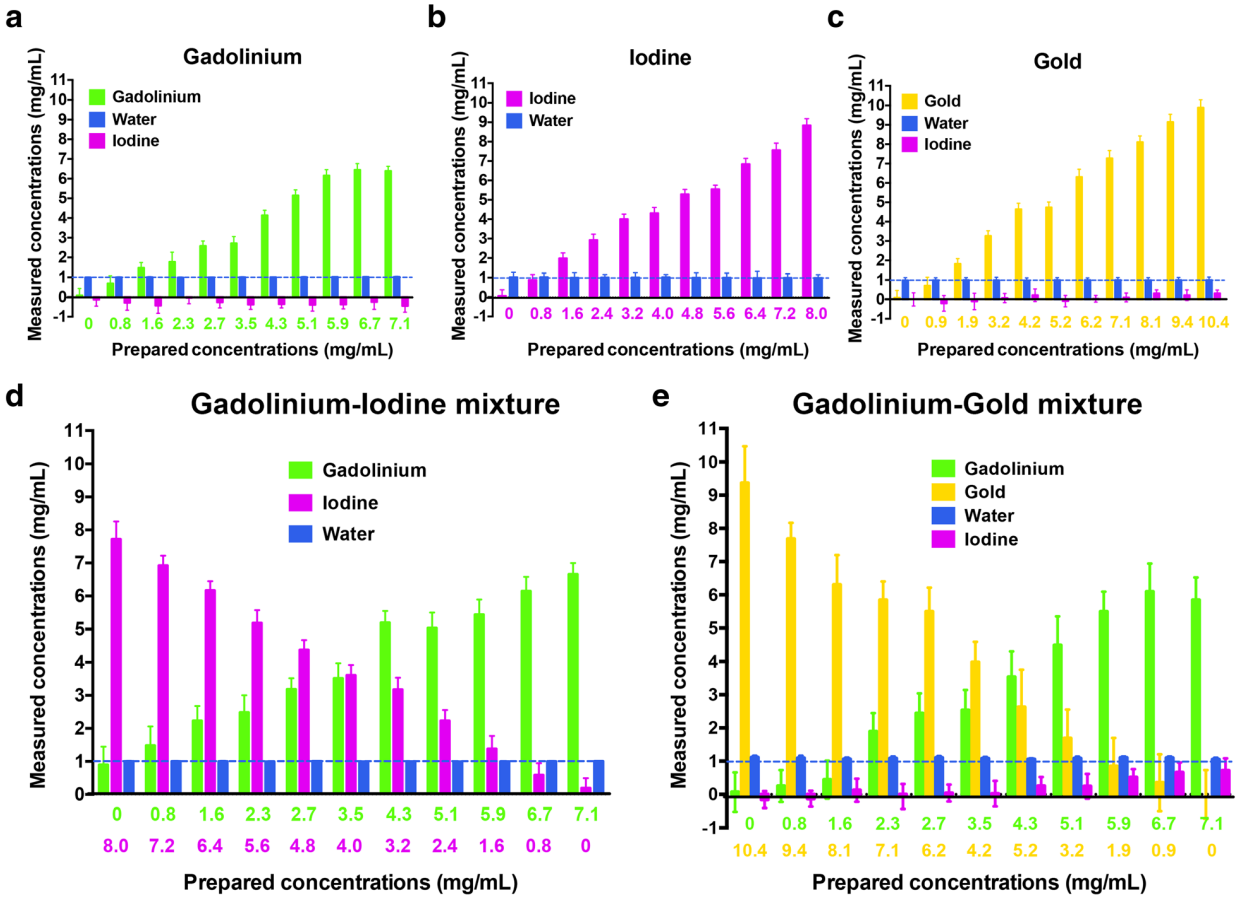


**Figure 5. Cross-contamination in the contrast agents' images.**

The graph bars show the concentrations (mean ± SD) of water (blue), iodine (purple), gadolinium (green), and gold (yellow) measured by the system, in each contrast material images, as a function of the prepared concentrations within the unmixed (A: gadolinium, B: iodine, C: gold) and mixed (D: gadolinium – iodine; E: gadolinium – gold) solutions. The blue dotted line represents the concentration of water expected in each solution (1000 mg/mL). Note the slight cross-contamination in the iodine image for the gadolinium – gold mixture that increases with increasing concentration of gadolinium but not gold.

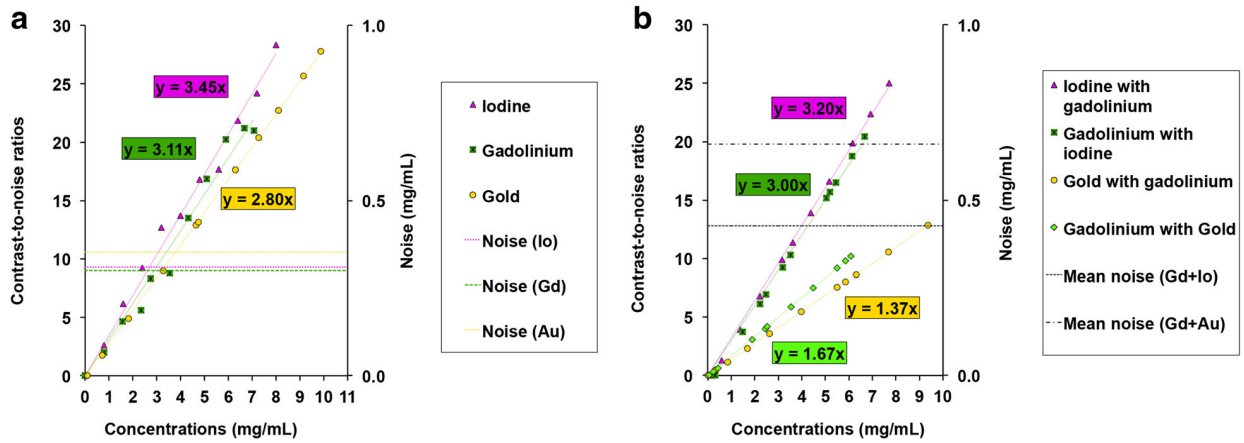


**Figure 6. Contrast-to-noise ratios of the contrast agents.**
The graphs represent the contrast to noise ratios values depending on the concentration of the contrast agent and the noise values of the contrast agents measured in their respective contrast material maps within the unmixed (A) and mixed (B) solutions. The dotted lines represent the noise measured in a tube filled with PBS only within the contrast material images. Mean noise is the mean of the noise measured within the two contrast material images of each mixture.

## DISCUSSION

Computed tomography is an imaging modality with excellent spatial resolution and fast acquisition times that has laid the foundation for SPCCT. In the present study, we demonstrate that SPCCT has the ability to separate two mixed contrasts agents qualitatively and quantitatively. Indeed, the SPCCT energy resolving detectors enable such spectral resolution that it is possible to distinguish different contrast agents' K-edge signatures, within the same voxel and at the same time. Consequently, separate quantity maps for each individual contrast agent can be generated.

Optical imaging is another method that allows the separation of different contrast materials in the same spatial location but it is limited by penetration depth (30). Similarly, single photon emission computed tomography and positron emission tomography permit the specific detection of a material but suffer from low spatial resolution and long acquisition times (31). Moreover, despite its good spatial resolution, MRI detects the non-linear effect of the contrast material on the surrounding protons, preventing the detection of the contrast material itself (32). Finally, while it has been previously shown that SPCCT can be used for absolute quantification

of unmixed multiple contrast agents *in vivo* (7,8,21,22,33,34), few studies have investigated the accuracy of the quantification (21,34).

Recent *in vitro* studies have reported the quantification of iodine and gadolinium contrast agents using dual energy CT (35,36). However, this technology can decompose the attenuations into at most two components because it can perform only two measurements per pixel. SPCCT, on the other hand, provides five photon-count measurements (five bins) per pixel, which theoretically allows the concomitant decomposition of the attenuations on a two to four materials basis; two non K-edge materials (*e.g.* water and iodine), and one or two K-edge materials (*e.g.* gadolinium and gold), given that their K-edge energies are in two different energy bins. Our results confirm this theory, as we were able to show an accurate affine response of the material decomposition process both for unmixed (iodine, gadolinium, and gold) and mixed (iodine – gadolinium and gadolinium – gold mixtures) solutions, despite slightly shifted offsets. Nevertheless, when two contrast agents were mixed, we observed an underestimation of the quantification of the contrast agents that was more marked for K-edge materials (*e.g.* gold and gadolinium). Similarly, mixing the two k-edge materials led to some cross-contamination in the iodine image. Another consequence of mixing the materials was the increase of noise and the decrease of the CNR of the materials, much more adversely affected for the K-edge materials, i.e. gadolinium and gold. Indeed, as a result we observed a two-fold decrease of the CNR for the mixture of gadolinium and gold demonstrating that the four material basis approach comes with a lower sensitivity performance limiting drastically the trade off between contrast and noise. These outcomes can be explained by the fact that including more components in the material decomposition process means more degrees of freedom for the maximum likelihood algorithm, leading to smaller signal per component, and therefore more noise and more noise induced bias. In addition, we observed that among the K-edge materials, the gadolinium image was more contrasted than the gold one. This can be explained by the fact that gadolinium beneficiates from a better balance of photons below and above its k-edge energy than gold in a 120 kVp beam, leading to a more accurate material decomposition.

The origins of all these imperfections can be explained by the noise on the photon counts, which propagates to noise in the decomposed sinograms, and ultimately to the material maps. In addition to the inherent quantum noise, physical effects such as pulse pile-up and charge sharing as well as inaccuracies in the spectral model of the system (e.g. X-ray tube spectrum, detector

response function) will further degrade the quantification results if not properly addressed in the forward model which is solved by the maximum likelihood decomposition (1,16). The decomposition and reconstruction algorithms are still under development. Quantification improvements are expected as more accurate models and further noise handling algorithms will be applied. For example, researchers are actively looking into including some of the still un-modeled physical effects, and enhancing the accuracy of the incident spectrum and detector response function (37,38). Additionally, mitigating the noise would probably require to use regularized iterative methods, either during the material decomposition process (39), during the reconstruction process (40), or in a one-step algorithm that would embed both processes (41).

Based on our results, and the fact that all SPCCT reconstructed images have a 100% spatial registration (13), using multiple contrast agents with different pharmacokinetics in the same biological system simultaneously can reasonably be considered. Several applications of such method in the vascular system can be considered. For example, different contrast agents injected sequentially within a single scan could allow the imaging of multiple uptake phases of a given tissue/organ (7,33). It could also be possible to simultaneously visualize the vascular lumen and wall in pathologies such as atherosclerosis by using a combination of specific and non-specific contrast agents (22). These applications would dramatically enhance the diagnostic capabilities and decrease the patients' exposure to radiation. Finally, for the past twenty years, increasing efforts have been directed toward *in vivo* imaging of gene expression and enzyme activity, particularly in oncology research. It would be interesting to develop new multi-atom contrast agents that could be modified or cleaved in targeted tissues to allow cellular activity imaging (42–44).

Today, however, the simultaneous use of multiple intravascular heavy metal-based contrast agents is still not approved clinically. Moreover, none of the K-edge candidates are approved for human use, *i.e.* the heavy atoms, even in the case of contrast agent based nanoparticles. As a consequence, further pharmacological evaluations of currently available agents (*e.g.* concomitant use of iodine and gadolinium), or the development of new contrast media are needed. Finally, the work we report here has been done on relatively simple phantoms using a preclinical SPCCT scanner. In order to extend our study to clinical applications, we are now using a machine scaled for clinical use and assessing its spectral capabilities under varying

conditions (tube currents and voltage) with phantom conditions closer to human characteristics (size, attenuation, FOV).

## Conclusion

The SPCCT prototype used in this study can qualitatively and quantitatively differentiate multiple contrast agents within the same solution, opening perspectives in clinical applications. However, to fully take advantage of the SPCCT multicolor imaging performance, new agents containing K-edge materials must be developed.

## REFERENCES

1. Schlomka JP, Roessl E, Dorscheid R, Dill S, Martens G, Istel T, et al. Experimental feasibility of multi-energy photon-counting K-edge imaging in pre-clinical computed tomography. Phys Med Biol. 2008;53(15):4031–47.

2. Cole LE, Ross RD, Tilley JM, Vargo-Gogola T, Roeder RK. Gold nanoparticles as contrast agents in x-ray imaging and computed tomography. Nanomed. 2015;10(2):321–41.

3. Hong SR, Chang S, Im DJ, Suh YJ, Hong YJ, Hur J, et al. Feasibility of single scan for simultaneous evaluation of regional krypton and iodine concentrations with dual-energy CT: an experimental study. Radiology. 2016;152429.

4. Altman. TU-E- 210A-03: A Double-Layer Detector, Dual-Energy CT—Principles, Advantages and Applications. Med Phys. 2009;36(6):2750–2750.

5. McCollough CH, Leng S, Yu L, Fletcher JG. Dual- and Multi-Energy CT: Principles, Technical Approaches, and Clinical Applications. Radiology. 2015;276(3):637–53.

6. Mongan J, Rathnayake S, Fu Y, Wang R, Jones EF, Gao D-W, et al. In vivo differentiation of complementary contrast media at dual-energy CT. Radiology. 2012;265(1):267–72.

7. Symons R, Krauss B, Sahbaee P, Cork TE, Lakshmanan MN, Bluemke DA, et al. Photon-counting CT for simultaneous imaging of multiple contrast agents in the abdomen: An in vivo study. Med Phys. 2017;44(10):5120–7.

8. Cormode DP, Si-Mohamed S, Bar-Ness D, Sigovan M, Naha PC, Balegamire J, et al. Multicolor spectral photon-counting computed tomography: in vivo dual contrast imaging with a high count rate scanner. Sci Rep. 2017;7(1):4784.

9. Si-Mohamed S, Bar-Ness D, Sigovan M, Cormode DP, Coulon P, Coche E, et al. Review of an initial experience with an experimental spectral photon-counting computed tomography system. Nucl Instrum Methods Phys Res. 2017;873:27–35.

10. Rathnayake S, Mongan J, Torres AS, Colborn R, Gao D-W, Yeh BM, et al. In vivo comparison of tantalum, tungsten, and bismuth enteric contrast agents to complement intravenous iodine for double-contrast dual-energy CT of the bowel. Contrast Media Mol Imaging. 2016;11(4):254–61.

11. Mongan J, Rathnayake S, Fu Y, Gao D-W, Yeh BM. Extravasated contrast material in penetrating abdominopelvic trauma: dual-contrast dual-energy CT for improved diagnosis--

preliminary results in an animal model. Radiology. 2013;268(3):738–42.

12. Goodsitt MM, Christodoulou EG, Larson SC. Accuracies of the synthesized monochromatic CT numbers and effective atomic numbers obtained with a rapid kVp switching dual energy CT scanner. Med Phys. 2011;38(4):2222–32.

13. Grosjean R, Sauer B, Guerra RM, Daudon M, Blum A, Felblinger J, et al. Characterization of human renal stones with mdct: advantage of dual energy and limitations due to respiratory motion. Am J Roentgenol. 2008;190(3):720–8.

14. Taguchi K, Iwanczyk JS. Vision 20/20: Single photon counting x-ray detectors in medical imaging. Med Phys. 2013;40(10):100901.

15. Roessl. Imaging performance of a photon-counting computed tomography prototype. CERN, Geneva, Switzerland; 2015.

16. Roessl E, Proksa R. K-edge imaging in x-ray computed tomography using multi-bin photon counting detectors. Phys Med Biol. 2007;52(15):4679–96.

17. Schirra CO, Brendel B, Anastasio MA, Roessl E. Spectral CT: a technology primer for contrast agent development. Contrast Media Mol Imaging. 2014;9(1):62–70.

18. Clark DP, Badea CT. Hybrid spectral CT reconstruction. PLOS ONE. 2017;12(7):e0180324.

19. Pan D, Roessl E, Schlomka J-P, Caruthers SD, Senpan A, Scott MJ, et al. Computed tomography in color: nanoK-enhanced spectral CT molecular imaging. Angew Chem Int Ed Engl. 2010;49(50):9635–9.

20. Pan D, Schirra CO, Senpan A, Schmieder AH, Stacy AJ, Roessl E, et al. An early investigation of ytterbium nanocolloids for selective and quantitative "multicolor" spectral CT imaging. ACS Nano. 2012;6(4):3364–70.

21. Si-Mohamed S, Cormode DP, Bar-Ness D, Sigovan M, Naha PC, Langlois J-B, et al. Evaluation of spectral photon counting computed tomography K-edge imaging for determination of gold nanoparticle biodistribution in vivo. Nanoscale. 2017;9(46):18246–57.

22. Cormode DP, Roessl E, Thran A, Skajaa T, Gordon RE, Schlomka J-P, et al. Atherosclerotic plaque composition: analysis with multicolor CT and targeted gold nanoparticles. Radiology. 2010;256(3):774–82.

23. Blevis IM, Altman A, Berman Y, Levinson R, Livne A, Steadman R. Introduction of Philips Preclinical Photon Counting Scanner and Detector Technology Development. IEEE Med

Imaging Conf. 2015;

24. Roessl E, Herrmann C. Cramér-Rao lower bound of basis image noise in multiple-energy x-ray imaging. Phys Med Biol. 2009;1307–18.

25. Roessl E, Brendel B, Engel KJ, Schlomka JP, Thran A, Proksa R. Sensitivity of photon-counting based K-edge imaging in x-ray computed tomography. IEEE Trans Med Imaging. 2011;30(9):1678–90.

26. Naha PC, Chhour P, Cormode DP. Systematic in vitro toxicological screening of gold nanoparticles designed for nanomedicine applications. Toxicol Vitro Int J Publ Assoc BIBRA. 2015;29(7):1445–53.

27. Loewe C, Becker CR, Berletti R, Cametti CA, Caudron J, Coudyzer W, et al. 64-Slice CT angiography of the abdominal aorta and abdominal arteries: comparison of the diagnostic efficacy of iobitridol 350 mgI/ml versus iomeprol 400 mgI/ml in a prospective, randomised, double-blind multi-centre trial. Eur Radiol. 2010;20(3):572–83.

28. Heuscher D, Brown K, Noo F. Redundant data and exact helical cone-beam reconstruction. Phys Med Biol. 2004;49(11):2219–38.

29. Grass M, Köhler T, Proksa R. 3D cone-beam CT reconstruction for circular trajectories. Phys Med Biol. 2000 Feb;45(2):329–47.

30. Kolste KK, Kanick SC, Valdés PA, Jermyn M, Wilson BC, Roberts DW, et al. Macroscopic optical imaging technique for wide-field estimation of fluorescence depth in optically turbid media for application in brain tumor surgical guidance. J Biomed Opt. 2015;20(2):26002.

31. Moses WW. Fundamental Limits of Spatial Resolution in PET. Nucl Instrum Methods Phys Res Sect Accel Spectrometers Detect Assoc Equip. 2011;648 Supplement 1:S236–40.

32. Ishida M, Sakuma H, Murashima S, Nishida J, Senga M, Kobayasi S, et al. Absolute blood contrast concentration and blood signal saturation on myocardial perfusion MRI: estimation from CT data. J Magn Reson Imaging JMRI. 2009;29(1):205–10.

33. Symons R, Cork TE, Lakshmanan MN, Evers R, Davies-Venn C, Rice KA, et al. Dual-contrast agent photon-counting computed tomography of the heart: initial experience. Int J Cardiovasc Imaging. 2017;33(8):1253–61.

34. de Vries A, Roessl E, Kneepkens E, Thran A, Brendel B, Martens G, et al. Quantitative spectral K-edge imaging in preclinical photon-counting x-ray computed tomography. Invest

Radiol. 2015;50(4):297–304.

35. van Hamersvelt RW, Willemink MJ, de Jong PA, Milles J, Vlassenbroek A, Schilham AMR, et al. Feasibility and accuracy of dual-layer spectral detector computed tomography for quantification of gadolinium: a phantom study. Eur Radiol. 2017;27(9):3677–86.

36. Pelgrim GJ, van Hamersvelt RW, Willemink MJ, Schmidt BT, Flohr T, Schilham A, et al. Accuracy of iodine quantification using dual energy CT in latest generation dual source and dual layer CT. Eur Radiol. 2017;27(9):3904–12.

37. Long Y, Fessler JA. Multi-material decomposition using statistical image reconstruction for spectral CT. IEEE Trans Med Imaging. 2014;33(8):1614–26.

38. Li Z, Leng S, Yu L, Yu Z, McCollough CH. Image-based Material Decomposition with a General Volume Constraint for Photon-Counting CT. Proc SPIE [Internet]. 2015 [cited 2018 Mar 29];9412. Available from: https://www.ncbi.nlm.nih.gov/pmc/articles/PMC4517482/

39. Ducros N, Abasca J, Sixou B, Rit S, Peyrin F. Regularization of Nonlinear Decomposition of Spectral X-ray Projection Images. Med Phy. 2017;

40. Sawatzky A, Xu Q, Schirra C, Anastasio M. Proximal ADMM for multi-channel image reconstruction in spectral X-ray CT. IEEE Trans Med Imaging. 2017;

41. Schmidt T, Barber R, Sidky E. A Spectral CT method to directly estimate basis material maps from experimental photon-counting data. IEEE Trans Med Imaging. 2017;

42. Ren G, Blum G, Verdoes M, Liu H, Syed S, Edgington LE, et al. Non-invasive imaging of cysteine cathepsin activity in solid tumors using a 64Cu-labeled activity-based probe. PloS One. 2011;6(11):e28029.

43. Louie AY, Hüber MM, Ahrens ET, Rothbächer U, Moats R, Jacobs RE, et al. In vivo visualization of gene expression using magnetic resonance imaging. Nat Biotechnol. 2000;18(3):321–5.

44. Gaikwad HK, Tsvirkun D, Ben-Nun Y, Merquiol E, Popovtzer R, Blum G. Molecular imaging of cancer using X-ray computed tomography with protease targeted iodinated activity-based probes. Nano Lett. 2018;18(3):1582–91.

# Chapter III

## *In vivo* spectral photon-counting CT imaging

## I. MONOCOLOR AND MULTICOLOR IMAGING *IN VIVO*

**Title: Multicolor spectral photon-counting computed tomography: *in vivo* dual contrast imaging with a high count rate scanner**

D.P. Cormode[1.], S. Si-Mohamed[2.3] (First author with equal contributions), D. Bar-Ness[2.3], M. Sigovan[2.3], P.C. Naha[1], J. Balegamire [4], F. Lavenne[5], P. Coulon[6], E. Roessl[7], M. Bartels[7], M. Rokni,[8] I.Blevis,[8] L. Boussel[2.3], P. Douek [2.3]

1. Department of Radiology, University of Pennsylvania, Philadelphia, PA, USA
2. Radiology Department, Hospices Civils de Lyon, Lyon, France
3. CREATIS, UMR CNRS 5220, Inserm U1044, University Lyon1 Claude Bernard, Lyon, France
4. LAGEP Laboratory, University Lyon 1 Claude Bernard, Lyon, France
5. CERMEP, Lyon, France
6. CT Clinical Science, Philips, Suresnes, France
7. Philips GmbH Innovative Technologies, Research Laboratories, Hamburg, Germany
8. Global Advanced Technologies, CT, Philips, Haifa, Israel

## ABSTRACT

A new prototype spectral photon-counting computed tomography (SPCCT) based on a modified clinical CT system has been developed. SPCCT analysis of the energy composition of the transmitted x-ray spectrum potentially allows simultaneous dual contrast agent imaging, however, this has not yet been demonstrated with such a system. We investigated the feasibility of using this system to distinguish gold nanoparticles (AuNP) and an iodinated contrast agent. The contrast agents and calcium phosphate were imaged in phantoms. Conventional CT, gold K-edge, iodine and water images were produced and demonstrated accurate discrimination and quantification of gold and iodine concentrations in a phantom containing mixtures of the contrast agents. *In vivo* experiments were performed using New Zealand White rabbits at several times points after injections of AuNP and iodinated contrast agents. We found that the contrast material maps clearly differentiated the distributions of gold and iodine in the tissues allowing quantification of the contrast agents' concentrations, which matched their expected pharmacokinetics. Furthermore, rapid, repetitive scanning was done, which allowed measurement of contrast agent kinetics with high temporal resolution. In conclusion, a clinical

scale, high count rate SPCCT system is able to discriminate gold and iodine contrast media in different organs in vivo.

## INTRODUCTION

Spectral photon-counting computed tomography (SPCCT) is a new imaging modality that is currently heavily investigated. SPCCT scanners use a standard polychromatic x-ray source and dedicated, photon-counting detectors that discriminate the transmitted photons based on their energy and separate them into several energy bins [1–7]. Placing the energy bin boundaries in close proximity to the K-edge energies of elements allows specific imaging of these elements, which is also known as K-edge imaging (Fig. 1A). This technology can be used to distinguish several different materials in the field of view simultaneously, referred to as multicolor CT imaging [8–10]. The contrast agents reported for this technique have been based on heavy atoms, due to their K-edge energies being within a region of high x-ray flux within the beams used (50-90 keV), such as gold, bismuth, gadolinium and ytterbium [10–17]. Moreover, the spectral information can be additionally used for material separation in a similar fashion to dual-energy CT [3,18], i.e. allowing the formation of water or iodine density maps.

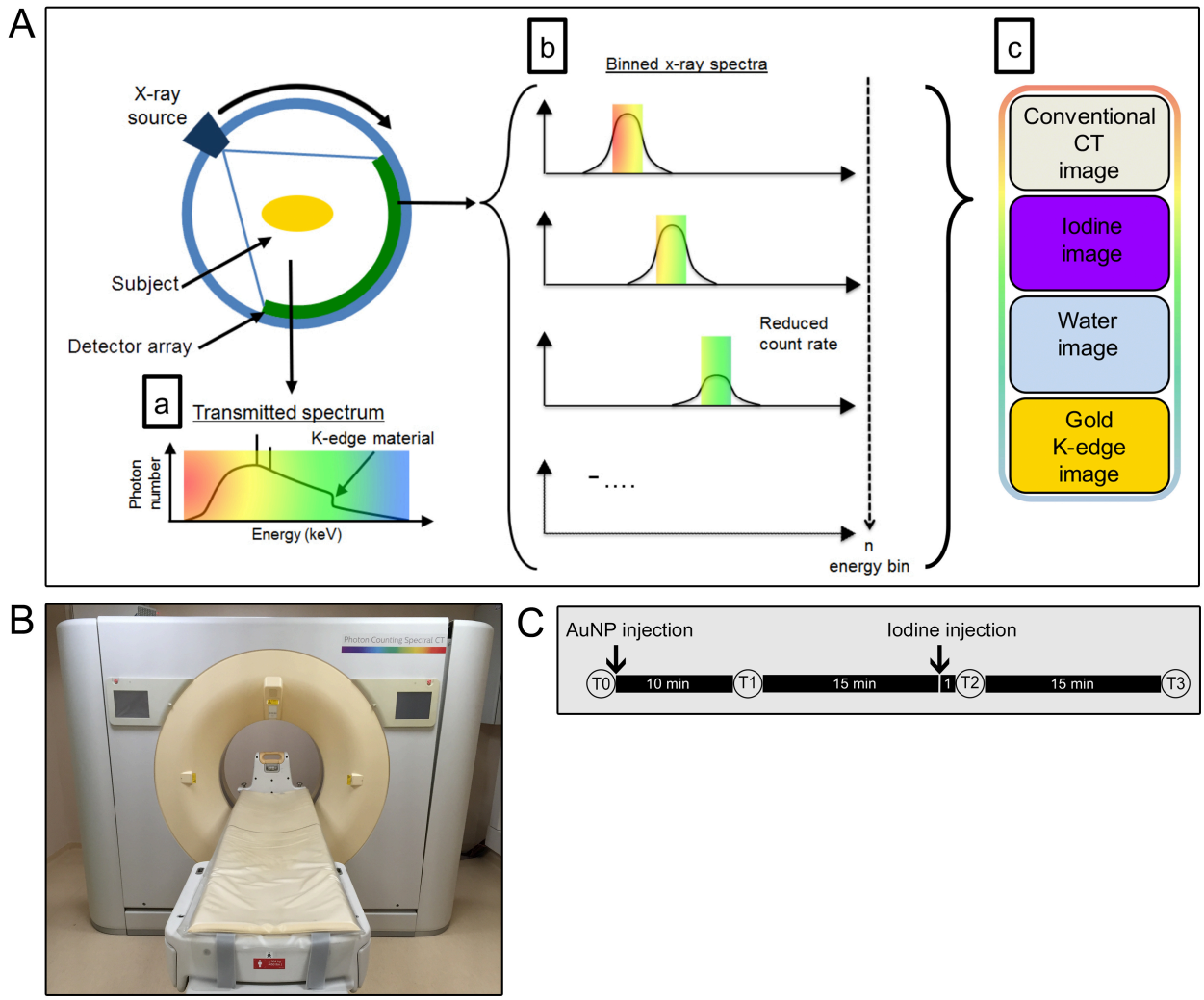


**Figure 1.** (A) Schematic depiction of SPCCT image formation. The transmitted spectrum (a) is divided by photon-counting detectors into multiple bins (b). These datasets are jointly processed to provide conventional images, and specific material decomposition images, e.g. water, iodine and gold images (c). (B) Photograph of the spectral photon-counting CT system used in this study. (C) Schematic depiction of the in vivo imaging protocol.

Spectral photon-counting CT scanners have been used to facilitate CT-based molecular imaging, as only a single scan, performed post-injection, is needed to detect accumulations of contrast agent in the target site, eliminating the need for comparison of pre- and post-injection images [8,13,17]. For example, SPCCT has been used to image macrophages inside atherosclerotic plaque with the use of gold nanoparticles, and simultaneously image the arterial lumen with an iodine contrast agent [19]. However, these previous results were obtained using SPCCT systems designed for small animal imaging and that had several technological limitations incompatible

with clinical imaging, such as low temporal resolution, very long acquisition time due to low count rate performance and limited detector collimation [20].

Recently, prototype clinical scale SPCCT scanners have been built [21]. Some of the characteristics of these scanners have been studied and initial patient imaging results have been reported [21–23]. However, it is not known if these clinical scale scanners retain the valuable ability to distinguish multiple materials simultaneously (e.g. iodine, gold and tissue). The purpose of this study was to investigate whether a small FOV prototype SPCCT scanner based on a modified clinical CT system (Fig. 1B) with high count rate performance was able to distinguish iodine and gold contrast media from endogenous tissues in a single scan.

## RESULTS

*AuNP characterization*

The average core diameter of the gold nanoparticles (AuNP) was found from transmission electron microscopy to be 12.5 +/- 2.4 nm (**Fig. 2**), while their mean hydrodynamic diameter was 18.3 +/- 0.5 nm, as determined by dynamic light scattering.

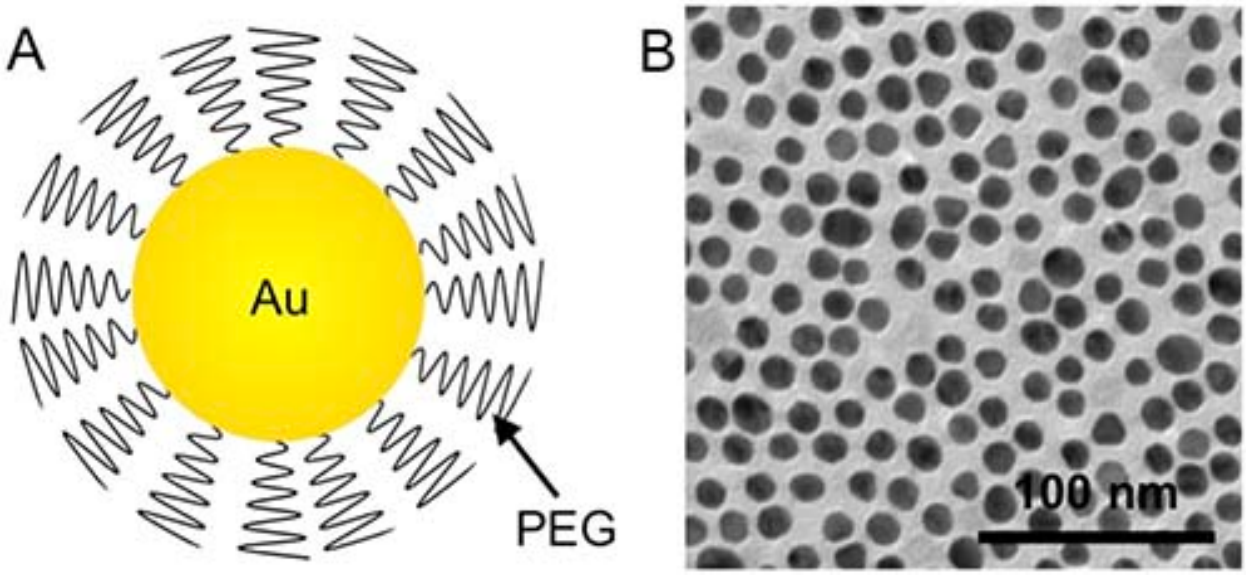


**Figure 2.** (A) Schematic representation of the gold nanoparticle used in this report. (B) TEM of the gold nanoparticles.

*Phantom imaging*

In order to study the material discriminating capabilities of this SPCCT scanner, we first imaged a phantom contained a range of concentrations of AuNP and iodine (Fig. 3). As can be

seen, the scanner could accurately determine the location of gold and iodine in the field of view (Fig. 3A,B). Since the plastic of the phantom is composed of elements close in atomic weight to those that make up water, both the plastic of the phantom and water in the vials appear in the water image. Discrimination between iodine and calcium was not attempted in this study. We therefore observed signal arising from the calcium phosphate sample in both the iodine and water images (Fig. 3B). There was a linear correlation between the contrast agent concentration and the signal produced in the element specific images (Fig. 3C). However, the concentration determined from the images was typically slightly underestimated compared to the actual concentration (for gold the slope of the line was 0.9, while for iodine it was 0.7). Bland-Altman plots for this phantom are shown in Supporting **Figure 1**.

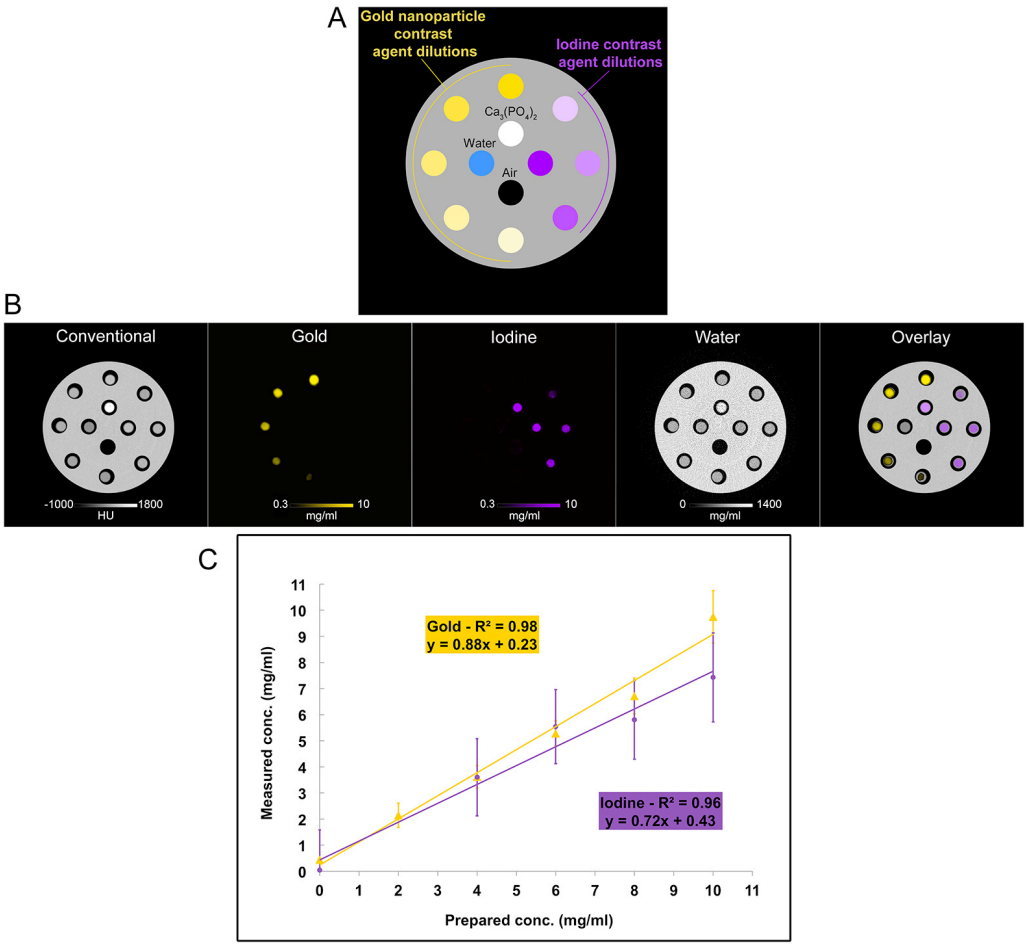


**Figure 3.** (A) Schematic of the phantom with unmixed solutions. (B) Conventional, gold, iodine, water and overlay images are depicted. (C) Graph of the expected and the measured concentrations.

In the second phantom, as expected, different solutions of mixed contrast agents could not be differentiated on conventional CT images as all samples had similar attenuations with an average of 279 ± 10 HU (Fig. 4). However, we found that the contrast agents were accurately identified in the gold and iodine specific images (Fig. 4B). As above, there was a linear correlation between the SPCCT measurements and the known concentrations of iodine and gold (Fig. 4C). However, the analysis for gold revealed an offset of -1.16 mg/ml. The phantom data indicates a detection limit close to 1 mg/ml of contrast agent, similar to conventional CT systems [24], but with the added benefit of material discrimination. Note that the size of the sample is typically slightly larger in the water image than in the gold or iodine images since the plastic rim of the tube appears in the water image, but not in the material specific images. Bland-Altman plots for this phantom are shown in Supporting Figure 2. The noise in the iodine image, for example, was 0.35 mg/ml, resulting in CNR of 24.9 in the sample with the highest concentration. Similar results were found for the gold images.

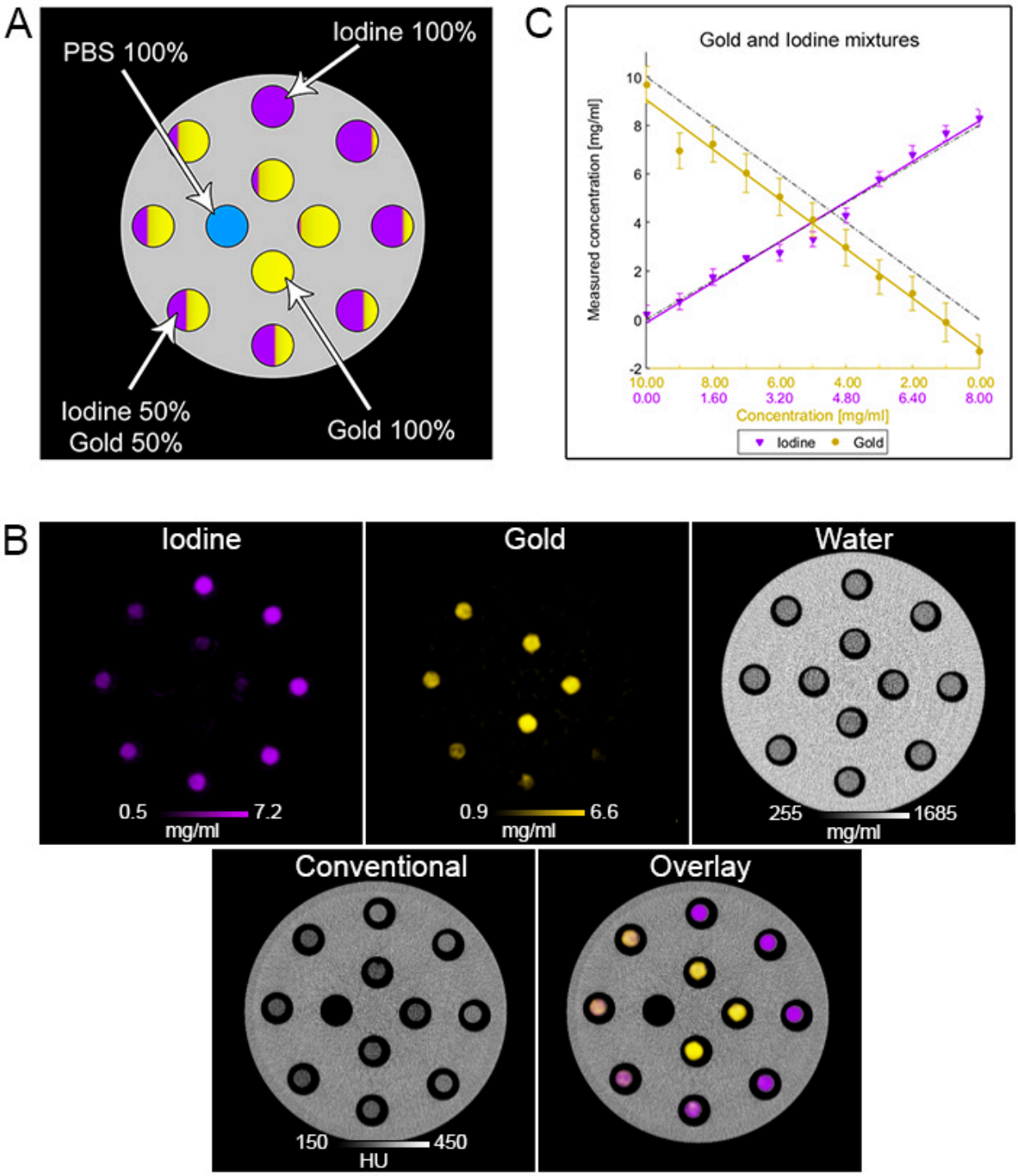


**Figure 4.** (A) Schematic of the phantom with mixed solutions. (B) Conventional, gold, iodine, water and overlay images are depicted. (C) Comparison of the expected and the measured concentrations.

*In vivo imaging*

In vivo testing of the material discrimination capabilities of the scanner was done via injecting rabbits with both AuNP and subsequently an iodinated contrast agent (see timeline in **Fig. 1C**). The agents used were selected such as they had differing pharmacokinetics and biodistributions (iodinated contrast media are swiftly excreted via the urine, while the AuNP used are a blood pool agent with a long blood residence time [25]). The difference in pharmacokinetics helped confirm the imaging results, as will be seen later. In vivo spectral CT images (conventional CT, gold, iodine, water and overlay) are shown in **Figs 5 and 6**.

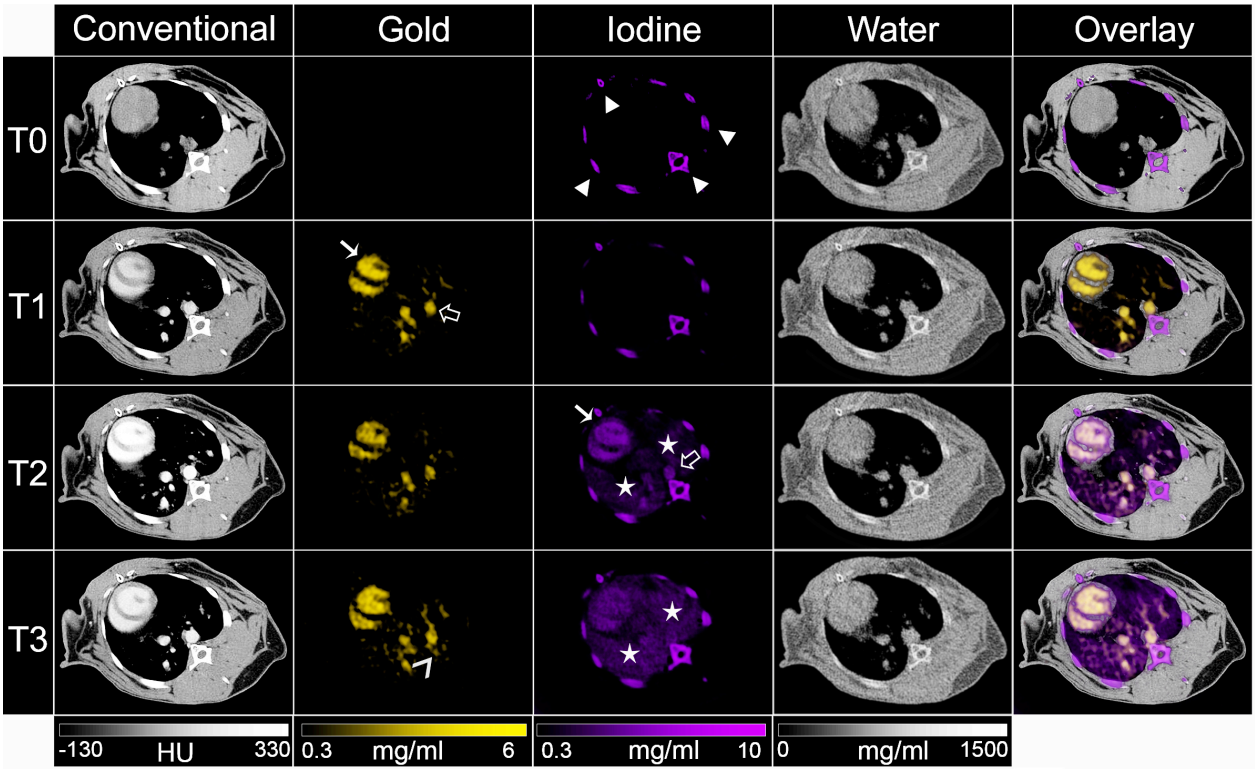


**Figure 5.** Photon-counting CT images of the chest of a rabbit. Conventional, gold, iodine, water and overlay images are shown for the three different time points. Arrowheads indicate bones, white arrows indicate the heart, black arrows indicate the aorta and stars indicate the lungs.

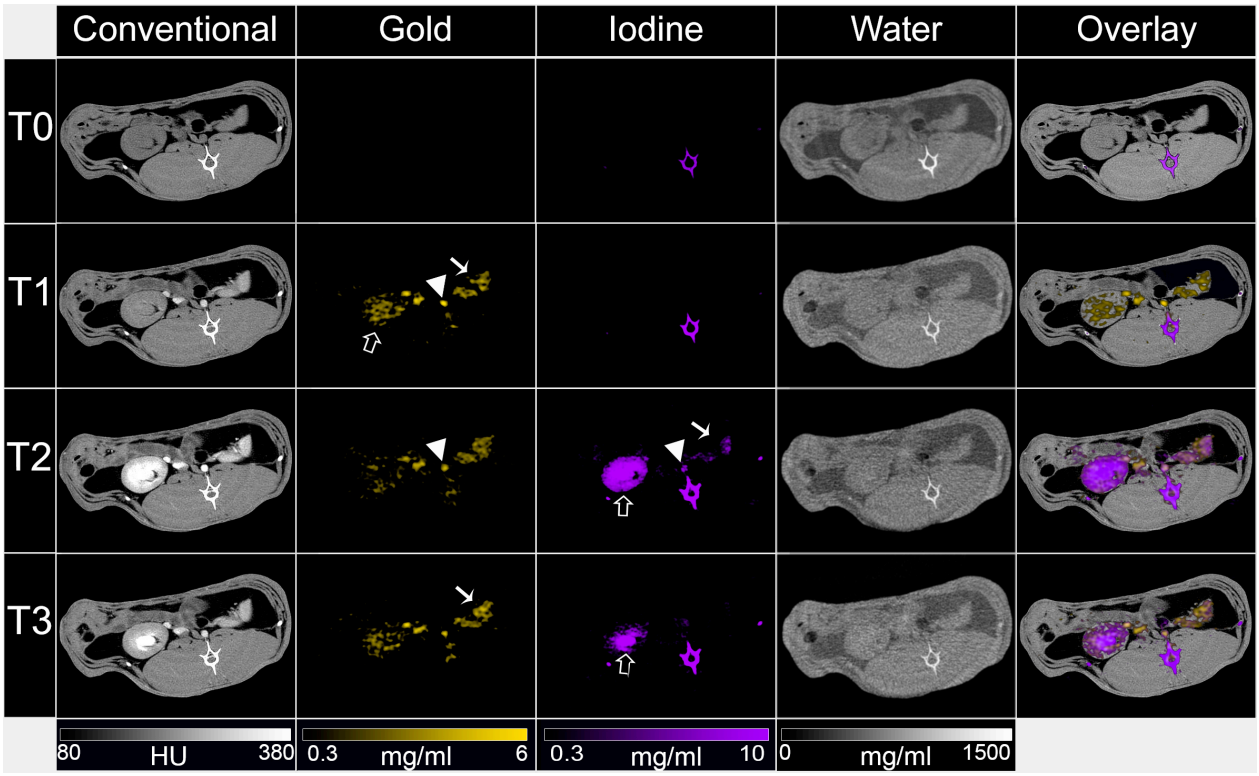


**Figure 6.** Photon-counting CT images of the abdomen of a rabbit. Conventional, gold, iodine, water and overlay images are shown for the three different time points. Arrowheads indicate aorta, white arrows indicate the spleen and black arrows indicate the kidney.

As can be seen from the images and from the image analysis, variations in attenuation were seen in the blood, kidney, spleen and renal pelvis at the different time points. For example, the attenuation in the blood increased from T0 to T1 after AuNP injection and increased further at T2, after iodine injection, before declining at T3. However, conventional CT images do not allow contrast arising from gold to be discriminated from that due to iodine. For example, at T3 in the abdomen (**Fig. 6**), contrast can be seen in the kidney and spleen, but it cannot be ascribed to one or the other or both of the contrast agents used.

Gold images allowed discrimination of gold rich matter from all other tissues and materials. Strong signals were observed in the blood vessels, which were sustained over time **(Figs 5 and 7**). The signal of gold was also persistent in the liver, spleen and the kidney (Table 1), which is likely due in part to the presence of blood in these organs, over this timeframe. A low signal was seen in the renal pelvis.

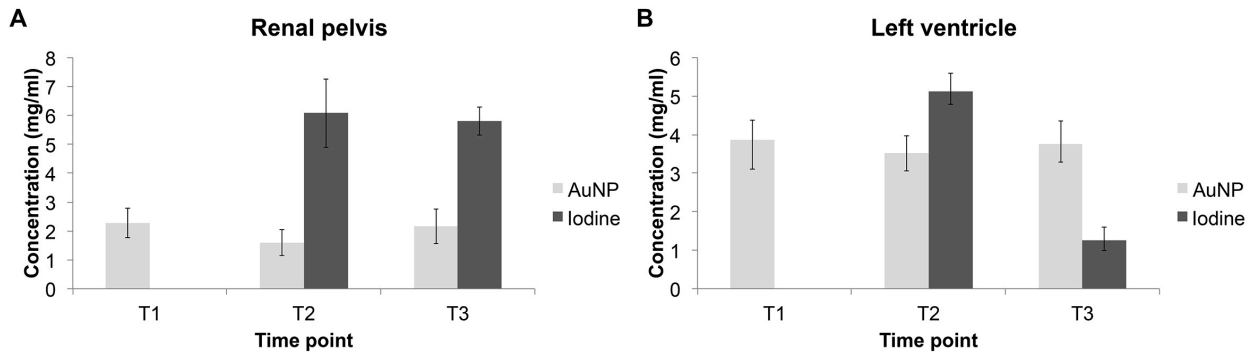


**Figure 7.** Concentrations of contrast agents in (A) the blood compartment and (B) the renal pelvis.

| Organ | Spectral Reconstruction | T1 | | T2 | | T3 | |
|---|---|---|---|---|---|---|---|
| | | Mean | SD | Mean | SD | Mean | SD |
| Left ventricle | Conventional (HU) | 139.93 | 21.89 | 310.07 | 30.91 | 167.52 | 19.34 |
| | Gold (mg/ml) | 3.86 | 0.75 | 3.53 | 0.47 | 3.75 | 0.47 |
| | Iodine (mg/ml) | □ | □ | 5.12 | 0.33 | 1.26 | 0.27 |
| Liver | Conventional (HU) | 77.17 | 23.90 | 118.30 | 30.34 | 92.31 | 29.27 |
| | Gold (mg/ml) | 1.80 | 0.92 | 1.31 | 0.50 | 1.28 | 0.94 |
| | Iodine (mg/ml) | □ | □ | 1.69 | 0.65 | 0.45 | 0.61 |
| Spleen | Conventional (HU) | 75.36 | 25.57 | 164.33 | 43.27 | 98.88 | 25.52 |
| | Gold (mg/ml) | 2.01 | 0.80 | 1.66 | 0.63 | 1.72 | 0.70 |
| | Iodine (mg/ml) | □ | □ | 2.80 | 0.72 | 0.88 | 0.50 |
| Kidney | Conventional (HU) | 63.77 | 24.81 | 139.17 | 28.84 | 109.98 | 24.40 |
| | Gold (mg/ml) | 1.49 | 1.63 | 1.41 | 0.67 | 1.53 | 0.63 |
| | Iodine (mg/ml) | □ | □ | 2.20 | 0.69 | 1.35 | 0.42 |
| Renal pelvis | Conventional (HU) | 74.93 | 22.61 | 230.51 | 60.93 | 260.74 | 26.92 |
| | Gold (mg/ml) | 2.28 | 0.51 | 1.60 | 0.45 | 2.16 | 0.60 |
| | Iodine (mg/ml) | □ | □ | 6.08 | 1.19 | 5.80 | 0.48 |

**Note - data are means ± standard deviation.**
**□ Absence of iodine contrast media**

**Table 1.** Values of attenuation and concentrations of gold and iodine in various organs.

The presence of iodine could be identified in iodine images, with strong signals in the blood and kidney at T2. These images showed that the signal from iodine in the blood quickly decreased, leaving signal in renal pelvis, matching the expected pharmacokinetics of iodine contrast media. In the kidney and the spleen, the signal decreased quickly from T2 to T3, likely reflecting the rapid clearance from the blood into the urine of this agent. As in the phantom imaging, bone created signal in the iodine and water images.

The speed of the scanner allowed us to perform multiple repeated scans to capture the pharmacokinetics of the iodine contrast agent immediately post injection. As can be seen in Figure 8, the bolus of the iodine injection can be tracked from the right ventricle to the pulmonary artery, the lung, and subsequently into the aorta. Such rapidity of scanning has not been demonstrated before to the best of our knowledge and is valuable to be able to assess arterial input function for potential quantification of abnormal tissue perfusion, such in the case of myocardial infarction.

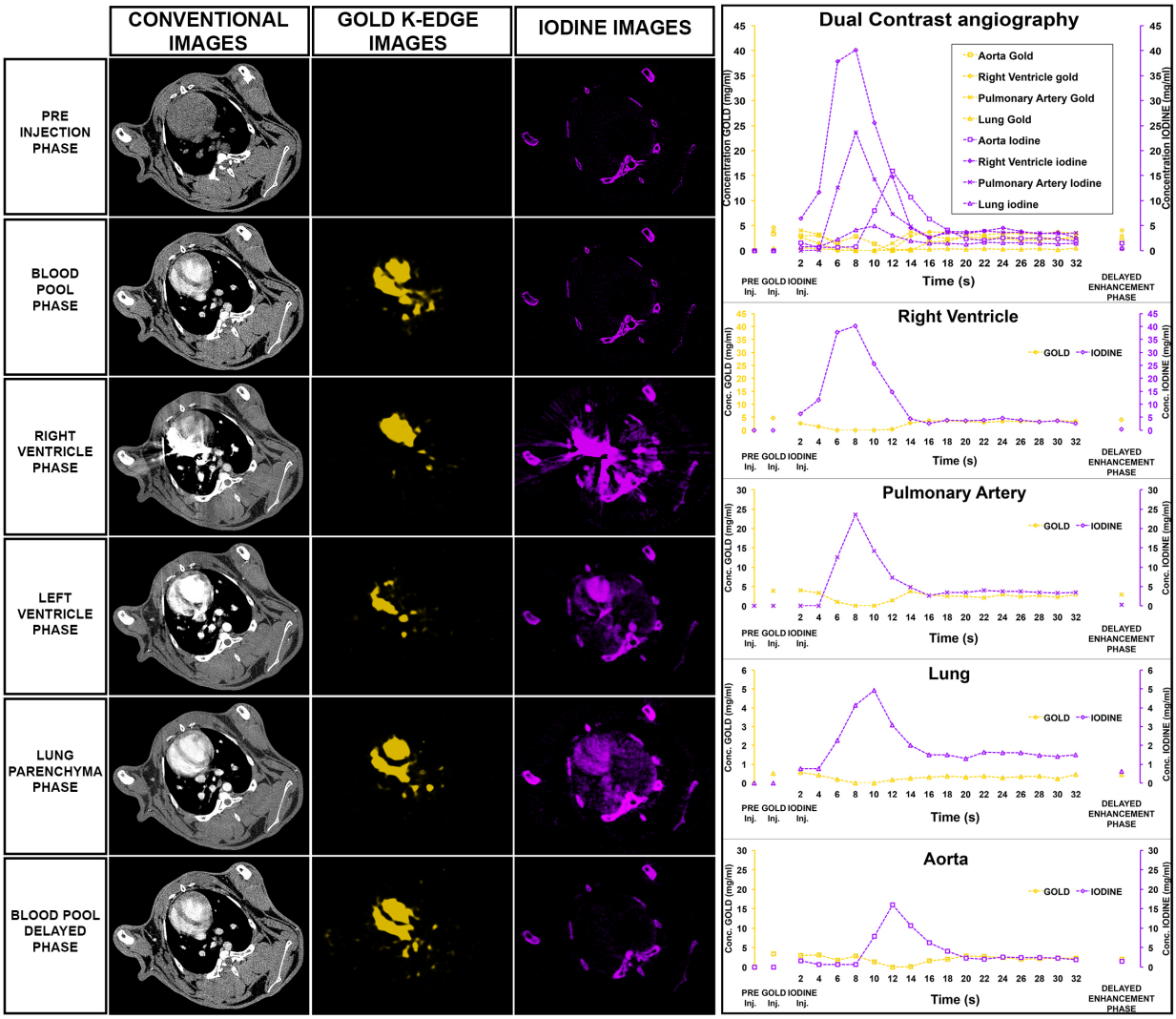


**Figure 8.** Conventional, gold k-edge and iodine material decomposition images at the level of the heart of a rabbit injected with AuNP and an iodine contrast agent at various timepoints (left). Quantification of the signal in various organs at the different timepoints (right).

## DISCUSSION

In this study, we demonstrated the ability of a small FOV prototype spectral photon-counting computed tomography system derived from a modified clinical CT system to simultaneously discriminate and quantify a blood pool agent (Au-NP) from an iodinated contrast agent, tissue, and calcium-rich matter on scans of phantoms and in rabbits in vivo. In conventional, single energy CT, data is acquired via detectors that measure the energy-integrated signals of x-ray photons, losing energy information of the individual photons and preventing specific discrimination of two contrast agents in one field of view [2,26,27]. There are several different configurations for dual-energy CT (dual x-ray tube, fast kVp switching and dual layer detector [18,28,29]), which can provide material specific images. However, these systems produce results of limited spectral performance because the high and low energy datasets are overlapping and the possibilities for material decomposition are limited to an analysis of only two basis images [2.3].

In spectral photon-counting CT, information is derived from photon-counting detectors that discriminate photon energies of each detected photon [2.8]. Therefore, an important advantage used herein of SPCCT over dual-energy CT is that the detected x-rays can be divided into multiple different energy windows to distinguish multiple materials. Additionally one or more boundaries of the energy bins can be freely adjusted to match the K-edge of contrast media such as AuNP or to best match the pathology being imaged [2,9,10,20,30]. Furthermore, it is generally expected that SPCCT imaging will have lower radiation doses than conventional CT [2.26].

Previous studies have focused on the capability of SPCCT to distinguish different materials. These studies were done using systems suited for small animals and were typically conducted postmortem due to the slow scanning speed of these systems [7.12.14.15]. A notable feature of the prototype SPCCT scanner described herein is that it performs axial scans in a clinically relevant time, i.e. one second. There has been a recent report of SPCCT imaging of humans, but multi-material decompositions were not done [21]. The ability to perform absolute quantification of two contrast agents, combined with excellent spatial resolution and fast acquisition times, makes SPCCT a unique imaging modality. SPECT and PET are limited by low spatial resolution [32] and long acquisition time. Finally, MRI has good spatial resolution but is unable to detect the contrast material itself; it detects the effect on the surrounding protons and this effect is not linearly dependent with the contrast agent concentration [33].

In this study, the scanned data was processed by material decomposition into the water/iodine/gold bases, therefore calcium-rich matter appears in the iodine and water material images, since all signal must be categorized as one or more of these three materials and the attenuation profiles of water and iodine are closest to that of calcium. K-edge imaging of iodine is not possible with this scanner, since it is a prototype for eventual clinical scanners and therefore low energy (15-30 keV) photons are not used, a distinction from earlier small animal scanners. Therefore, there are too few photons below the K-edge of iodine (33.2 keV) to allow K-edge imaging. Four material basis decomposition into water/iodine/gold/calcium could be done, but has drawbacks of reduced image quality, therefore we performed the afore-mentioned three material decomposition. Nevertheless, knowledge of anatomy and the synthesized conventional CT images can be used to determine whether signal is arising from calcified tissue rather than iodinated contrast media. The specific K-edge imaging of gold did not experience cross-talk from other components in the field of view, accurately discriminating the calcium-rich matter, all other tissue, and also the iodine contrast agent. When mixing two contrast agents, we observed a systematic underestimation of the gold concentration compared with the unmixed contrast agent. This is likely due to imperfections and systematic errors in the current system's hardware and software, such as the spectral forward model, i.e. uncertainties in the knowledge of the x-ray tube spectrum, as well as in the response function of the detector. Future work will seek to minimize such errors and improve quantification.

We were able to specifically image the biodistribution of an iodine contrast agent, detecting its presence in and quantifying its elimination from the blood vessels. We observed that the agent was rapidly excreted into the renal pelvis, matching the expected pharmacokinetics. We were also able to specifically image the biodistribution of a gold nanoparticle blood pool agent. We found persistently high concentrations of the gold nanoparticles in the blood vessels over the duration of the experiment (41 minutes), allowing both arterial and venous mapping. Previous reports indicate that such nanoparticles will remain in the circulation for several hours [25], allowing imaging to be done over a wide time window. SPCCT imaging allows the use of blood pool agents for delayed steady-state imaging, and can simultaneously perform first pass arterial imaging using a different contrast agent, such as iodine as we have demonstrated. For instance, it could be interesting to assess liver perfusion and blood mapping simultaneously. Further applications of blood pool contrast agents include detection of bleeding [34], visualization of tumor vasculature [35] and quantification of tissue blood volume [36]. Interestingly, we observed a slight decrease in gold

concentrations in the blood just after injection of iodine media contrast (T2), with a return to the initial level at T3, which could be due to a bolus effect from the iodine contrast media temporarily displacing the AuNP out of the organs or the reduction of gold signal observed from the second phantom (Fig. 4). We observed some gold signal in the renal pelvis, Since the size of this nanoparticle is above what is considered to be "renally excretable" (5.5 nm) [37] it seems unlikely that the agent is being filtered and excreted by the kidney, and chemical analysis indicated that gold was not present in the urine. Possibly this signal is due to AuNP in the blood present in this tissue. As a preclinical agent, an important issue for the translation of the gold nanoparticles is toxicity assessments. The formulation used in this study has been shown to be highly biocompatible by several groups [20.34], although testing in a non-rodent species would need to be done prior to clinical trials.

This was an early in vivo study to probe whether spectral imaging with two contrast media is feasible with a small FOV prototype spectral photon-counting computed tomography system derived from a modified clinical CT system; therefore the sample size we used was small. Moreover, we did not compare the measured concentrations in vivo with blood draws, and so we can only rely on the phantom measurements for calibration. Another limitation is that we did not study human subjects. The small FOV of the current scanner is another limitation, however a FOV typical of clinical scanners could be achieved via expansion of the detector array. The principal impediment is that AuNP are not currently clinically approved for use in humans. However, efforts to clinically translate metal-based nanoparticles that will provide spectral CT specific contrast are ongoing [39,40].

*Conclusion*

In summary, to the best of our knowledge, we have demonstrated for the first time the potential of the newly developed prototype spectral photon counting CT imaging system for qualitative and quantitative discrimination of two contrast agents in vivo, simultaneously over time, indicating the clinical impact of SPCCT in the field of "multicolor" imaging. This finding points to preclinical and clinical applications with various types of contrast agents to probe other biological processes and diseases, and also for multi-phase imaging in a single scan. In addition, it highlights the need to develop SPCCT specific contrast agents, which could expand the field of CT-based molecular imaging.

## MATERIALS/METHODS

*Gold nanoparticle preparation and characterization*

Polyethylene glycol–coated gold nanoparticles were prepared and characterized as previously described [38,41]. In brief, AuNP were synthesized in house using the Turkevich method, i.e. by reduction of gold chloride in boiling water via addition of sodium citrate. These nanoparticles were then capped with thiol-PEG-2000 and purified by washing in molecular weight cut-off concentrator tubes with phosphate-buffered saline. The AuNP were concentrated to about 65 mg/ml and sterilized via filtration before use. The nanoparticles were characterized with transmission electron microscopy, dynamic light scattering and inductively coupled plasma-optical emission spectroscopy.

*SPCCT Scanner*

The SPCCT scanner (Philips Healthcare, Haifa, Israel) is a prototype spectral photon-counting computed tomography system derived from a modified clinical CT system with a field-of-view (FOV) of 168 mm in-plane, and a z-coverage of 2 mm. It is equipped with energy-sensitive photon-counting detectors made of the direct conversion high band gap semiconductor cadmium zinc telluride. The electronics comprises 5 rate counters with 5 different configurable energy thresholds. For this study the thresholds were set to 30, 51, 78, 83 and 98 keV, chosen to give high differential sensitivity to materials with differing Z's, and in particular to analysis of gold, which has a K-edge of 80.7 keV. A full description of the SPCCT system can be found elsewhere[42]. Spectral photon-counting CT acquisitions were performed with a conventional X-ray tube at 100 mA tube current and 120 kVp tube voltage with a gantry rotation time of 1s and 2400 projections per rotation. A generalized schematic of how SPCCT systems operate is shown in Fig 1A. A photograph of the system is shown in Fig 1B.

*Material decomposition & quantitative measurements*

The material decomposition process was based on a method originally developed for dual-energy CT [43] that was extended to photon-counting CT [44], which is independent from the conventional images. The conventional CT images and material decomposition images were derived from SPCCT data using the detected information of the transmitted spectrum in all energy bins. The material decomposition from the multi-bin photon-counting data included a maximum-likelihood based material decomposition of the attenuation into three

material images, i.e. water, iodine and gold[45]. The material decomposition process provided water, iodine and gold images in mg/ml, allowing measurements of the concentration of a specific material. The conventional CT equivalent images are provided in Hounsfield units. Images were reconstructed as 0.25x0.25x0.25 mm voxels using conventional filtered back-projection without further post-processing and a standard Kernel filter.

*Image analysis*

For the phantom study, image analysis was performed using MATLAB (MathWorks. Inc.). Samples were automatically detected on conventional images and circular regions of interest were automatically drawn in the middle of each tube. The same ROIs were used on all images generated on a given data set and mean and standard deviation were computed for each ROI. In vivo images were analyzed using ImageJ software [46]. The attenuation values in Hounsfield Units (HU) and the concentrations of iodine and gold were recorded from a 2 mm slice, by manually drawing regions of interest (ROIs) of at least 50 pixels in all rabbits for selected organs (i.e. the left ventricle. right kidney. renal pelvis and spleen). The ROI's were defined on conventional CT images prior to retrieval of the gold and iodine concentrations per organ to avoid operator bias. After obtaining the respective concentrations, no adjustments of the ROIs were made. The ROIs were manually traced in the organs of interest and then were automatically copied on the gold specific K-edge and iodine material decomposition images. Representative ROIs used for image analysis are displayed in Supplementary Figure 3. The data presented is the absolute mean concentration of gold and iodine in mg/ml (mean ± standard deviation) among the five rabbits.

*Phantom imaging*

In order to study the material discriminating capabilities of the SPCCT system, we first performed phantom imaging on solutions of polyethylene glycol coated AuNP and an iodinated contrast agent (Iomeron 400 mg/ml. Bracco). A polyoxymethylene cylindrical phantom with a diameter of 13 cm and 12 holes of 1.5 cm in diameter was used. The first phantom contained a range of concentrations of AuNP and iodine contrast media, including 5 different concentrations of gold nanoparticles (2, 4, 6, 8 and 10 mg/ml), 4 concentrations of iodine contrast agent (4, 6, 8 and 10 mg/ml), a phosphate buffered saline (PBS) sample and a calcium phosphate sample (with an attenuation of 1860 HU), all prepared in 1.5 ml polypropylene centrifuge tubes (Dominique Dutscher SAS, Brumath, France) and inserted into the phantom. For the second phantom, eleven 1.5 ml polypropylene centrifuge tubes

were prepared, each contained a solution of AuNP mixed with the iodinated agent, in varying proportions and diluted in PBS. The proportions of each solution were adjusted based on data obtained from imaging unmixed contrast agent; the attenuation of each solution was 280 HU at 120 kVp in conventional CT images; the concentration of AuNP and iodine varied between 0-10.4 mg/ml, and 0-8 mg/ml respectively. The concentration ranges for the clinically available iodinated agent was based on current practice, i.e. below the maximum concentrations achievable during the arterial phase (~12-20 mg/ml) [33].

*Animal imaging*

This study was approved by the relevant Institutional Animal Care and Use Committee (Local Ethics Commitee: CeLYne C2EA42, Council Directive No. 2010/63/UE on the protection of animals used for scientific purpose) under the authorization number APAFIS#1732-2015091411181645v3 and performed in accordance with relevant guidelines and regulations. Five adult New Zealand White rabbits (Charles River, Canada, mean weight, 2.8 ± 0.6 kg; 2 females, 3 males; mean age, 6.1 ± 3.0 months) were sedated before imaging using a 20 mg/kg injection of ketamine (10 mg/ml, Merial, Lyon, France) and 0.25 mg/kg injection of medetomidine (1.0 mg/ml, Orion Pharma, Orion Corporation, Espoo, Finland) in order to maintain general anesthesia for 90 minutes. A 22-gauge catheter was placed in the ear vein for contrast agent administration, 3.5 ml/kg (about 12 ml) of AuNP were injected first, followed 25 minutes later by 0.9 ml/kg of Iomeron (3 ml). An initial acquisition was performed pre-injection (time point "T0"), followed by an acquisition at 10 minutes after injection of AuNP (time point "T1"). Subsequent acquisitions were performed 1 (time point "T2") and 15 minutes (time point "T3") after injection of iodine media contrast (Fig. 1C). Axial scans were acquired at the level of the heart, liver, spleen and the kidneys, allowing visualization of thoracic blood vessels, cardiac cavities, liver, spleen and renal pelvis. The pharmacokinetics of the iodine contrast agent were imaged by performing scans at the level of the heart every two seconds fifteen times after injection. Image analysis is described above.

*Data Analysis Statistics*

For the phantom study, linear regression was used to assess the correlation between the measured and the expected concentrations.

## REFERENCES


1. Iwanczyk, J. S. *et al.* Photon counting energy dispersive detector arrays for x-ray imaging. *IEEE Trans. Nucl. Sci.* **56,** 535–542 (2009).
2. Taguchi, K. & Iwanczyk, J. S. Vision 20/20: Single photon counting x-ray detectors in medical imaging. *Med. Phys.* **40,** 100901 (2013).
3. McCollough, C. H., Leng, S., Yu, L. & Fletcher, J. G. Dual- and multi-energy CT: principles, technical approaches, and clinical applications. *Radiology* **276,** 637–653 (2015).
4. Anderson, N. G. & Butler, A. P. Clinical applications of spectral molecular imaging: potential and challenges. *Contrast Media Mol. Imaging* **9,** 3–12 (2014).
5. Schlomka, J. P. *et al.* Experimental feasibility of multi-energy photon-counting K-edge imaging in pre-clinical computed tomography. *Phys. Med. Biol.* **53,** 4031–4047 (2008).
6. Blevis, I. Photon-counting detectors and clinical applications in medical CT imaging. in *Radiation Detectors for Medical Imaging* 169–192 (Jan S. Iwanczyk, 2015).
7. Taguchi, K. Energy-sensitive photon counting detector-based X-ray computed tomography. *Radiol. Phys. Technol.* **10,** 8–22 (2017).
8. Anderson, N. G. *et al.* Spectroscopic (multi-energy) CT distinguishes iodine and barium contrast material in MICE. *Eur. Radiol.* **20,** 2126–2134 (2010).
9. Si-Mohamed, S. *et al.* Review of an initial experience with an experimental spectral photon-counting computed tomography system. *Nucl. Instrum. Methods Phys. Res. Sect. Accel. Spectrometers Detect. Assoc. Equip.* doi:10.1016/j.nima.2017.04.014
10. Schirra, C. O., Brendel, B., Anastasio, M. A. & Roessl, E. Spectral CT: a technology primer for contrast agent development. *Contrast Media Mol. Imaging* **9,** 62–70 (2014).
11. Schirra, C. O. *et al.* Second generation gold nanobeacons for robust K-edge imaging with multi-energy CT. *J. Mater. Chem.* **22,** 23071–23077 (2012).
12. Cormode, D. P., Naha, P. C. & Fayad, Z. A. Nanoparticle contrast agents for computed tomography: a focus on micelles. *Contrast Media Mol. Imaging* **9,** 37–52 (2014).
13. Pan, D. *et al.* An early investigation of ytterbium nanocolloids for selective and quantitative 'multicolor' spectral CT imaging. *ACS Nano* **6,** 3364–3370 (2012).
14. Moghiseh, M. *et al.* Discrimination of multiple high-Z materials by multi-energy spectral CT– A phantom study. *JSM Biomed. Iaging Data Pap.* (2016).
15. Baturin, P., Alivov, Y. & Molloi, S. Spectral CT imaging of vulnerable plaque with two independent biomarkers. *Phys. Med. Biol.* **57,** 4117–4138 (2012).

16. Clark, D. P., Ghaghada, K., Moding, E. J., Kirsch, D. G. & Badea, C. T. In vivo characterization of tumor vasculature using iodine and gold nanoparticles and dual energy micro-CT. *Phys. Med. Biol.* **58,** 1683–1704 (2013).

17. Pan, D. *et al.* Computed tomography in color: nanoK-enhanced spectral CT molecular imaging. *Angew. Chem. Int. Ed Engl.* **49,** 9635–9639 (2010).

18. Agrawal, M. D. *et al.* Oncologic applications of dual-energy CT in the abdomen. *RadioGraphics* **34,** 589–612 (2014).

19. Cormode, D. P. *et al.* Atherosclerotic plaque composition: analysis with multicolor CT and targeted gold nanoparticles. *Radiology* **256,** 774–782 (2010).

20. de Vries, A. *et al.* Quantitative spectral K-edge imaging in preclinical photon-counting x-ray computed tomography. *Invest. Radiol.* **50,** 297–304 (2015).

21. Pourmorteza, A. *et al.* Abdominal imaging with contrast-enhanced photon-counting CT: First human experience. *Radiology* **279,** 239–245 (2016).

22. Gutjahr, R. *et al.* Human imaging with photon counting-based computed tomography at clinical dose levels: contrast-to-noise ratio and cadaver studies. *Invest. Radiol.* **51,** 421–429 (2016).

23. Yu, Z. *et al.* Initial results from a prototype whole-body photon-counting computed tomography system. *Proc. SPIE-- Int. Soc. Opt. Eng.* **9412,** (2015).

24. Galper, M. W. *et al.* Effect of computed tomography scanning parameters on gold nanoparticle and iodine contrast. *Invest. Radiol.* **47,** 475–481 (2012).

25. Cai, Q.-Y. *et al.* Colloidal gold nanoparticles as a blood-pool contrast agent for X-ray computed tomography in mice. *Invest. Radiol.* **42,** 797–806 (2007).

26. Fleischmann, D. & Boas, F. E. Computed tomography--old ideas and new technology. *Eur. Radiol.* **21,** 510–517 (2011).

27. Shikhaliev, P. M. & Fritz, S. G. Photon counting spectral CT versus conventional CT: comparative evaluation for breast imaging application. *Phys. Med. Biol.* **56,** 1905–1930 (2011).

28. Gabbai, M., Leichter, I., Mahgerefteh, S. & Sosna, J. Spectral material characterization with dual-energy CT: comparison of commercial and investigative technologies in phantoms. *Acta Radiol.* **56,** 960–969 (2015).

29. Fuentes-Orrego, J. M. *et al.* New and evolving concepts in CT for abdominal vascular imaging. *Radiographics* **34,** 1363–1384 (2014).

30. Roessl, E. *et al.* Sensitivity of photon-counting based K-edge imaging in X-ray computed tomography. *IEEE Trans. Med. Imaging* **30,** 1678–1690 (2011).

31. Yu, Z. *et al.* How low can we go in radiation dose for the data-completion scan on a research whole-body photon-couting computed tomography system. *J. Comput. Assist. Tomogr.* **40,** 663–670 (2016).

32. Moses, W. W. Fundamental limits of spatial resolution in PET. *Nucl. Instrum. Methods Phys. Res. Sect. Accel. Spectrometers Detect. Assoc. Equip.* **648 Supplement 1,** S236–S240 (2011).

33. Ishida, M. *et al.* Absolute blood contrast concentration and blood signal saturation on myocardial perfusion MRI: estimation from CT data. *J. Magn. Reson. Imaging JMRI* **29,** 205–210 (2009).

34. Williams, J. & Vasanawala, S. S. Active gastrointestinal hemorrhage identification by blood pool contrast-enhanced magnetic resonance angiography. *Pediatr. Radiol.* **41,** 1198–1200 (2011).

35. Popovtzer, R. *et al.* Targeted gold nanoparticles enable molecular CT imaging of cancer. *Nano Lett.* **8,** 4593–4596 (2008).

36. Giovagnoni, A. & Catalano, C. Application of blood-pool agents in visualization of peripheral vessels. *Eur. Radiol.* **17 Suppl 2,** B18-23 (2007).

37. Choi, H. S. *et al.* Renal clearance of quantum dots. *Nat. Biotechnol.* **25,** 1165–1170 (2007).

38. Naha, P. C., Chhour, P. & Cormode, D. P. Systematic in vitro toxicological screening of gold nanoparticles designed for nanomedicine applications. *Toxicol. In Vitro* **29,** 1445–1453 (2015).

39. Bonitatibus, P. J. *et al.* Preclinical assessment of a zwitterionic tantalum oxide nanoparticle X-ray contrast agent. *ACS Nano* **6,** 6650–6658 (2012).

40. Cheheltani, R. *et al.* Tunable, biodegradable gold nanoparticles as contrast agents for computed tomography and photoacoustic imaging. *Biomaterials* **102,** 87–97 (2016).

41. Blasi, F. *et al.* Radiation dosimetry of the fibrin-binding probe $^{64}$Cu-FBP8 and Its feasibility for PET imaging of deep vein thrombosis and pulmonary embolism in rats. *J. Nucl. Med. Off. Publ. Soc. Nucl. Med.* **56,** 1088–1093 (2015).

42. Rokni, M. *et al.* Conventional and spectral imaging performance of a small field-of-view spectral photon-counting computed tomography prototype scanner. *Submitt. Phys. Med. Biol.* (2017).

43. Stenner, P., Berkus, T. & Kachelriess, M. Empirical dual energy calibration (EDEC) for cone-beam computed tomography. *Med. Phys.* **34,** 3630–3641 (2007).

44. Brendel, B., Roessl, E., Schlomka, J.-P. & Proksa, R. Empirical projection-based

basis-component decomposition method. in **7258,** 72583Y–72583Y–8 (2009).

45. Roessl, E. & Proksa, R. K-edge imaging in x-ray computed tomography using multi-bin photon counting detectors. *Phys. Med. Biol.* **52,** 4679 (2007).

46. Schneider, C. A., Rasband, W. S. & Eliceiri, K. W. NIH Image to ImageJ: 25 years of image analysis. *Nat. Methods* **9,** 671–675 (2012).

## II. MOLECULAR MACROPHAGE K-EDGE IMAGING IN HEALTHY RABBIT

**Title: Evaluation of spectral photon counting computed tomography K-edge imaging for determination of gold nanoparticle biodistribution *in vivo***

S. Si-Mohamed[1,2], D.P. Cormode[3], D. Bar-Ness[2], M. Sigovan[1,2], P. C. Naha[3], JB. Langlois[4], L. Chalabreysse[5], P. Coulon[6], I. Blevis[7], E. Roessl[8], K. Erhard[8], L. Boussel[1,2], P. Douek[1,2]

[1] Radiology Department, Centre Hospitalier Universitaire, Lyon, France
[2] CREATIS, UMR CNRS 5220, Inserm U1044, University Lyon1 Claude Bernard, Lyon, France
[3] University of Pennsylvania, Department of Radiology, Philadelphia, PA, USA
[4] CERMEP-Imagerie du vivant, Lyon, France
[5] Centre Hospitalier Universitaire, Pathology Department, Lyon, France
[6] CT Clinical Science, Philips, Suresnes, France
[7] Philips, Global Advanced Technologies, CT, Haifa, Israel
[8] Philips GmbH Innovative Technologies, Research Laboratories, Hamburg, Germany

## ABSTRACT

Spectral photon counting computed tomography (SPCCT) is an emerging medical imaging technology. SPCCT scanners record the energy of incident photons, which allows specific detection of contrast agents due to measurement of their characteristic x-ray attenuation profiles. This approach is known as K-edge imaging. Nanoparticles formed from elements such as gold, bismuth or ytterbium have been reported as potential contrast agents for SPCCT imaging. Furthermore, gold nanoparticles have many applications in medicine, such as adjuvants for radiotherapy and photothermal ablation. Specific, longitudinal imaging of the biodistribution of nanoparticles would be highly attractive for their clinical translation. We therefore studied the capabilities of a novel SPCCT scanner to quantify the biodistribution of gold nanoparticles *in vivo*. PEGylated gold nanoparticles were used. Phantom imaging showed that concentrations measured on gold images correlated well with known concentrations (slope = 0.94, intercept = 0.18, RMSE = 0.18, $R^2$ = 0.99). The SPCCT system allowed repetitive and quick acquisitions *in vivo*, and follow-up of changes in the AuNP biodistribution over time. Measurements performed on gold images correlated with the Inductively coupled plasma-optical emission spectrometry (ICP-OES) measurements in the organs of interest (slope = 0.77, intercept = 0.47, RMSE = 0.72, $R^2$ = 0.93). TEM agreed with the imaging and ICP-OES in that much higher concentrations of AuNP were observed in the liver, spleen, bone marrow and lymph nodes (mainly in macrophages). In conclusion, we

found that SPCCT is capable of repetitive and non invasive determination of the biodistribution of gold nanoparticles *in vivo*.

**Keywords:** Spectral photon-counting computed tomography, blood pool, gold nanoparticles, biodistribution, pharmacokinetics, K-edge imaging, contrast agent

## INTRODUCTION

Since its introduction in the early 1970s, computed tomography (CT) has become the workhorse of diagnostic imaging owing to its cost effectiveness, wide availability, high spatial resolution, high temporal resolution, and diagnostic benefits. A current major area of research in CT is the use of photon counting detectors, referred to as spectral photon-counting CT (SPCCT), or as multicolor CT [1–4]. The photon-counting detectors are able to measure the energy of individual photons transmitted through the subject based on pulse height analysis, and to allocate this information between multiple energy thresholds, called bins, leading to energy-based attenuation profiles of tissue [3]. One of the strengths of SPCCT is its ability to specifically detect exogenous contrast media. This is possible due to edges in the x-ray attenuation profiles of elements such as gold, which have their K-edge binding energy in the relevant energy range of the x-ray spectrum (K-edge energy of gold is 80.7 keV). This approach is known as K-edge imaging and eliminates the need for imaging before and after injection, since the location of the contrast media can be determined solely from post-injection scan, streamlining the imaging and image analysis process. For instance, De Vries *et al*. investigated the feasibility and the accuracy of a small animal SPCCT scanner to determine the concentration and localization of iodine-based contrast agents in mice [5].

Clinical computed tomography relies on the use of iodinated contrast agents. However, these iodinated agents have a number of limitations. Some patients are hypersensitive to iodinated agents [6]. These agents are contra-indicated for use in patients with renal insufficiency, as their use in such patients can lead to further reduction in kidney function, an event known as contrast-induced nephropathy [7]. Moreover, they are non-specific with diffuse interstitial distribution and suffer from short imaging windows due to rapid renal clearance. Finally, the K-edge energy of iodine, 33.2 keV, is too low to be detected with clinical SPCCT systems, because of low x-ray flux at that point in the energy spectrum caused by high patient absorption. Thus there is a compelling need to develop novel contrasts agents for use with SPCCT.

Meanwhile, the field of nanoparticle contrast agents for CT has expanded rapidly over the past decade. Nanoparticles based on heavy elements, such as gold nanoparticles (AuNP), can overcome the drawbacks of small molecule iodinated CT contrast agents [8–13]. Several groups have demonstrated AuNP to be highly effective x-ray contrast agents, producing stronger contrast than iodinated agents, having the potential to circulate longer than iodinated contrast agents for improved blood pool imaging and possessing high biocompatibility [9,12,14–16]. In addition, gold nanoparticles have been shown to be potent contrast agents for SPCCT [17] and have been shown to be effective imaging agents for characterization of atherosclerosis with a preclinical system [18]. Moreover, gold nanoparticles and nanoparticles based on other heavy elements have been employed in a plethora of biomedical applications such as adjuvants for radiotherapy, photothermal ablation, drug delivery, photoacoustics, surface enhanced Raman imaging and others [19]. Methods that would allow the non-invasive assessment of the biodistribution of such agents at multiple time points would be highly valuable.

SPCCT has the potential to track the biodistribution and elimination of heavy element based agents over time via repeated scanning, sparing the need to sacrifice animals at each time point to perform *ex vivo* analyses or to perform radiolabeling. However, to the best of our knowledge, studying the biodistribution of agents over extended timeframes with SPCCT has not been previously reported. This was due to the limitations of early SPCCT systems, such as very long scan times [5] that prevented *in vivo* image acquisitions. SPCCT systems have now been developed with image acquisition times of 1 second that allow dynamic and repetitive imaging *in vivo*, such as a small field of vue (FOV) SPCCT prototype system derived from a modified clinical CT system [4].

The purpose of this study was to investigate the feasibility of SPCCT for specific characterization and quantification of a gold nanoparticle contrast agent's organ biodistribution *in vivo* over time.

## RESULTS

Nanoparticle preparation and characterization. AuNP were prepared from reduction of gold chloride with sodium citrate in boiling water, and then capped with thiol-PEG-2000. This process yielded gold nanoparticles (Fig. 1A) with a core size of 12.5 nm as found from transmission electron microscopy (TEM) (Fig. 1B) and mean hydrodynamic diameter of 18 nm as determined by dynamic light scattering (DLS). The concentration of the gold solution was determined from inductively coupled plasma-optical emission spectroscopy (ICP-OES)

to be 65 mg/ml. The pH was the same as that of iopamidol and phosphate buffered saline (PBS) solutions (7.46 ± 0.05). The viscosity of an x-ray contrast agent needs to be low to allow rapid injection and to avoid adverse side effects[20]. We therefore measured the viscosity of the AuNP. The dynamic viscosity of the gold nanoparticles was lower than that of iopamidol, being 1.14 ± 0.03 mPa/s and 1.28 ± 0.18 mPa/s respectively, indicating the gold nanoparticles have good viscosity for in vivo applications.

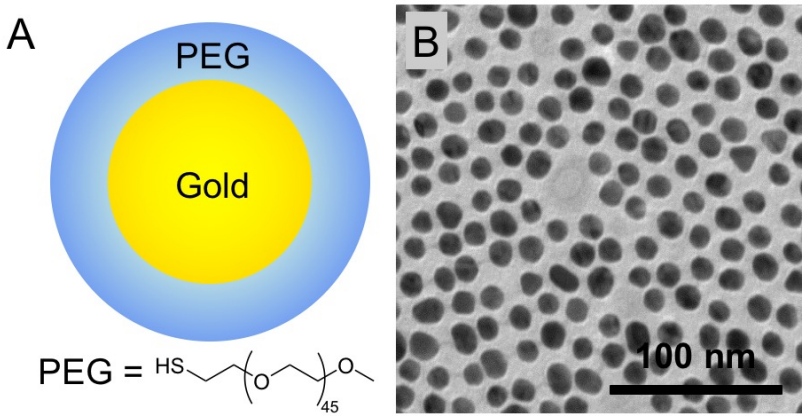


**Figure 1**. (A) Schematic representation of the AuNP. (B) Transmission electron micrograph of the AuNP.

SPCCT phantom imaging. We performed phantom imaging experiments to test the specific material discrimination capabilities of this SPCCT prototype. The images of the phantom provided by the SPCCT system are conventional CT images, water material decomposition images and gold images (Fig. 2B). As can be seen, the scanner could specifically detect and accurately quantify the range of concentrations of AuNP, with a very good linear correlation between the concentrations measured on the gold images and the concentrations prepared having a slope close to 1 (slope = 0.94, intercept = 0.17, $R^2$ = 0.99, RMSE = 0.18), and good agreement with a bias of 0.11 demonstrated by the Bland-Altman analysis (Fig. 2C-D). The PBS in the tubes is seen in the water images, as is the plastic of the phantom and the tubes, since it has a similar x-ray attenuation profile to water.

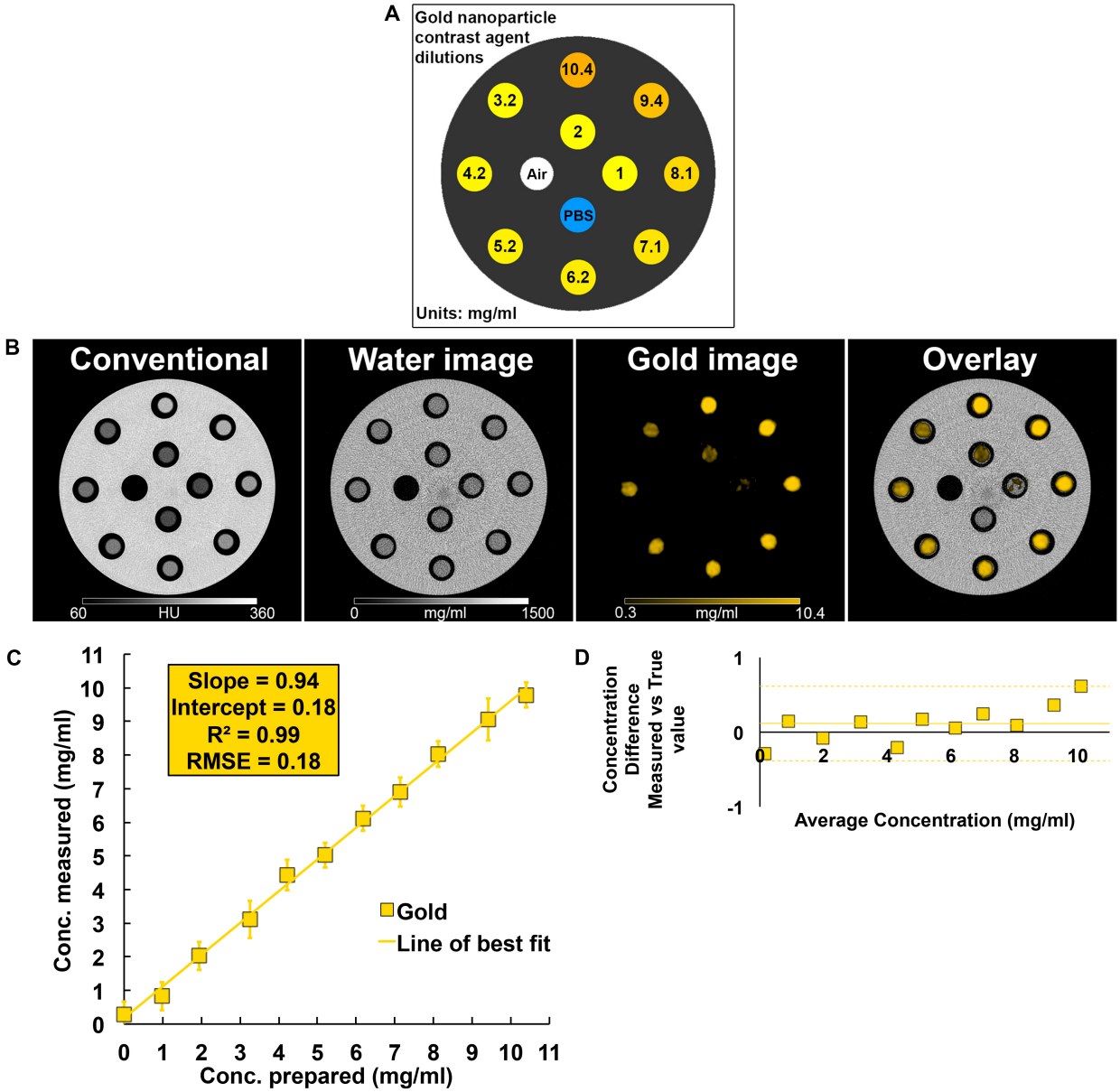


**Figure 2.** (A) Diagram of the phantom used. (B) SPCCT derived images (left to right: conventional CT image, water material decomposition, gold image, overlay of gold image on water image). (C) Comparison between the expected and measured concentrations. (D) Bland-Altman plot depicting the comparison of gold content between the prepared and measured concentration as determined by SPCCT image analysis.

*In vivo* SPCCT imaging. New Zealand White rabbits were injected with AuNP without any obvious side effects and scanned three times on the day of injection (once pre- (T0) and twice post-injection (T1, T2)). They were also scanned at one week (W1), one month (M1) and six months (M6) post-injection in order to determine and quantify the biodistribution of the contrast agent. The contrast agent was chosen because its K-edge is at 80.7 keV, relatively close to the effective energy of the x-ray spectrum used (30-120 keV). Furthermore, these

AuNP have long circulation times permitted by the hydrodynamic diameter of 18 nm and the thiol-PEG coating [9]. Last, there is widespread interest in the use of gold nanoparticles in an array of diagnostic and therapeutic applications [21–25].

The SPCCT system allowed us to perform repetitive imaging *in vivo* with 1-second acquisition times and provided conventional CT and quantitative gold images (Figs. 3-6). The gold images allowed specific detection of gold nanoparticles in the organs of interest and showed differential temporal uptake between organs (Figs. 3 & 6). For example, AuNP were highly concentrated in blood at 8 min post injection (4.76±0.51 mg/ml), but negligible values were found at one week and one month post-injection (0.16±0.42 mg/ml), matching the expected blood pool pharmacokinetics [9]. On the other hand, the gold content in the liver, spleen, and bone marrow, was lower at T1 and T2 (gold content at these time points is likely due to AuNP in the blood perfusing the organs) with persistent higher concentrations in scans acquired at 1 week, 1 month and 6 months (Figs. 3-6). At the last time point, the SPCCT system was used to perform a helical scan that covered the entire body of the animal (Fig. 5). This whole body scan revealed lymph nodes that contained gold with a concentration in the same range as the spleen. The liver, spleen and bone marrow are part of the mononuclear phagocyte system (MPS), and had sustained gold uptake and retention over time (Fig. 6). The gold content observed in the muscle and brain was close to zero at all time points, which is as expected since the nanoparticles are too large to extravasate in these organs. In the kidney and the urinary cavity, about 2 mg/ml of gold was detected at T1 and T2 without any signal at follow-up. A table with the gold concentrations in the organs, as determined from image analysis is presented in the supplementary information.

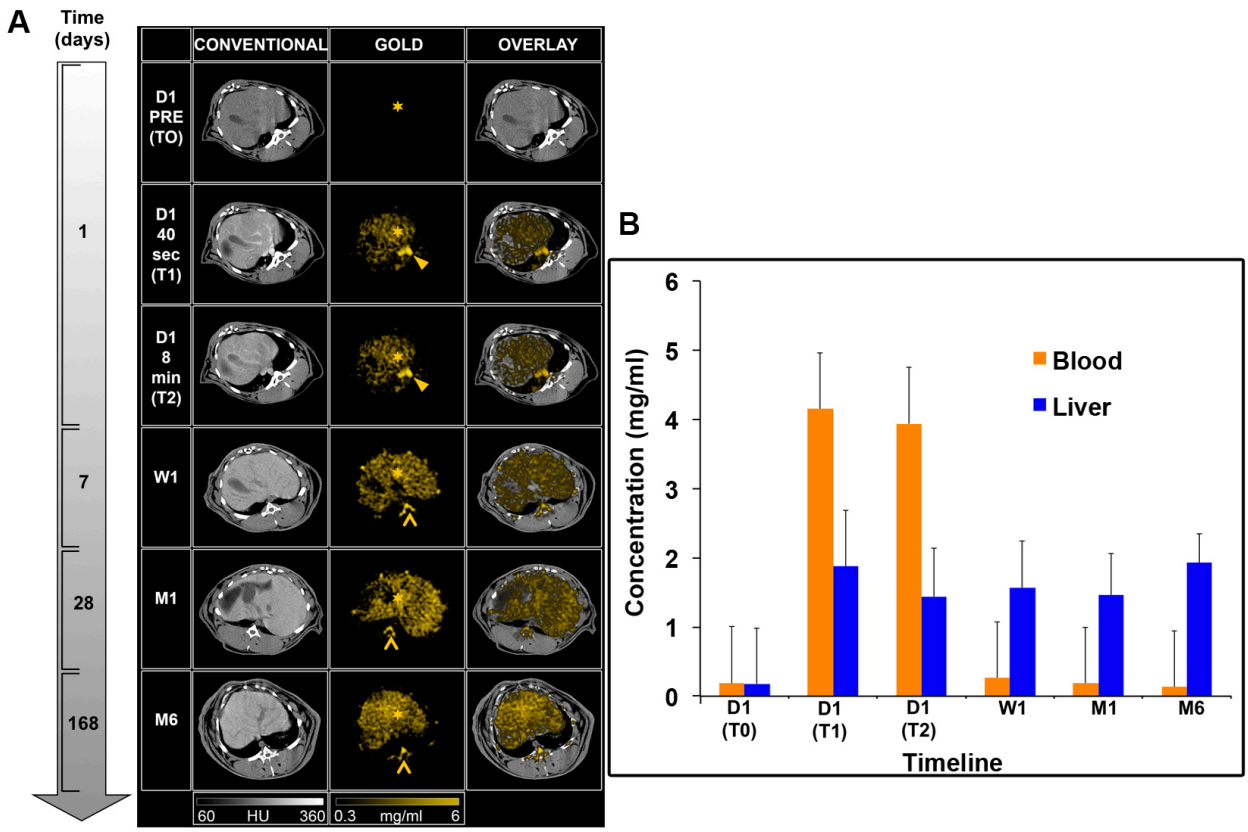


**Figure 3.** (A) SPCCT images displaying the AuNP biodistribution in the liver over time (left to right: conventional CT image, gold image, overlay). Star: liver, arrowhead: aorta, chevron: bone marrow. (B) Gold content in the liver and blood at various time points, as determined from SPCCT image analysis.

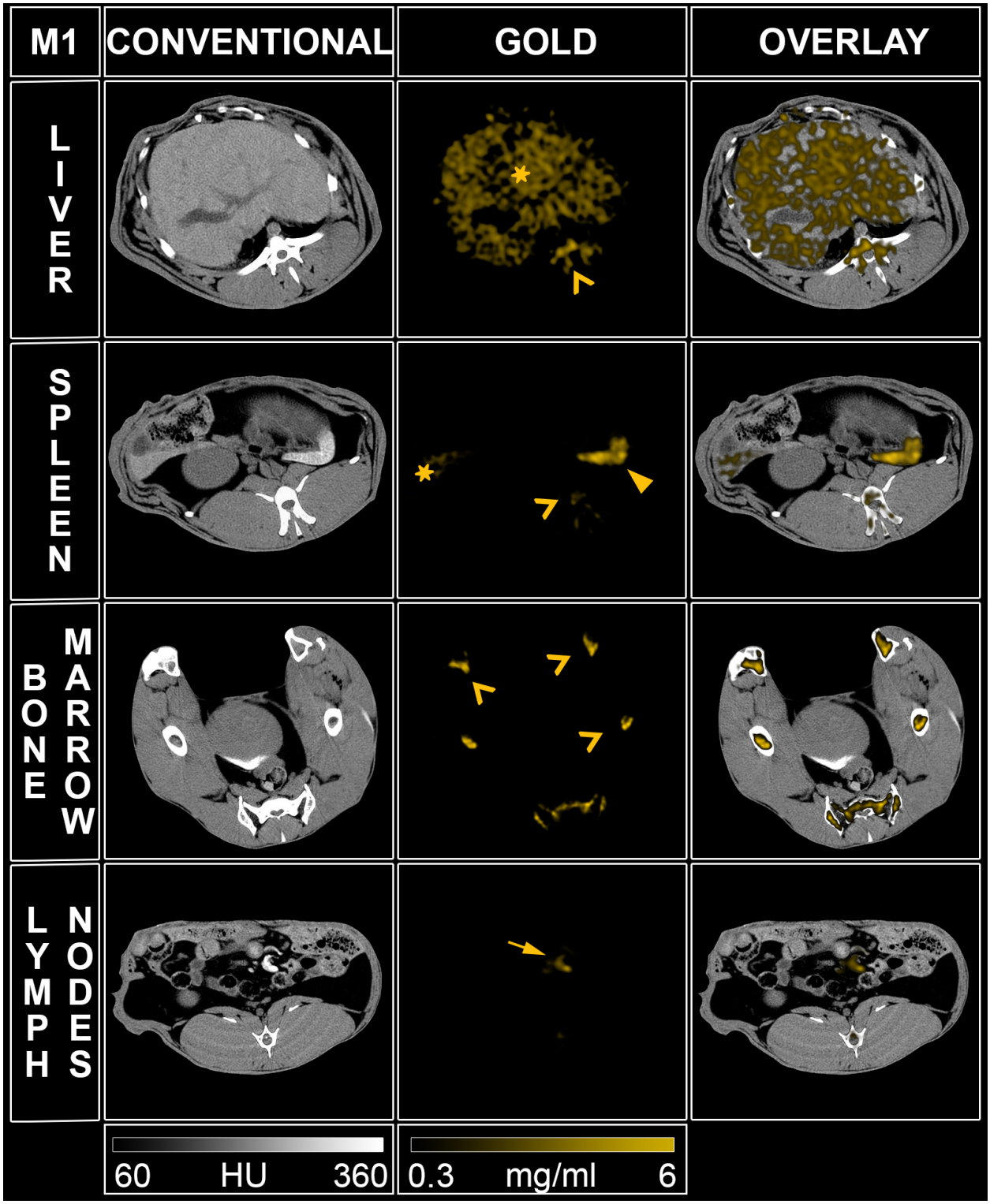


**Figure 4.** SPCCT images displaying the AuNP retention at one month (M1) in the organs of the mononuclear phagocyte system (left to right: conventional CT image, gold image, overlay). Star: liver, head arrow: spleen, chevron: bone marrow, full arrow: lymph node**.**

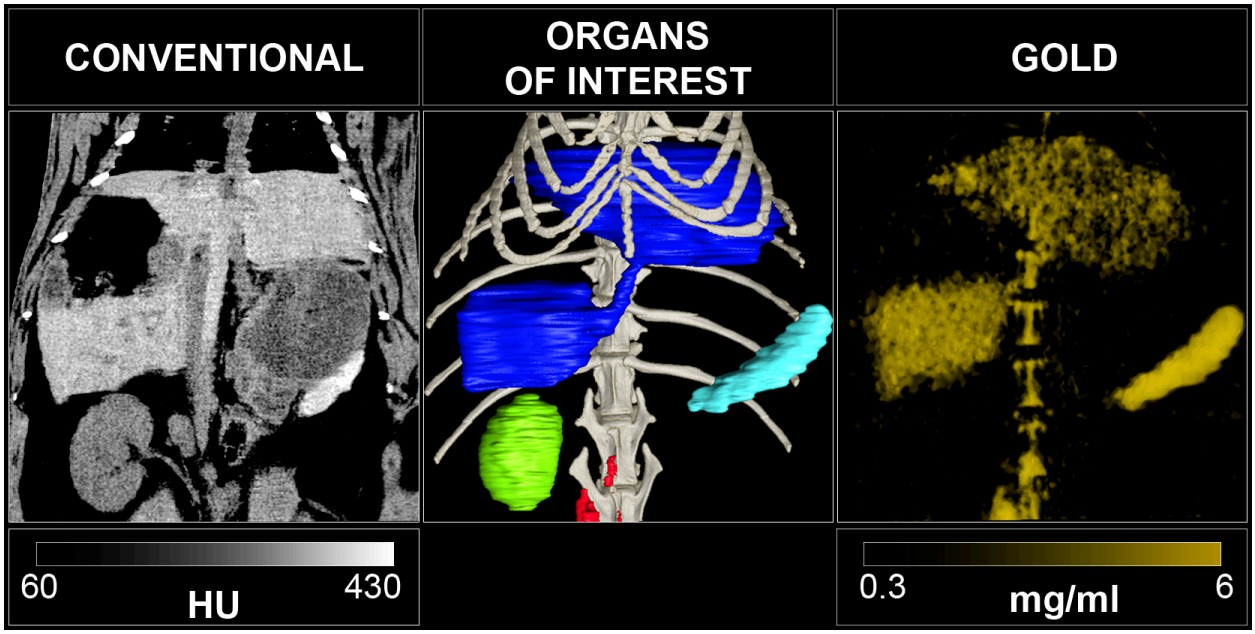


**Figure 5.** Left: Abdomen SPCCT images of a rabbit at 6 months after injection of gold nanoparticles with coronal conventional CT image, center: 3D volume rendering reconstruction of the conventional HU images with segmentation of the organs of interest (dark blue: liver, light blue: spleen, green: right kidney, red: lymph nodes, light grey: bone structure), right: 3D volume rendering reconstruction of the gold images.

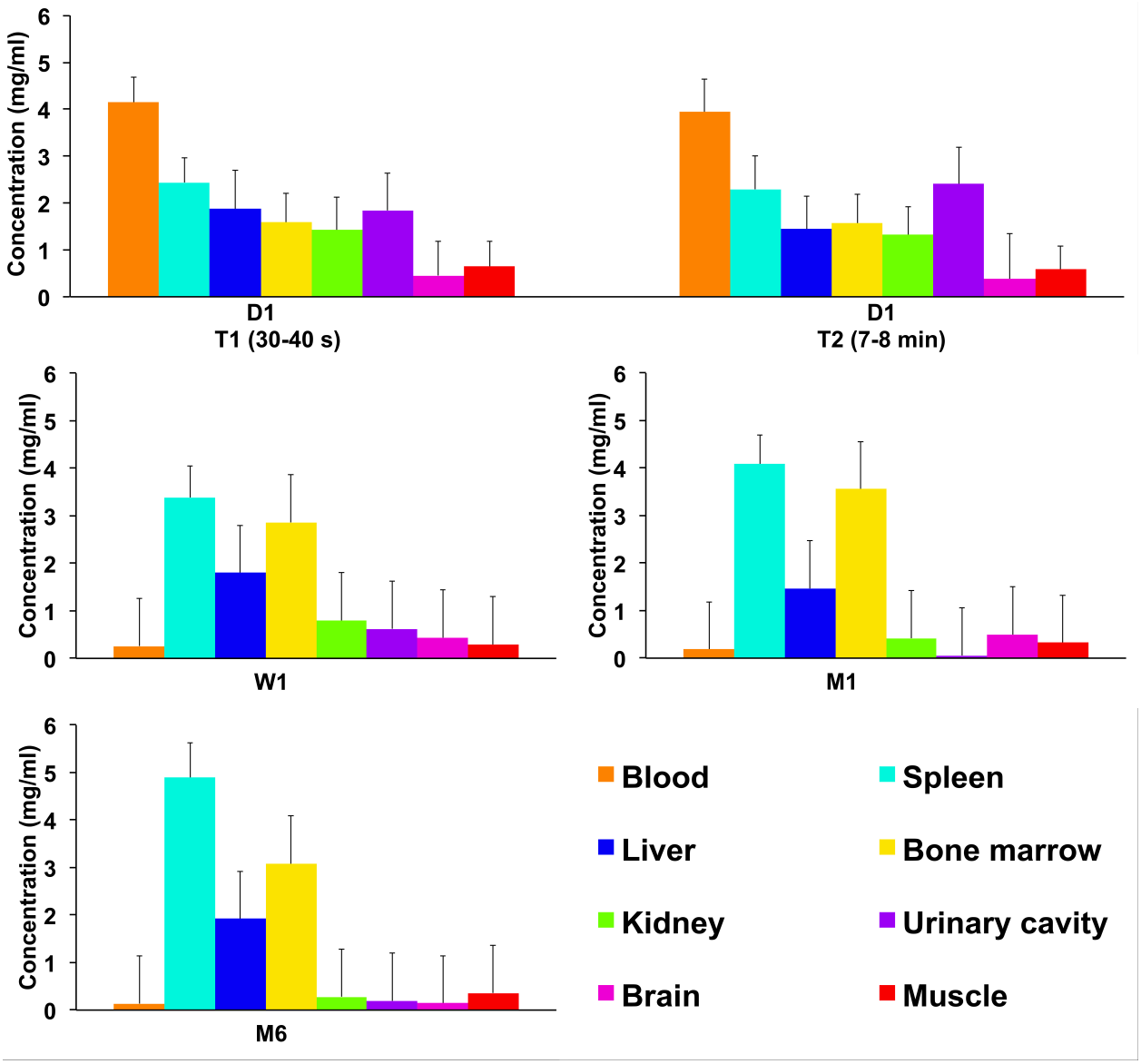


**Figure 6.** The biodistribution of AuNP among the organs of interest at several time points. Error bars represent the mean of the noise in the ROIs.

***Ex vivo* analysis.** In order to determine whether the measurements acquired from the SPCCT system were accurate, we sacrificed the animals (2 animals at 6 months, 2 animals at 1 month, 1 animal at one week) and performed ICP-OES on the organs (n=25). Comparison between concentrations measured with SPCCT and ICP-OES showed a linear correlation between the two measurements ($R^2$ = 0.93, intercept = 0.47, RMSE = 0.77) (Fig. 7A), and agreement with a bias of 0.11 demonstrated by the Bland-Altman analysis (Fig. 7B). SPCCT underestimated the gold concentration in the organs by 23% on average with an offset of 0.47, compared to ICP-OES values, however, this indicates quite good accuracy (Fig. 7A). There was no significant difference with a paired-T test analysis ($p>0.05$). Moreover, the data indicates that the highest concentration of AuNP is in the spleen.

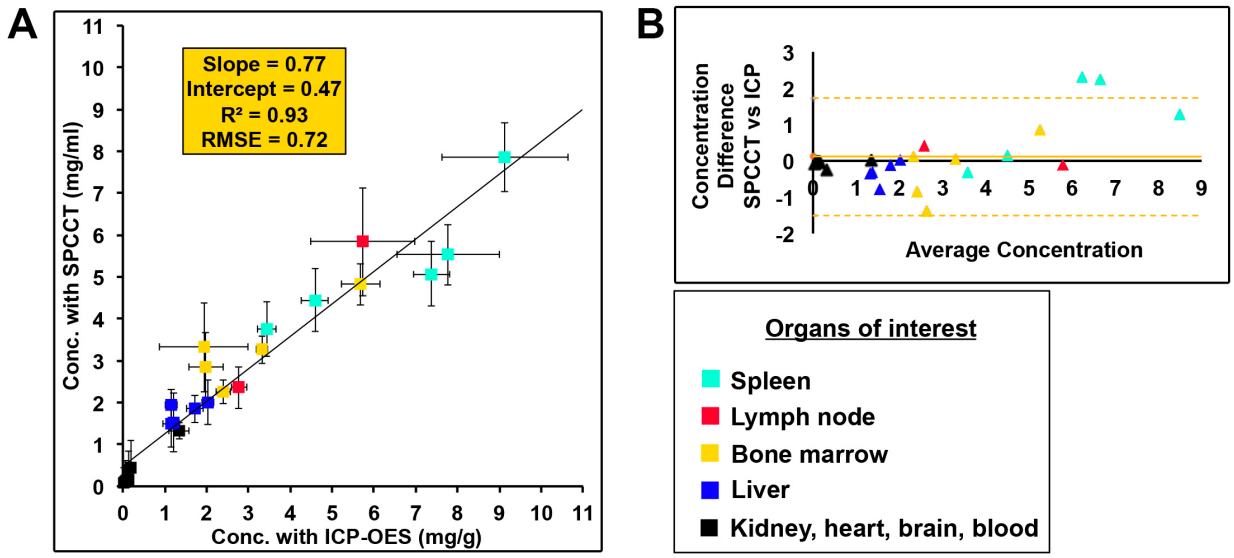


**Figure 7.** (A) Comparison between the expected and measured concentrations. (B) Bland-Altman plot depicting the comparison of gold content in rabbit organs as determined via ICP-OES and SPCCT image analysis.

Furthermore, to probe the localization of AuNP in organs, we performed TEM on tissues excised from the animals at the 6 month time point. We found the AuNP in these tissues to be intact and of similar size to those injected. We mostly observed AuNP aggregated inside lysosomes within macrophages in the organs of the MPS, i.e. liver, spleen, bone marrow and lymph nodes (Fig. 8A-L). AuNP were absent in cardiac and brain tissues (Fig. S1A-F). Moreover, surprisingly, we observed small amounts of AuNP in the renal mesangial cells behind the glomerular membrane (Fig. S1G-I).

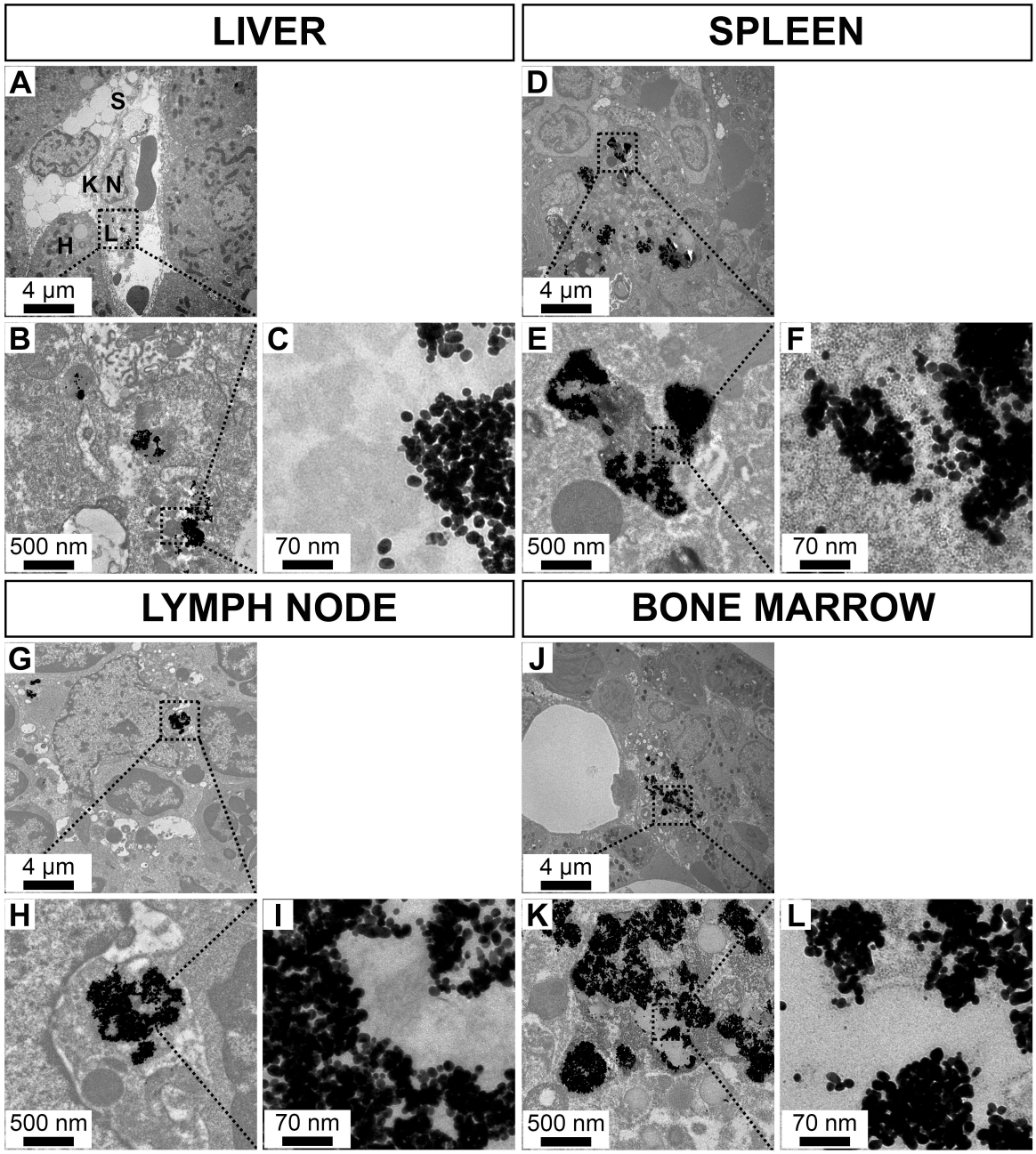


**Figure 8.** Transmission electron micrographs of rabbit organs from the mononuclear phagocyte system 6 months after AuNP injection over a range of magnifications. **A-C:** liver, **D-F:** spleen, **G-I:** lymph node, **J-L:** bone marrow (H: hepatocyte, K: Kuppfer cell, L: lysosome, N: nucleus, S: sinusoid).

## DISCUSSION

In this study, we demonstrated that a small FOV spectral photon-counting computed tomography prototype system derived from a modified clinical CT system enables repeated, noninvasive quantitative biodistribution analysis of AuNP *in vivo* with good accuracy compared to ICP-OES. We also demonstrated the capability of the SPCCT system to detect and quantify AuNP that accumulated in the MPS.

In SPCCT, the transmitted spectrum is collected by photon-counting detectors that have the ability to respond individually to every single photon received and discriminate their energy [26,27]. The photons are divided into multiple different energy windows, referred to as bins, for which one or more boundaries can be adjusted to match the K-edge of the contrast agent studied, the K-edge being the binding energy of the K shell electron of an atom [3,28–30]. The limitation of previous SPCCT systems was their lengthy scan times, which were as much as 24 hours for whole body imaging of a mouse[31]. This was due to the low photon flux needed to avoid pulse pileup in the detectors and limited number of detector rows. The small FOV SPCCT prototype scanner used for this study is equipped with detectors that have high flux capacity allowing high temporal resolution (1-1.5 seconds) compared to the previously reported prototypes [32], allowing for the dynamic and repetitive imaging *in vivo* reported herein [33].

Several advantages of using SPCCT for gold imaging have been highlighted in this study. First, the detection of AuNP in the bone marrow is remarkable, since contrast arising in that tissue would likely have gone unnoticed or be undetectable on conventional images due to the nearby presence of bone, although the accuracy of detection in the bone marrow is not as good as for other organs as can be seen in Figure 7, which may be due to factors such as beam hardening[34]. This highlights the strength of SPCCT, i.e. detection of contrast material close to calcified structures. Moreover, a good linear correlation in phantom imaging between SPCCT and prepared concentrations, and *in vivo* imaging between ICP-OES and SPCCT derived concentrations has been demonstrated, indicating that SPCCT is a non-invasive quantitative imaging technique [5,28,35]. This capacity is promising as a new tool for assessing non-invasively the biodistribution of materials that have a K-edge between ~40-100 keV, as opposed to ICP-OES based approaches, in which multiple groups of animals have to be sacrificed in a serial fashion and their organs dissected to obtain the biodistribution of contrast media at different time points. In addition, K-edge images benefit from the high spatial resolution provided by the photon-counting detectors as well as for the conventional

CT images [26]. Finally, the added value provided by the multi bin photon-counting data is to provide both anatomical information from conventional CT images and specific information from material decomposition images simultaneously, allowing tracking of a targeted heavy element for functional information. Some of the competing techniques requiring two scans to be acquired can suffer from motion between the acquisitions and therefore image registration issues [36], and expose the subject to higher radiation dose.

Gold nanoparticles are being explored in many applications in the biomedical field such as contrast agents for medical imaging [11,14], drug delivery, targeted killing of cells [21] and also therapeutic applications, such as theranostic agents [37] and radiosensitization[38]. This has led to numerous investigations of their toxicity and biodistribution. Previously, Naha *et al*. [12] have shown good cytocompatibility in vitro for this AuNP, with no effect on cell cytoskeleton or cell spreading.

*In vivo*, we confirmed the blood pool effect of the AuNP with scant change in blood concentration between scans acquired immediately after injection and acquired at 8 minutes post injection. Indeed, the gold nanoparticles are designed for long lasting vascular phase CT imaging, and are referred to as a blood pool contrast agent. They are designed to be biocompatible without toxicity at very high concentrations, as Cai et al. showed in mice [9], due to the PEG coating that increases its circulation half-life and reduces interactions with serum proteins. As they are 18 nm in diameter, theoretically no renal excretion was expected [39]. While, some gold signal was observed in the renal pelvis, ICP and UV/vis analysis of the urine did not indicate the presence of and AuNP. Therefore the signal in the renal pelvis is likely due to AuNP in the blood in this tissue.

Retention of AuNP over time was demonstrated in organs of MPS, e.g. the bone marrow, the liver, and the spleen, confirmed by the TEM of these tissues, which revealed retention in the macrophages. These findings supported the results of Naha *et al.* [12] that typically observed macrophages to be more sensitive to AuNP as compared to epithelial and fibroblast cells, likely due to their higher phagocytic activity and thus higher uptake of nanoparticles. Thus we corroborated the results of Cai *et al.* [9] who demonstrated that AuNP are taken up by the MPS organs.

Moreover, retention of AuNP at six months is consistent with the life span of tissue macrophages, which is several months or years, as well as the data of others [9,40]. Finally, we noticed retention in the mesenteric lymph nodes via hyper-intensities that appeared in the gold images, but would likely not have been noticed on conventional CT images. In summary, our study of biodistribution kinetics of these Au-NP demonstrated a biphasic

clearance of the nanoparticles, i.e. a steady state of the agent in the blood compartment after injection and a subsequent slow clearance of the dose into the organs of the MPS, indicating poor biological elimination leading to potential concerns over long-term safety, although Hainfeld *et al.* did not find any evidence of toxicity in mice over one year [41].

These findings emphasize the potential of SPCCT for mapping specific tissues due to their uptake of a contrast agent within clinically significant range of sensitivity and detection threshold (1 mg/ml), similar to previous publications using dual energy CT [13] and spectral CT [42]. This capability should be used for diagnosing pathologic conditions with a differing uptake of the contrast agent. Indeed, this diagnostic approach is known and has already been used clinically, i.e. for localization of the sentinel lymph nodes in breast cancer with MRI via the use of an iron oxide nanoparticle that is not taken up by pathologic lymph nodes [43] or imaging of the biliary tract via the use of an MRI-specific gadolinium contrast agent that is not excreted in cases of biliary cancer [44]. Compared with other techniques such as MRI or nuclear imaging, the strengths of SPCCT for this type of application would be its high temporal and spatial resolution, as well as whole-body imaging capabilities. Moreover, SPCCT, as a pragmatic non-invasive tool for determining quantitative biodistribution *in vivo* over time, may be advantageous for use in the developing field of nanotechnology, which frequently uses heavy elements such as gold, bismuth, ytterbium, tantalum [8,27,45–47].

Quantification of gold using ICP-OES was only performed at late time points. At these time points, significant quantities of gold were only found in the MPS organs, therefore the accuracy of the system was not tested in blood, muscle, brain. However, physics suggests that the system should be accurate for those tissues as well. We only compared ICP-OES to SPCCT for a limited number of animals, i.e. n=5, although the total number of organs compared was 25. The scanner used currently has small field of view and z-coverage, limiting its ability to perform rapid, whole body imaging. Only five animals were used for the in vivo imaging, limiting statistical power. In addition, we did not study human subjects, for whom results may vary compared to this relatively small animal model, as the X-ray attenuation of humans will be greater. Finally, we have only studied gold based agents in this report, while agents based on bismuth, tantalum, ytterbium and other elements have been reported as CT contrast agents and for other applications [10,47–51].

## Conclusions

In summary, we have demonstrated the potential of the newly developed small FOV SPCCT prototype imaging system for non-invasive quantitative determination of gold nanoparticle biodistribution *in vivo* over time, giving us confidence about the impact of SPCCT on nanoparticle development. Moreover, we have shown that the AuNP used in this study are effective contrast agents for the vascular system initially and for the MPS over time, providing potential applications in the field of cardiovascular disease and cancer.

## METHODS

*SPCCT system.*

The SPCCT scanner (Philips Healthcare, Haifa, Israel) is a modified clinical base prototype that has a small field-of-view (FOV) of 168 mm in-plane and with 2 mm z coverage, equipped with a conventional X-ray tube. Energies below 30 keV are filtered by pre-patient collimation and not transmitted, such as with a conventional clinical CT system. The photon-counting detectors are energy-sensitive detectors that have 5 rate counters with 5 different configurable energy thresholds[52]. For this study, the energy bins were set to 30–53, 53-78, 78–83, 83–98, 98-120 keV in order to benefit from high differential sensitivity to materials with differing atomic numbers, and in particular from the K-edge absorption of gold (80.7 keV). A full description of the SPCCT system can be found elsewhere . Axial acquisitions were performed at 100 mA and 120 kVp with a gantry rotation time of 1 s and 2400 projections per rotation for the phantom and animal experiments. One additional helical acquisition was performed at the last time point to visualize whole body nanoparticle uptake .

*SPCCT images.*

Multi-bin photon-counting data were pre-processed and a conventional CT image was derived from the information contained in all energy bins using a proprietary algorithm, corresponding to sum counts prior to reconstruction. After pile-up correction, material decomposition images were derived from the multi-bin photon-counting data and included a maximum-likelihood based material decomposition of the attenuation into water, iodine and gold material bases [3,33]. The iodine images were formed as part of the standard reconstruction protocol, but were not analyzed as no iodine contrast agent injection was done. The resulting gold and water images are displayed in units mg/ml. Note that the gold images are K-edge images since they are formed from information derived from bins placed around the K-edge

of gold. Images were reconstructed on a voxel grid of 0.25x0.25x0.25 $mm^3$ using conventional filtered back-projection without further post-processing besides removal of ring artifacts and utilization of a 2 pixel sigma Gaussian filter. For the analysis, the gold and water images were averaged to a slice thickness of 2 mm. For the representation of the organs of interest in the Figure 7, segmentation was done on the conventional images, while bone delineation was performed using windowing thresholds. No segmentation for the gold images was performed because of the specificity of the gold signal based on the gold images.

*Gold nanoparticles preparation and characterization.*

Gold nanoparticles were synthesized, based on previously reported methods [12,53]. The cores were formed by reducing gold chloride via addition of sodium citrate while at boiling point. Methoxy-PEG-2000-thiol was used to coat the resulting gold nanoparticles. The nanoparticles were washed three times with phosphate-buffered saline (PBS), concentrated and sterilized via syringe filtration. Samples of the final product were characterized with transmission electron microscopy (TEM) using a JEOL 1010 microscope, dynamic light scattering (DLS) using a Malvern Instruments Nano ZS 90 and inductively coupled plasma-optical emission spectroscopy (ICP-OES) using a Spectro Genesis system. The dynamic viscosity and the pH were also evaluated and compared to an iodinated contrast agent, iopamidol (65 mg/ml), and PBS. Viscosity was measured using a RFS3 rheometer from TA Instruments (New Castle DE). A pH meter was used.

*Phantom imaging.*

In order to validate the quantification of gold using K-edge information, a cylindrical phantom of 15 cm diameter and made of acetal homopolymer was used. Ten 1.5 ml polypropylene centrifuge tubes, 1 cm in diameter, were filled with AuNP samples ranging in concentration from 1 to 10.4 mg/ml, diluted with PBS, and one was only filled with PBS. The design of the phantom is schematically depicted in Fig. 2A.

*Animal experiments.*

Experiments were conducted with approval from the Institutional Animal Care and Use Committee (Council Directive No. 2010/63/UE on the protection of animals used for scientific purpose) under authorization number APAFIS#1732-2015091411181645v3. Five New Zealand white rabbits (Charles River, Canada, mean weight, 3.1 ± 0.5 kg; 2 females, 3 males; mean age, 7.4 ± 2.7 months) were anesthetized with 0.25 mg/kg intramuscular

injection of médétomidine (1.0 mg/ml, Orion Pharma, Orion Corporation, Espoo, Finland) and 20 mg/kg intramuscular injection of ketamine (10.0 mg/ml, Merial, Lyon, France). 22-gauge auricular vein catheters were placed. A veterinary handheld pulse oximeter and carbon dioxide detector (Model 9847V, Nonin Medical, Inc, Plymouth, Minnesota) with a remote sensor pulse placed on earlobe was used to monitor heart beat and oxygen saturation. Rabbits are the smallest animal model whose blood vessels are practical to image with a clinical scanner and have the benefit that the doses of contrast agent that need to be synthesized are relatively low compared with a larger animal model such as a pig.

3.5 ml/kg (about 12 ml) of gold nanoparticles were injected through the catheter placed in the auricular vein at 1 ml/sec. After the last imaging session, animals were euthanized using a lethal dose of Dolethal (Vetoquinol, Kontichsesteenweg, Aartselaar, Belgium). Specific organs were removed and prepared for gold content analysis using ICP-OES for comparison with SPCCT-based quantification of gold.

Images were acquired on the day of injection (D1), one week (W1), one month (M1) and six months later (M6). Imaging was performed at three time points on the day of injection, i.e. before injection (T0), 30-45 seconds (T1) and 7-8 minutes (T2) after injection of AuNP, with images acquired at the level of the heart, liver, spleen, kidney, urinary cavity and brain. Images were acquired in the same organs at W1, M1 and M6 without additional injection of gold nanoparticles. A whole body scan was performed at the M6 time point. SPCCT images were acquired using the same scan parameters as used for the phantom scan.

*Image processing.*

Axially acquired conventional CT images, water and gold images were analyzed using ImageJ software [54]. The attenuation values in HU were recorded from one slice, and the concentrations of gold (mg/ml) were recorded from an average of eight adjacent slices measurements, by manually drawing regions of interest (ROIs) in all rabbits for the imaged organs: thoracic aorta, myocardium, liver, spleen, left kidney and/or right kidney, bladder, paravertebral muscle, adipose tissue, bone marrow and brain. All ROIs were manually traced in the organs of interest by a senior radiologist (SSM, 6 years of experience) on the conventional images prior to retrieval of the gold concentrations per organ to avoid operator bias and then automatically copied on the gold images.

*Inductively coupled plasma-optical emission spectrometry (ICP-OES).*

Ex vivo analysis of the biodistribution of the gold nanoparticle was done using ICP-OES (Spectro Genesis ICP) according a protocol published elsewhere [23]. The organs taken from the sacrificed animals were weighed, minced into small pieces and then 1 g portions were digested using 800 µl of concentrated nitric acid at 75 ºC for 16 hours. After digestion with nitric acid, 250 µl of concentrated hydrochloric acid was added to each sample and the samples were incubated at 37 ºC for 3 hours. After this incubation, the final volume of each sample was made to 3.5 ml with DI water. The gold content in each sample was analyzed using ICP-OES, reporting concentrations in mg/g. The SPCCT, since the images acquired were volumes, reported gold content as mg/ml.

*Transmission electron microscopy.*

Organs of interest (liver, spleen, bone marrow, kidney, brain) were harvested, cut into one millimeter cubes, prefixed in 2.5% glutaraldehyde and prepared for TEM analysis using a conventional method [55]. Sections were examined with a JEOL 1400JEM (Tokyo, Japan) transmission electron microscope equipped with an Orius 1000 camera and Digital Micrograph.

*Statistics.*

For phantom analysis, linear regression was used to assess correlation between the measured and the expected concentrations. For the *in vivo* study, linear regression and paired T-test were used to assess correlation and difference respectively between the measured concentrations by SPCCT and the concentration determined by the gold standard ICP-OES. Bland-Altman analysis was performed for both experiments.

## REFERENCES


1 C. H. McCollough, S. Leng, L. Yu and J. G. Fletcher, *Radiology*, 2015, **276**, 637–653.

2 E. Roessl, B. Brendel, K.-J. Engel, J.-P. Schlomka, A. Thran and R. Proksa, *IEEE Trans. Med. Imaging*, 2011, **30**, 1678–1690.

3 J. P. Schlomka, E. Roessl, R. Dorscheid, S. Dill, G. Martens, T. Istel, C. Bäumer, C. Herrmann, R. Steadman, G. Zeitler, A. Livne and R. Proksa, *Phys. Med. Biol.*, 2008, **53**, 4031–4047.

4 S. Si-Mohamed, D. Bar-Ness, M. Sigovan, D. P. Cormode, P. Coulon, E. Coche, A. Vlassenbroek, G. Normand, L. Boussel and P. Douek, *Nucl. Instrum. Methods Phys. Res. Sect. Accel. Spectrometers Detect. Assoc. Equip.*, DOI:10.1016/j.nima.2017.04.014.

5 A. de Vries, E. Roessl, E. Kneepkens, A. Thran, B. Brendel, G. Martens, R. Proska, K. Nicolay and H. Grüll, *Invest. Radiol.*, 2015, **50**, 297–304.

6 S. T. Cochran, *Curr. Allergy Asthma Rep.*, 2005, **5**, 28–31.

7 P. A. McCullough, A. Adam, C. R. Becker, C. Davidson, N. Lameire, F. Stacul, J. Tumlin and CIN Consensus Working Panel, *Am. J. Cardiol.*, 2006, **98**, 5K–13K.

8 D. P. Cormode, P. C. Naha and Z. A. Fayad, *Contrast Media Mol. Imaging*, 2014, **9**, 37–52.

9 Q.-Y. Cai, S. H. Kim, K. S. Choi, S. Y. Kim, S. J. Byun, K. W. Kim, S. H. Park, S. K. Juhng and K.-H. Yoon, *Invest. Radiol.*, 2007, **42**, 797–806.

10 A. Jakhmola, N. Anton and T. F. Vandamme, *Adv. Healthc. Mater.*, 2012, **1**, 413–431.

11 J. F. Hainfeld, D. N. Slatkin, T. M. Focella and H. M. Smilowitz, *Br. J. Radiol.*, 2006, **79**, 248–253.

12 P. C. Naha, P. Chhour and D. P. Cormode, *Toxicol. In Vitro*, 2015, **29**, 1445–1453.

13 W. E. Ghann, O. Aras, T. Fleiter and M.-C. Daniel, *Langmuir ACS J. Surf. Colloids*, 2012, **28**, 10398–10408.

14 M. W. Galper, M. T. Saung, V. Fuster, E. Roessl, A. Thran, R. Proksa, Z. A. Fayad and D. P. Cormode, *Invest. Radiol.*, 2012, **47**, 475–481.

15 D. P. Clark, K. Ghaghada, E. J. Moding, D. G. Kirsch and C. T. Badea, *Phys. Med. Biol.*, 2013, **58**, 1683–1704.

16 D. P. Cormode, P. C. Naha and Z. A. Fayad, *Contrast Media Mol. Imaging*, 2014, **9**, 37–52.

17 D. Pan, C. O. Schirra, S. A. Wickline and G. M. Lanza, *Contrast Media Mol. Imaging*, 2014, **9**, 13–25.

18 D. P. Cormode, E. Roessl, A. Thran, T. Skajaa, R. E. Gordon, J.-P. Schlomka, V. Fuster, E. A. Fisher, W. J. M. Mulder, R. Proksa and Z. A. Fayad, *Radiology*, 2010, **256**, 774–782.

19 A. S. Thakor, J. Jokerst, C. Zavaleta, T. F. Massoud and S. S. Gambhir, *Nano Lett.*, 2011, **11**, 4029–4036.

20 H. Lusic and M. W. Grinstaff, *Chem. Rev.*, DOI:10.1021/cr200358s.

21 K. Weintraub, *Nature*, 2013, **495**, S14–S16.

22 D. Kim, S. Park, J. H. Lee, Y. Y. Jeong and S. Jon, *J. Am. Chem. Soc.*, 2007, **129**, 7661–7665.

23 P. C. Naha, K. C. Lau, J. C. Hsu, M. Hajfathalian, S. Mian, P. Chhour, L. Uppuluri, E. S. McDonald, A. D. A. Maidment and D. P. Cormode, *Nanoscale*, 2016, **8**, 13740–13754.

24 W. Ngwa, R. Kumar, S. Sridhar, H. Korideck, P. Zygmanski, R. A. Cormack, R. Berbeco and G. M. Makrigiorgos, *Nanomed.*, 2014, **9**, 1063–1082.

25 R. Popovtzer, A. Agrawal, N. A. Kotov, A. Popovtzer, J. Balter, T. E. Carey and R. Kopelman, *Nano Lett.*, 2008, **8**, 4593–4596.

26 K. Taguchi and J. S. Iwanczyk, *Med. Phys.*, 2013, **40**, 100901.

27 C. O. Schirra, B. Brendel, M. A. Anastasio and E. Roessl, *Contrast Media Mol. Imaging*, 2014, **9**, 62–70.

28 E. Roessl, B. Brendel, K.-J. Engel, J.-P. Schlomka, A. Thran and R. Proksa, *IEEE Trans. Med. Imaging*, 2011, **30**, 1678–1690.

29 J. S. Iwanczyk, E. Nygård, O. Meirav, J. Arenson, W. C. Barber, N. E. Hartsough, N. Malakhov and J. C. Wessel, *IEEE Trans. Nucl. Sci.*, 2009, **56**, 535–542.

30 E. Roessl and R. Proksa, *Phys. Med. Biol.*, 2007, **52**, 4679.

31 D. P. Cormode, E. Roessl, A. Thran, T. Skajaa, R. E. Gordon, J.-P. Schlomka, V. Fuster, E. A. Fisher, W. J. M. Mulder, R. Proksa and Z. A. Fayad, *Radiology*, 2010, **256**, 774–782.

32 A. de Vries, E. Roessl, E. Kneepkens, A. Thran, B. Brendel, G. Martens, R. Proska, K. Nicolay and H. Grüll, *Invest. Radiol.*, 2015, **50**, 297–304.

33 Blevis IM, Altman A, Berman Y, et al. Introduction of Philips preclinical photon counting scanner and detector technology development. Presented at the IEEE Nuclear Science Symposium and Medical Imaging Conference, San Diego, Calif, October 31–November 7, 2015

34 T. L. McGinnity, O. Dominguez, T. E. Curtis, P. D. Nallathamby, A. J. Hoffman and R. K. Roeder, *Nanoscale*, 2016, **8**, 13627–13637.

35 J. P. Schlomka, E. Roessl, R. Dorscheid, S. Dill, G. Martens, T. Istel, C. Bäumer, C. Herrmann, R. Steadman, G. Zeitler, A. Livne and R. Proksa, *Phys. Med. Biol.*, 2008, **53**, 4031–4047.

36 R. Grosjean, B. Sauer, R. M. Guerra, M. Daudon, A. Blum, J. Felblinger and J. Hubert, *Am. J. Roentgenol.*, 2008, **190**, 720–728.

37 K. T. Butterworth, J. R. Nicol, M. Ghita, S. Rosa, P. Chaudhary, C. K. McGarry, H. O. McCarthy, G. Jimenez-Sanchez, R. Bazzi, S. Roux, O. Tillement, J. A. Coulter and K. M. Prise, *Nanomed.*, 2016, **11**, 2035–2047.

38 G. Laurent, C. Bernhard, S. Dufort, G. Jiménez Sánchez, R. Bazzi, F. Boschetti, M. Moreau, T. H. Vu, B. Collin, A. Oudot, N. Herath, H. Requardt, S. Laurent, L. Vander Elst, R. Muller, M. Dutreix, M. Meyer, F. Brunotte, P. Perriat, F. Lux, O. Tillement, G. Le Duc, F. Denat and S. Roux, *Nanoscale*, 2016, **8**, 12054–12065.

39 H. S. Choi, W. Liu, P. Misra, E. Tanaka, J. P. Zimmer, B. Itty Ipe, M. G. Bawendi and J. V. Frangioni, *Nat. Biotechnol.*, 2007, **25**, 1165–1170.

40 E. Sadauskas, G. Danscher, M. Stoltenberg, U. Vogel, A. Larsen and H. Wallin, *Nanomedicine Nanotechnol. Biol. Med.*, 2009, **5**, 162–169.

41 J. F. Hainfeld, D. N. Slatkin, T. M. Focella and H. M. Smilowitz, *Br. J. Radiol.*, 2006, **79**, 248–253.

42 D. P. Clark and C. T. Badea, *Phys. Med. Biol.*, 2014, **59**, 6445–6466.

43 J. J. Pouw, M. R. Grootendorst, R. Bezooijen, C. A. H. Klazen, W. I. De Bruin, J. M. Klaase, M. A. Hall-Craggs, M. Douek and B. Ten Haken, *Br. J. Radiol.*, 2015, **88**, 20150634.

44 M. K. Seale, O. A. Catalano, S. Saini, P. F. Hahn and D. V. Sahani, *Radiogr. Rev. Publ. Radiol. Soc. N. Am. Inc*, 2009, **29**, 1725–1748.

45 C. O. Schirra, A. Senpan, E. Roessl, A. Thran, A. J. Stacy, L. Wu, R. Proska and D. Pan, *J. Mater. Chem.*, 2012, **22**, 23071–23077.

46 D. Pan, E. Roessl, J.-P. Schlomka, S. D. Caruthers, A. Senpan, M. J. Scott, J. S. Allen, H. Zhang, G. Hu, P. J. Gaffney, E. T. Choi, V. Rasche, S. A. Wickline, R. Proksa and G. M. Lanza, *Angew. Chem. Int. Ed Engl.*, 2010, **49**, 9635–9639.

47 D. Pan, C. O. Schirra, A. Senpan, A. H. Schmieder, A. J. Stacy, E. Roessl, A. Thran, S. A. Wickline, R. Proska and G. M. Lanza, *ACS Nano*, 2012, **6**, 3364–3370.

48 P. F. FitzGerald, R. E. Colborn, P. M. Edic, J. W. Lambert, A. S. Torres, P. J. Bonitatibus and B. M. Yeh, *Radiology*, 2016, **278**, 723–733.

49 P. J. Bonitatibus, A. S. Torres, B. Kandapallil, B. D. Lee, G. D. Goddard, R. E. Colborn and M. E. Marino, *ACS Nano*, 2012, **6**, 6650–6658.

50 A. L. Brown, P. C. Naha, V. Benavides-Montes, H. I. Litt, A. M. Goforth and D. P. Cormode, *Chem. Mater. Publ. Am. Chem. Soc.*, 2014, **26**, 2266–2274.

51 S. Rathnayake, J. Mongan, A. S. Torres, R. Colborn, D.-W. Gao, B. M. Yeh and Y. Fu, *Contrast Media Mol. Imaging*, , DOI:10.1002/cmmi.1687.

52 R. Steadman, C. Herrmann and A. Livne, *Nucl. Instrum. Methods Phys. Res. Sect. Accel. Spectrometers Detect. Assoc. Equip.*, 2017, **862**, 18–24.

53 F. Blasi, B. L. Oliveira, T. A. Rietz, N. J. Rotile, H. Day, P. C. Naha, D. P. Cormode, D. Izquierdo-Garcia, C. Catana and P. Caravan, *J. Nucl. Med. Off. Publ. Soc. Nucl. Med.*, 2015, **56**, 1088–1093.

54 C. A. Schneider, W. S. Rasband and K. W. Eliceiri, *Nat. Methods*, 2012, **9**, 671–675.

55 D. Horak, M. Babic, P. Jendelová, V. Herynek, M. Trchová, Z. Pientka, E. Pollert, M. Hájek and E. Syková, *Bioconjug. Chem.*, 2007, **18**, 635–644.

# SUPPLEMENTAL RESULTS

| Organs | D1 | | | | W1 | | M1 | | M6 | |
|---|---|---|---|---|---|---|---|---|---|---|
| | T1 | | T2 | | | | | | | |
| | Mean (mg/ml) | S.D. (mg/ml) | Mean (mg/ml) | S.D. (mg/ml) | Mean (mg/ml) | S.D. (mg/ml) | Mean (mg/ml) | S.D. (mg/ml) | Mean (mg/ml) | S.D. (mg/ml) |
| **Blood** | 4.15 | 0.54 | 3.94 | 0.72 | 0.26 | 0.35 | 0.18 | 0.45 | 0.14 | 0.21 |
| **Spleen** | 2.44 | 0.53 | 2.29 | 0.71 | 3.39 | 0.66 | 4.08 | 0.62 | 4.89 | 0.74 |
| **Liver** | 1.88 | 0.81 | 1.44 | 0.70 | 1.57 | 0.67 | 1.47 | 0.60 | 1.93 | 0.43 |
| **Bone marrow** | 1.59 | 0.61 | 1.57 | 0.63 | 2.86 | 0.51 | 3.56 | 0.41 | 3.08 | 0.94 |
| **Kidney** | 1.42 | 0.70 | 1.32 | 0.60 | 0.72 | 0.66 | 0.42 | 0.70 | 0.28 | 0.35 |
| **Renal pelvis** | 1.84 | 0.80 | 2.41 | 0.78 | 0.62 | 0.57 | 0.06 | 0.97 | 0.19 | 0.21 |
| **Brain** | 0.45 | 0.73 | 0.38 | 0.96 | 0.44 | 0.46 | 0.50 | 0.48 | 0.14 | 0.48 |
| **Myocardium** | 3.21 | 0.87 | 1.22 | 0.43 | 0.38 | 0.56 | 0.29 | 0.49 | 0.29 | 0.49 |
| **Muscle** | 0.65 | 0.53 | 0.58 | 0.50 | 0.29 | 0.42 | 0.33 | 0.56 | 0.36 | 0.58 |
| **Lymph nodes** | | | | | 2.36§ | 0.50§ | 6.69§ | 0.79§ | 7.22§ | 0.49§ |

T1: the first acquisition after gold nanoparticles (AuNP) injection from 30 to 45 seconds. T2: the second acquisition after AuNP injection from 7 to 8 minutes. W1: acquisition at 1 week. M1: acquisition at 1 month. Pre-injection measurements (T0) are not presented in the table. S.D. are standard deviation of the noise in the regions of interest.

One imaging session was performed at the 1 week (W1), 1 month (M1) and 6 month (M6) time points.

§ Lymph nodes were observed in the scans at one week, one month and six months.

**Table.** AuNP content of several organs (expressed in Au concentration) at various timepoints, as determined from SPCCT image analysis.

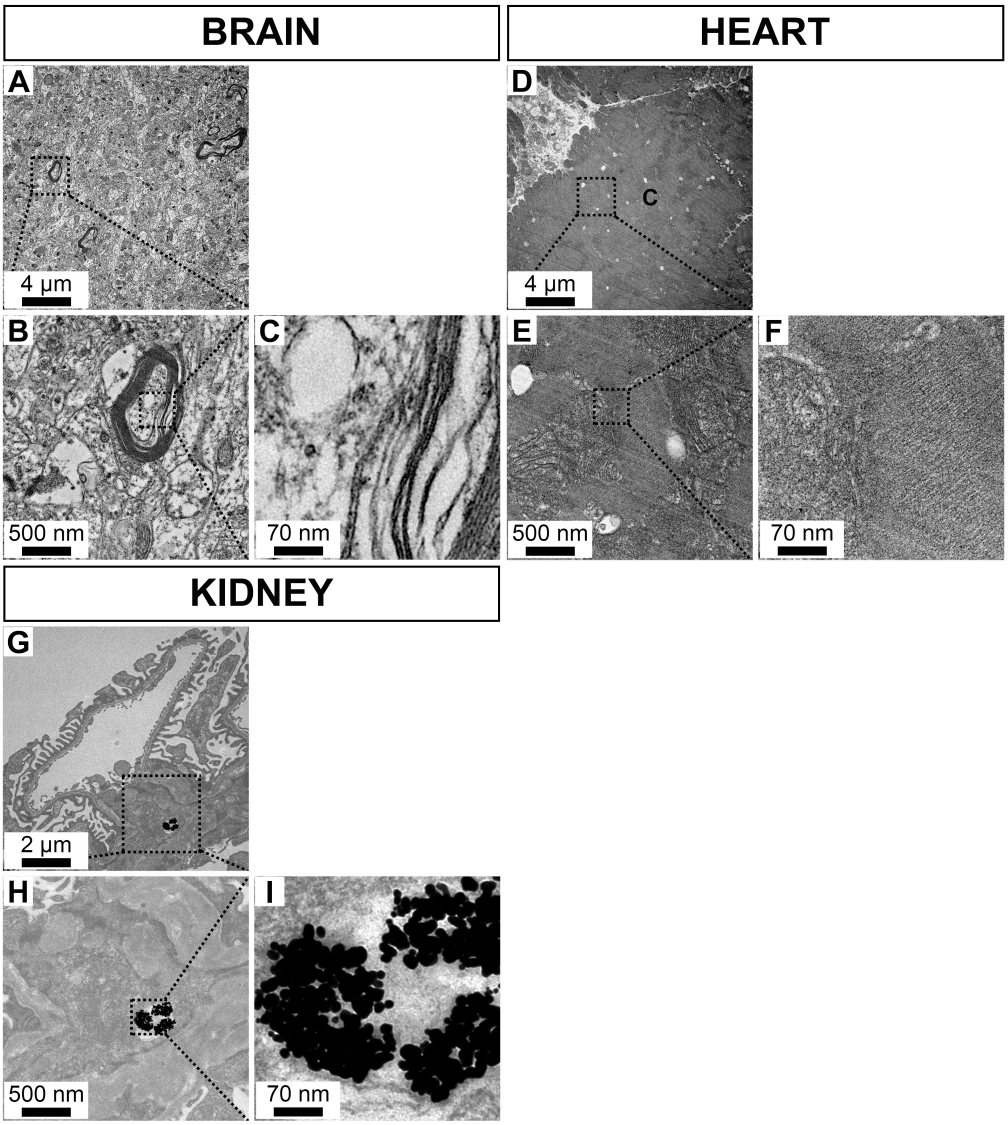


**Figure S1** Transmission electron micrographs of rabbit brain, heart and kidney 6 months after AuNP injection over a range of magnifications. **A-C:** heart (C: cardiomyocyte), **D-F:** brain, **G-I:** kidney.

## III. MOLECULAR MACROPHAGE K-EDGE IMAGING IN ATHEROSCLEROTIC RABBIT MODEL

**Title: *In vivo* molecular K-edge imaging of vulnerable atherosclerotic plaque using spectral photon-counting CT**

S. Si-Mohamed[1,2], M. Sigovan[1], J. C. Hsu[3], V. Tatard-Leitman[1], L. Chalabreysse[4], P. C. Naha[3], T. Garrivier[2], R. Dessouky[1,5], M. Carnaru[6], L. Boussel[1,2], D. P. Cormode[3], P. Douek*[1,2]

1 – Univ Lyon, INSA-Lyon, University Claude Bernard Lyon 1, UJM-Saint Etienne, CNRS, Inserm, CREATIS UMR 5220, U1206, F69621, Lyon, FRANCE
2 – Radiology Department, Hospices Civils de Lyon, Lyon, FRANCE
3 – Department of Radiology, Hospital of the University of Pennsylvania, Philadelphia, PA, USA
4 – Pathologist Department, Hospices Civils de Lyon, Lyon, FRANCE
5 – Radiology Department, Faculty of Medicine, Zagazig University, EGYPT
6 – Rheumatology Department, Allergy & Immunology, Yale University, New Haven, CT, USA

## ABSTRACT

**Background.** Macrophage burden is a large factor in the risk of atherosclerotic plaque rupture in coronary artery disease and its evaluation remains challenging with molecular noninvasive imaging approaches. Yet, spectral photon-counting CT (SPCCT) enabled K-edge imaging allows specific detection of macrophages using gold nanoparticles (AuNP).

**Objectives.** To perform K-edge imaging in combination with AuNP to detect and quantify the macrophage burden within the atherosclerotic aortas of rabbits.

**Methods.** 7 atherosclerotic and 4 control non-atherosclerotic New Zealand white rabbits were imaged before and at several time points up to two days after IV injection of 3.5 mL/kg AuNP (65 mg/mL). Additional angiography imaging was performed after IV injection of an iodinated contrast agent to prove the feasibility of atherosclerosis bicolor imaging. Gold K-edge and conventional CT images were reconstructed for qualitative and quantitative assessment of the macrophage burden. SPCCT imaging results were compared to histology, quantitative histomorphometry, transmission electron microscopy (TEM), quantitative inductively coupled plasma-optical emission spectrometry analyses (ICP-OES).

**Results.** In atherosclerotic rabbits, calcifications were observed along the aortic wall before injection. At two days after injection of AuNP, only gold K-edge images allowed distinction

of plaque enhancement within calcifications, as well as with the lumen enhancement during angiography. A good correlation was observed between the gold concentration measured within the wall and the macrophage area in 35 plaques (5 per rabbits)(r=0.82, 95% CI [0.67; 0.91], P=0.0001), which was opposite to that observed from conventional CT images (r=0.41, 95% CI [0.09; 0.65], P=0.01). TEM and ICP-OES analyses confirmed the gold K-edge imaging findings.

**Conclusions.** Our study represents a unique approach in the specific evaluation of macrophage burden in atherosclerotic plaque by using K-edge imaging in combination with AuNP, that allows to provide non-invasively both molecular and anatomic information *in vivo*.

## INTRODUCTION

Atherosclerosis is a leading cause of coronary artery disease (CAD) worldwide, with a high risk of myocardial infarction as the first major clinical manifestation (1). Noninvasive imaging of the macrophage burden, considered as an important determinant of atherosclerotic plaque vulnerability, can assist in diagnosing patients who are at high-risk of rupture (2,3). Among the modalities available, CT imaging is a method of choice for CAD, which produces high resolution images of coronary arteries in less than one second and is triggered on the heartbeat, thus mitigating the issues of motion (4). However, current CT technology presents several limitations for assessment of the inflammation in atherosclerotic lesions as well as for the lumen and would be greatly improved by: (1) better spatial resolution, (2) specific imaging capabilities to differentiate contrast media and wall calcifications, (3) specific contrast agent to target inflammatory processes in plaque. In order to address these challenges, a new CT technology called spectral photon-counting CT (SPCCT) technology has recently been developed in combination with appropriate contrats agents.

SPCCT is based on small pixel size photon-counting detectors enabling high spatial resolution imaging (5,6). Additionally, these detectors resolve the energy of each photon of the transmitted spectrum, quantify them, and classify them into energy bins. This process permits a configurable sampling of the energy-dependent attenuation of a subject, which allows discriminating the Compton and photoelectric effects that are specific for a given tissue or material (5). In the presence of one or more exogenous materials with high atomic numbers (i.e. 60 or higher), SPCCT enables K-edge imaging, which can produce specific and quantitative map of the distribution of an individual element. This is possible because the

system is capable of detecting the discontinuity of attenuation around the K-edge (5,7). Therefore, a K-edge agent that accumulates in macrophages could be extremely advantageous for K-edge imaging of vulnerable atherosclerotic plaques.

Among the candidate for K-edge imaging, promising results have been reported using gold nanoparticles (AuNP)(8,9). In addition, AuNP are highly biocompatible, extremely dense and have low viscosity, which is important for *in vivo* applications (10). Altogether, SPCCT has already given encouraging results in the field of cardiovascular imaging in phantoms, animals, and human studies (6,11–13) with several proof-of-concepts of K-edge imaging in phantom and animals experiments for monocolor (*i.e.* imaging of one agent) or bicolor imaging (*i.e.* simultaneous imaging of two agents)(8,14–17).

Therefore, we performed SPCCT enabled K-edge imaging in combination with AuNP to detect and quantify the macrophage burden within the atherosclerotic aortas of rabbits. K-edge imaging results were compared to conventional CT imaging, histology, transmission electron microscopy and quantitative inductively coupled plasma-optical emission spectrometry analyses.

## METHODS

*Animal model of atherosclerotic plaque*

All procedures were conducted with approval from the Institutional Animal Care and Use Committee (CELYNE committee, APAFIS#1732-2015091411181645). 11 male New Zealand white rabbits (Charles River, Canada) were used: 7 rabbits were fed a 1% cholesterol diet (SAFE DIETS, Augy, FRANCE) for 2 weeks before inducing a balloon injury of the aorta, as previously described (18,19). The same diet was followed for a further 6 weeks then substituted with a chow diet for 10 weeks (mean(SD) weight: 3.8(0.5) kg, age: 34.5 weeks). Four non-injured rabbits with matching weight and sex were fed a regular chow diet and used as non-atherosclerotic controls (mean(SD) weight: 3.4(0.2) kg; age: 18 weeks). These procedures promote atherosclerotic plaque development in the abdominal aorta, which is similar in size to human coronary arteries. Furthermore, a high level of macrophage infiltration and presence of calcification are expected due to the age of the animals at the time of imaging (18,19).

*K-edge SPCCT contrast agent*

PEG-coated AuNP with a mean hydrodynamic radius of 18 nm and a concentration at 65 mg Au/mL were synthesized as previously reported (20). Samples of the final product were characterized with transmission electron microscopy (TEM) using a JEOL 1010 microscope, dynamic light scattering (DLS) using a Malvern Instruments Nano ZS 90, inductively coupled plasma-optical emission spectroscopy (ICP-OES) using a Spectro Genesis system, and energy dispersion X-ray spectroscopy (EDS) using a FEI Quanta 600 FEG scanning electron microscope operated at 15 kV and equipped with EDX detectors.

*SPCCT imaging protocol*

Helical acquisitions of the whole rabbit aorta were performed using a SPCCT system (Philips Healthcare, Haifa, Israel) at 120 kVp, 100 mAs, with a pitch at 1 and a rotation time at 1 second. SPCCT was equipped with energy-sensitive photon-counting detectors of 2-mm-thick cadmium zinc telluride with a pixel pitch of 270 x 270 $\mu m^2$ at isocenter. The in-plane resolutions evaluated by the modulation transfer function measurements on a 100 µm tungsten wire at a distance of 15 mm to isocenter were 11.4 lp/cm (438 µm size) at 50% and 22.4 lp/cm (223 µm size) at 10% (14). Combination of (1) small focal spot (0.6 x 0.7 mm in size), (2) small FOV and high matrix size for small isotropic reconstructed voxel size at 250 µm(x) x 250 µm(y) x 250 µm(z) (160 mm FOV, 640 matrix, 250 µm slice thickness), and (3) an appropriate Kernel filter was used for conveying the intrinsic spatial resolution of the system in order to analyze healthy rabbit aortic wall thickness (between 200-300 µm)(21). With respect to K-edge imaging, the SPCCT system allows five energy bins set at 30–53, 53–78, 78–83, 83–98 and 98–120 keV for gold imaging only (monocolor imaging) and gold+iodine (bicolor imaging)(8,9). An *in vitro* imaging was first performed on tubes containing the K-edge contrast agent (AuNP), an iodinated contrast agent, and calcium phosphate. Then, an *in vivo* imaging was done at several time points before and after injection of 3.5 mL/kg of AuNP (65 mg Au/mL) at the following times: 5 minutes, 45 minutes, one day, and two days. Additional SPCCT angiography imaging of the abdominal aorta was performed at the end of protocol with 1 mL/kg IV injection of an iodinated vascular contrast agent (iomeron 400 mg/mL, Iomeprol; BRACCO, Milan, ITALY) at a speed of 2 mL/s to prove the feasibility of bicolor imaging in atherosclerosis. The design of the study is depicted in **Figure 1.**

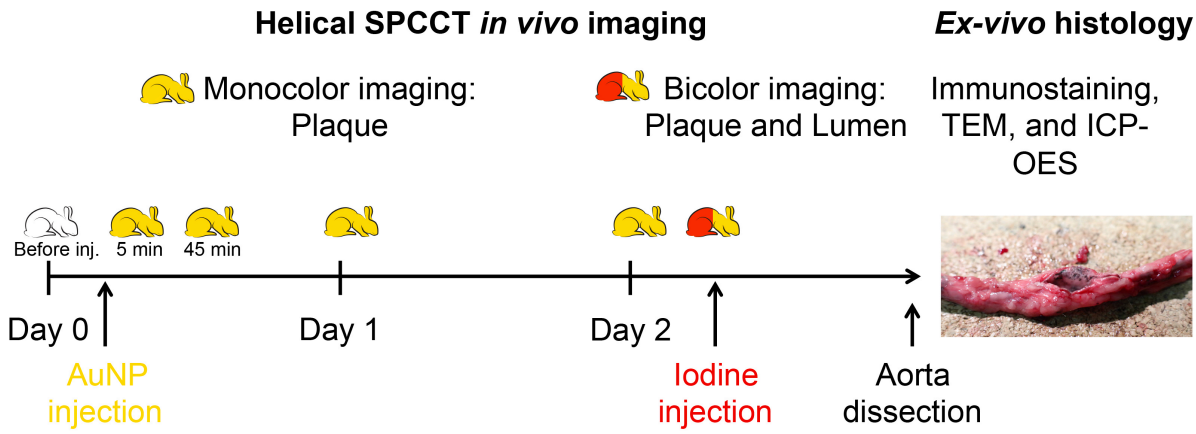


**Figure 1.** Study design schematic. (TEM: transmission electron microscopy, ICP-OES: inductively coupled plasma-optical emission spectrometry).

*SPCCT image reconstruction and analysis*

Conventional images scaled in HU and spectral images (gold K-edge, iodine, and water images) scaled in mg/mL were reconstructed from the same acquisition using the same reconstruction parameters (voxel size 250mm$^3$, standard Kernel). A descriptive qualitative analysis of the aortic wall in terms of presence of hyper-dense regions before and after injection was performed by two observers in consensus (__, __: both radiologists, 10-20 years of experience). For an analysis of the gold nanoparticle uptake within the aortic wall, we performed a semi-automatic quantitative analysis of the macrophage burden by measuring the attenuation on conventional images and the concentration of gold on gold K-edge images. Analysis was performed by segmenting semi-automatically a volume-of-interest of the whole aortic lumen using dedicated software (Amira, Thermo Fischer Scientific) and a dedicated graphic tablet (Wacom tablet, USA). The masks were then transferred to an in-house Matlab routine to compute a wall mask based on a predefined homogeneous thickness (2 pixels, 500 µm thickness). Furthermore, the total quantity of gold within the segmented wall was calculated based on the average gold concentration and the total volume of the mask. For an analysis of gold nanoparticle uptake within the immunostained aortic wall sections, we performed a quantitative analysis of 5 axial sections of 0.25 mm thickness spaced every 5 mm, starting from the first slice below the coeliac artery (7 rabbits, n sections=35), that corresponded to the sections analyzed in histology. The attenuations on conventional images and gold concentrations on gold K-edge images were measured by segmenting the wall using

the freehand selection tool in ImageJ on conventional images and transferring the ROI to the corresponding gold K-edge image (22).

*Ex vivo analyses*

*Histology*

The aorta from the thoracic to the iliac portions was excised carefully, with conservation of the main visceral branches in order to correlate SPCCT images with histology. The aorta samples were perfused with saline and fixed on cork with identification of the coeliac artery, providing an easy and reproducible landmark on imaging.

For all atherosclerotic rabbits, five sections of of 2 mm length each were collected from the coeliac artery (every 5 mm), stained with hematoxylin eosin safran and Masson's trichrome and immunostained with a monoclonal RAM-11 antibody (a marker of rabbit macrophage cytoplasm) counterstained with hematoxylin for macrophages. Staining of samples from control non-atherosclerotic rabbits was also performed. Atherosclerotic plaques were analyzed according to the AHA classification (23). Area of macrophages, defined as proportion (%) of wall infiltrated with macrophages was measured on immunostained sections. Five additional sections for 7 atherosclerotic rabbits and for 1 non-atherosclerotic rabbit were collected adjacent to each of the five sections described above, cut into one millimeter cubes, prefixed in 2.5% glutaraldehyde and prepared for TEM analysis (24)**.** Distribution of AuNP was analyzed on atherosclerotic and non-atherosclerotic tissue sections with TEM. Thoracic and abdominal aortic samples left after histology sampling were used for gold content analysis using ICP-OES.

*Histologic analysis*

Two observers (__: pathologist: 15 years of experience in atherosclerotic imaging, __: radiologist: 1 year of experience) rated in consensus the presence and the intensity of the following atherosclerotic plaque constituents: thickness, fibrosis (mild, intermediate, severe), smooth muscle cells, type of inflammatory cells (macrophages, lymphocytes cells), lipid core, calcification, hemorrhage and thrombus; in order to grade the plaque according to the AHA classification (23).

*Quantitative histomorphometry*

The acquisitions were performed with X5 lens and images were processed using the available plugin "Color Segmentation" in ImageJ v1.52s, as previously described (http://bigwww.epfl.ch/sage/soft/colorsegmentation/). Segmentation was performed using color thresholds adjusted manually to the immunostaining coloration of the macrophage area.

*Transmission electron microscopy (TEM) of tissue sections*

Sections were examined with a JEOL 1400JEM (Tokyo, Japan) transmission electron microscope equipped with an Orius 1000 camera and Digital Micrograph.

*Inductively coupled plasma-optical emission spectrometry (ICP-OES)*

Ex vivo analysis of the biodistribution of the gold nanoparticle was performed using ICP-OES (Spectro Genesis ICP) according a protocol published previously (24). The aorta samples were weighed and minced into pieces, and then 1 g portions were digested using 800 µl of concentrated nitric acid at 75 ºC for 16 hours. 250 µl of concentrated hydrochloric acid was then added to each sample before incubating at 37 ºC for 3 hours. After that, the final volume of each sample was made to 3.5 ml with distilled water. In order to compare the SPCCT and ICP-OES measurements, the gold content values were converted into the same units, i.e. mg. Weight and conversion of the mass to volume for ICP results were calculated using a d=1 g/mL conversion factor.

*Statistical analysis*

Data were expressed as mean(SD)(range) in Hounsfield units for conventional images, in mg/mL for gold K-edge images, and in mg for gold quantity measured by ICP and SPCCT.

To compare the aortic wall enhancement between time points before injection and two days after injection, a two-tailed paired t-test was performed in the atherosclerotic animal group (n=7) and the control group (n=4).

To assess the correlation between macrophage area measured in immunostained sections and both the concentration of gold and the attenuation measured in the corresponding SPCCT sections (n=35), a two-tailed Pearson correlation coefficient was calculated.

The nominal level of significance for all tests was $P<0.05$. GraphPad Prism 7.0a (GraphPad Software Inc., San Diego, CA) was used for statistical analysis.

A more detailed description of the methods is reported in the **Supplemental material**.

## RESULTS

An illustration of molecular K-edge imaging approach in combination with AuNP in calcified atherosclerotic plaque is provided in **Figure 2**.

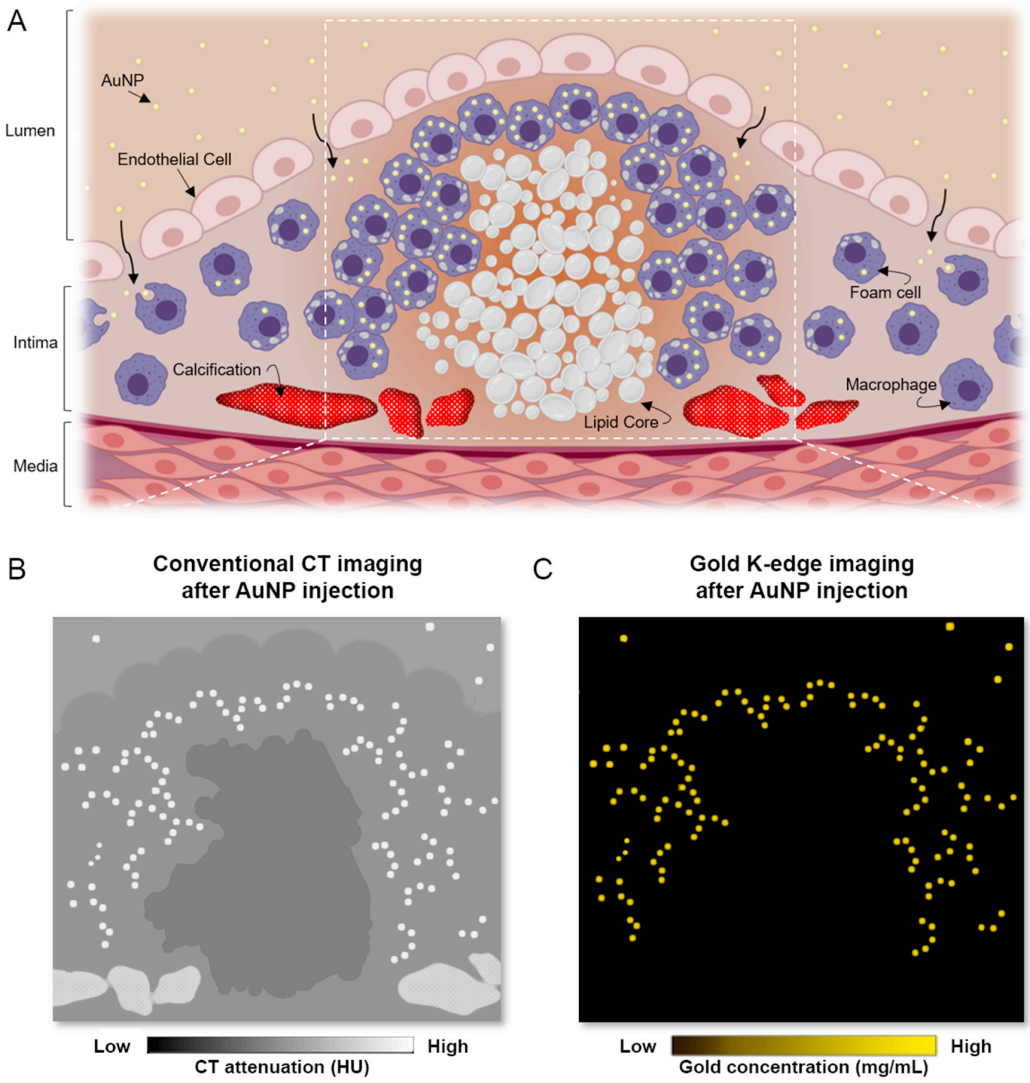


**Figure 2. Understanding of the molecular K-edge imaging approach using spectral photon-counting CT *in vivo* for macrophage detection and quantification in calcified atherosclerotic plaque in combination with a K-edge contrast agent, the Gold nanoparticles (AuNp).**

(A) Schematic of uptake of PEG-coated AuNP by macrophages within an atherosclerotic plaque. (B) Schematic of conventional CT showing different high density materials (AuNP, calcifications), hampering the characterization and quantification of macrophage burden. (C) Schematic of SPCCT gold K-edge imaging for specific, non-invasive macrophage burden imaging, which permits the quantification of AuNP.

*In vitro characterization and imaging of the PEG-coated AuNP*

The AuNP used had a core size of 12.5 nm, as found from TEM and mean hydrodynamic diameter of 18 nm as determined by dynamic light scattering. Energy dispersive x-ray spectroscopy resulted in strong peaks at 2.12, 9.66, and 11.50 keV that are characteristic of gold atoms (copper and other peaks are background arising from the grid used). In vitro, K-

edge imaging depicted only the AuNp tube, with no background or signal from the iodine and calcium tubes, confirming capacity to detect specifically AuNP (**Figure 3**).

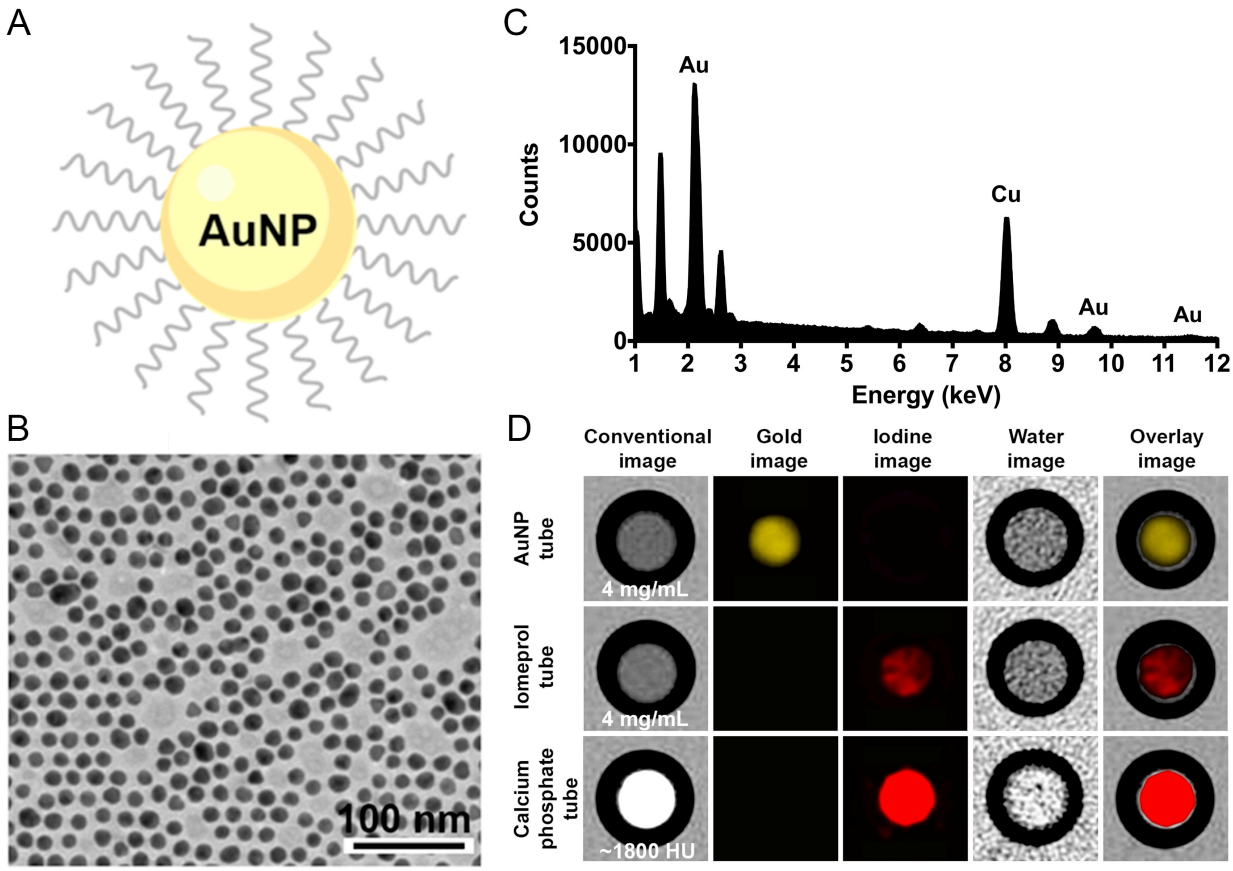


**Figure 3. *In vitro* characterization and imaging of PEG-coated AuNP.**
(A) Schematic representation of a PEG-coated AuNP. (B) Transmission electron micrograph of the AuNP. (C) The characteristic absorption spectrum of gold was detected with energy dispersive X-ray spectroscopy. (D) *In vitro* SPCCT imaging of tubes containing AuNP, iomeprol, or calcium phosphate.

*Macrophage burden visualization by gold K-edge imaging in vivo*

Before AuNP injection, sections presenting focal hyper attenuation on conventional images were observed along the aortic wall in all atherosclerotic animals. The location and extent of these sections was variable between the animals, but they were more predominant within the abdominal aorta, where the diameter was smaller. These sections were indicative of calcifications (**Figure 4**). No hyper attenuation was observed along the aortic wall in non-atherosclerotic animals (**Supplemental Figure 1**).

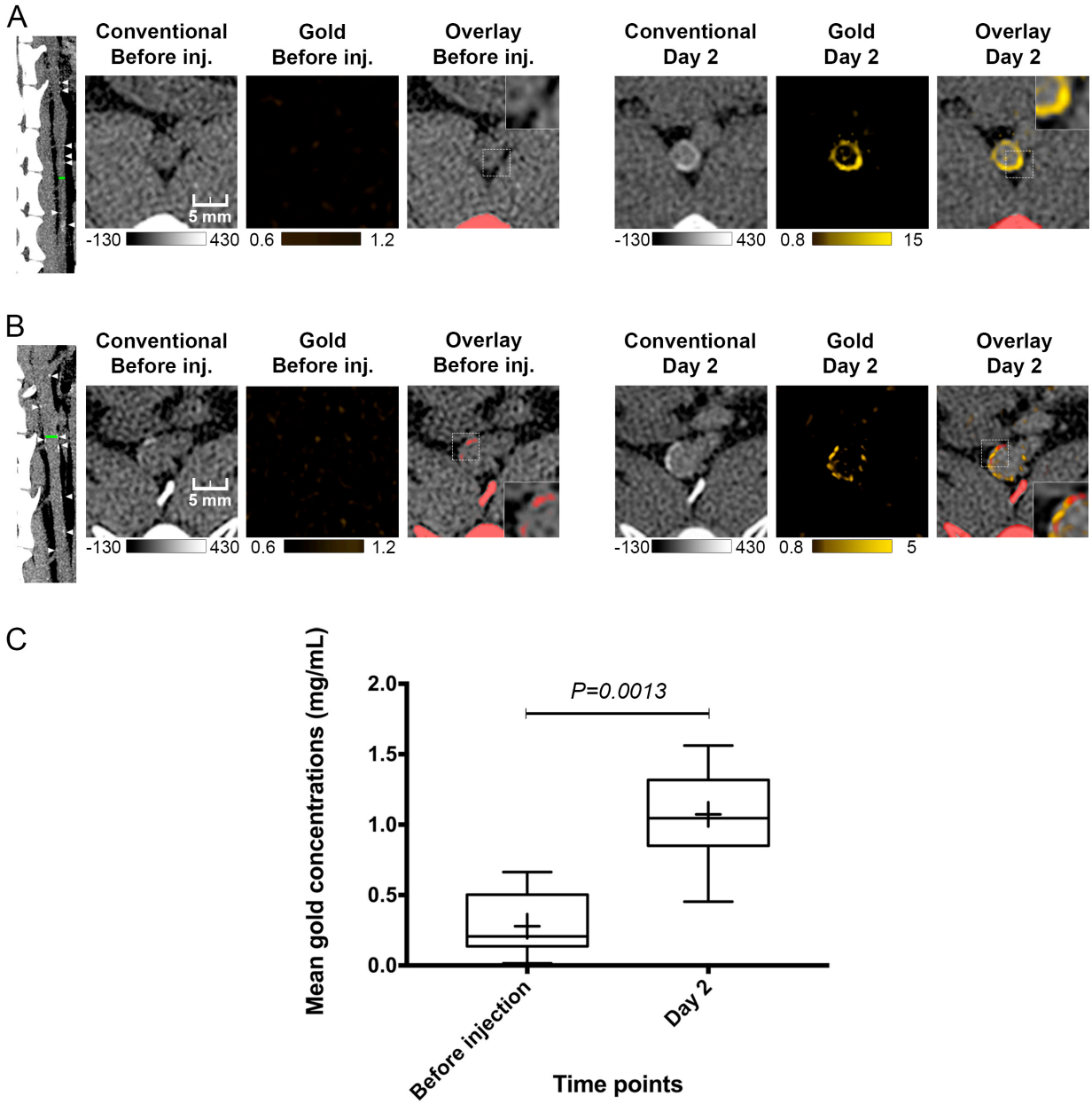


**Figure 4. Monocolor SPCCT imaging of atherosclerotic rabbit aortas before and two days after injection of AuNP.**

(A) Non calcified plaque with a strong circumferential enhancement, showing a mean wall concentration at 4.5 mg/mL of AuNP. (B) Calcified plaque with a strong enhancement within and around the calcified area, showing a mean wall concentration at 2.74 mg/mL of AuNP. Spotty enhancements were more discernable on the gold K-edge image than on the conventional image. (C) Quantitative analysis of the mean gold concentration found in the whole atherosclerotic rabbit abdominal aortic wall.

After AuNP injection, plaque enhancement and calcifications were not differentiable on conventional CT images because of similar attenuation values. The detection of any enhancement within a calcification was not possible with conventional images, even when

making a comparison between pre and post injection images. Contrast uptake was identifiable only on gold K-edge images. Furthermore, enhancement on gold K-edge images was sometimes co-localized with calcifications (**Figure 4**).

Aortic wall enhancement for atherosclerotic animals was the highest on conventional and gold K-edge images at D2. At this time point, atherosclerotic aortic walls had extended heterogeneous enhancement in terms of distribution (either large or punctate) and intensity on conventional and gold K-edge images. But punctate enhancements were more easily detected on gold K-edge images than on conventional images due to the background signal from the wall itself on conventional images. Conversely, no enhancement was observed for control, non-atherosclerotic aortas (**Figures 4 and 5, Supplemental Figures 1-3**).

At D2, after injection of an iodinated vascular contrast agent, both conventional and iodine images showed a good enhancement of the lumen with visualization of an irregular aortic diameter and enlargement of the infrarenal aorta (indicating aneurismal development), as well as high attenuating spots within the wall. We did not observe any stenosis, thromboses, or ulcerations in any animal. Conventional and iodine images failed to differentiate between areas of high attenuating wall and the enhanced lumen. Only gold K-edge images depicted specifically the enhancements within the wall. Simultaneous differentiation between the iodine enhanced lumen and the AuNP enhanced atherosclerotic macrophage burden was thus possible owing to the bicolor imaging capability of SPCCT (**Figure 5**).

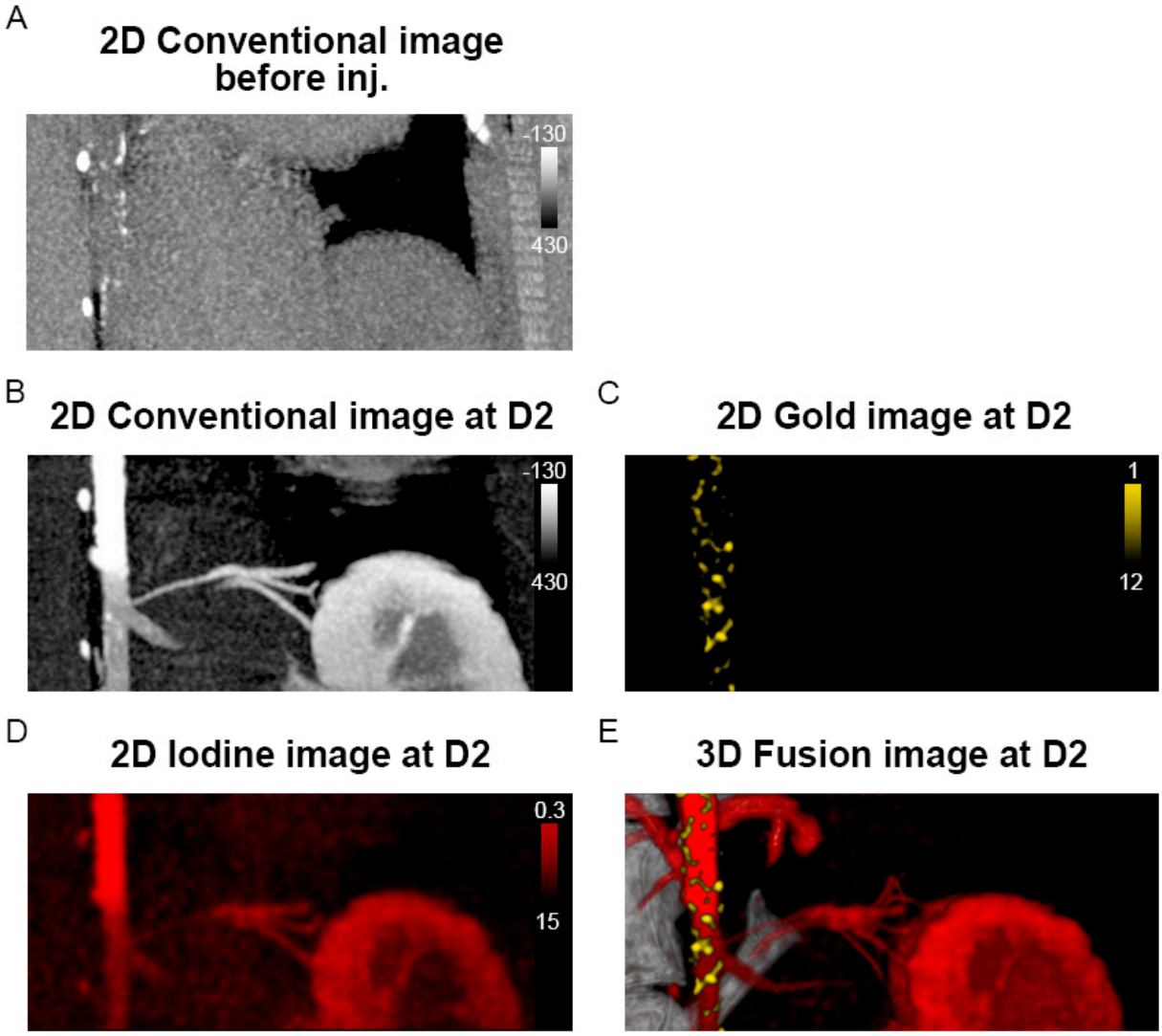


**Figure 5. Bicolor imaging of atherosclerotic rabbit aorta before and two days after injection of AuNP.** (A) Pre-injection conventional imaging shows the presence of focal hyper attenuation along the aortic wall in favor of calcifications. (B-E) *In vivo* bicolor SPCCT angiography imaging at the level of the abdomen of an atherosclerotic rabbit injected with a vascular contrast agent (Iomeron, 400 mg/mL) at two days after injection of AuNP. The lumens of aortic and renal arteries, enhancement of the kidney and dense wall lesions are apparent on maximum-intensity-projection (MIP) conventional (B) and iodine images (D). MIP gold K-edge images showed extensive, heterogeneous enhancement of the wall (C). Fusion of 3D volume rendering and gold K-edge image merged along with iodine image, and bone tissue (after segmentation on conventional images)(E), shows the spatial distribution of the atherosclerotic macrophage burden within the aortic wall.

*Macrophage burden quantification in the aortic wall by gold K-edge imaging in vivo*

For atherosclerotic rabbits, a significant increase in aortic wall enhancement two days after AuNP injection was measured on gold K-edge images with a mean(SD)=1.07(0.36) mg/mL

(range: 0.45 ; 1.56) vs mean(SD): 0.28(0.22) mg/mL (range: 0.01 ; 0.66) before injection (*P*=0.001) (**Figure 4, Table 1**) and also on conventional images with a mean(SD)=7(15) HU (range: -7 ; 33) vs mean(SD)=-11(21) HU (range: -35 ; 33) before injection (*P*=0.003). For control rabbits, no significant increase was measured on gold K-edge images (*P*>0.05) and conventional images (*P*>0.05).

Furthermore, the average gold quantity on gold K-edge images within the atherosclerotic aortic samples measured by SPCCT was 2.73(0.92) mg (range: 1.15 ; 3.98). This high quantity of gold was confirmed by ICP-OES with a quantity of gold measured at 1.53(0.55) mg (range: 0.64 ; 2.17).

| **Gold concentration** | **Pre-injection** | **5 min** | **45 min** | **Day 1** | **Day 2** |
|---|---|---|---|---|---|
| **Mean** (mg/mL) | 0.28 | 0.74 | 0.72 | 0.70 | 1.07 |
| **Standard Deviation** (mg/mL) | 0.22 | 0.27 | 0.28 | 0.23 | 0.36 |
| **Minimum** (mg/mL) | 0.01 | 0.37 | 0.33 | 0.37 | 0.42 |
| **Maximum** (mg/mL) | 0.66 | 1.04 | 1.16 | 1.032 | 1.56 |

**Table 1.** Gold concentrations within the aortic walls of atherosclerotic rabbits measured from SPCCT images at the time points noted.

*Macrophage burden quantification in atherosclerotic plaque by gold K-edge imaging in vivo and correlation with macrophage burden in immunohistochemistry*

Gold concentration was measured two days after injection on gold K-edge images in adjacent sections (n = 7 animals, 35 sections analyzed) and was found to be mean(SD) = 2.05(1.0) mg/mL (range: 0.13 ; 4.5), while the attenuation on conventional images was mean(SD) = 70.7(23.0) HU (range: 14.4 ; 138.2). The area immunostained for macrophages with RAM11 on corresponding aorta sections was measured to be mean(SD)=21.5%(10.5)(range: 1.0 ; 47.1).

A good correlation between the gold concentration measured within the wall on gold K-edge images and the macrophage area was found (Pearson correlation: r=0.82 with a 95% confidence interval at [0.67; 0.91], *P*=0.0001). Conversely, poor correlation was obtained between the attenuation values measured within the wall on conventional images and the macrophage area (r: 0.41, 95% confidence interval [0.09; 0.65] *P*=0.01)(**Figure 6**).

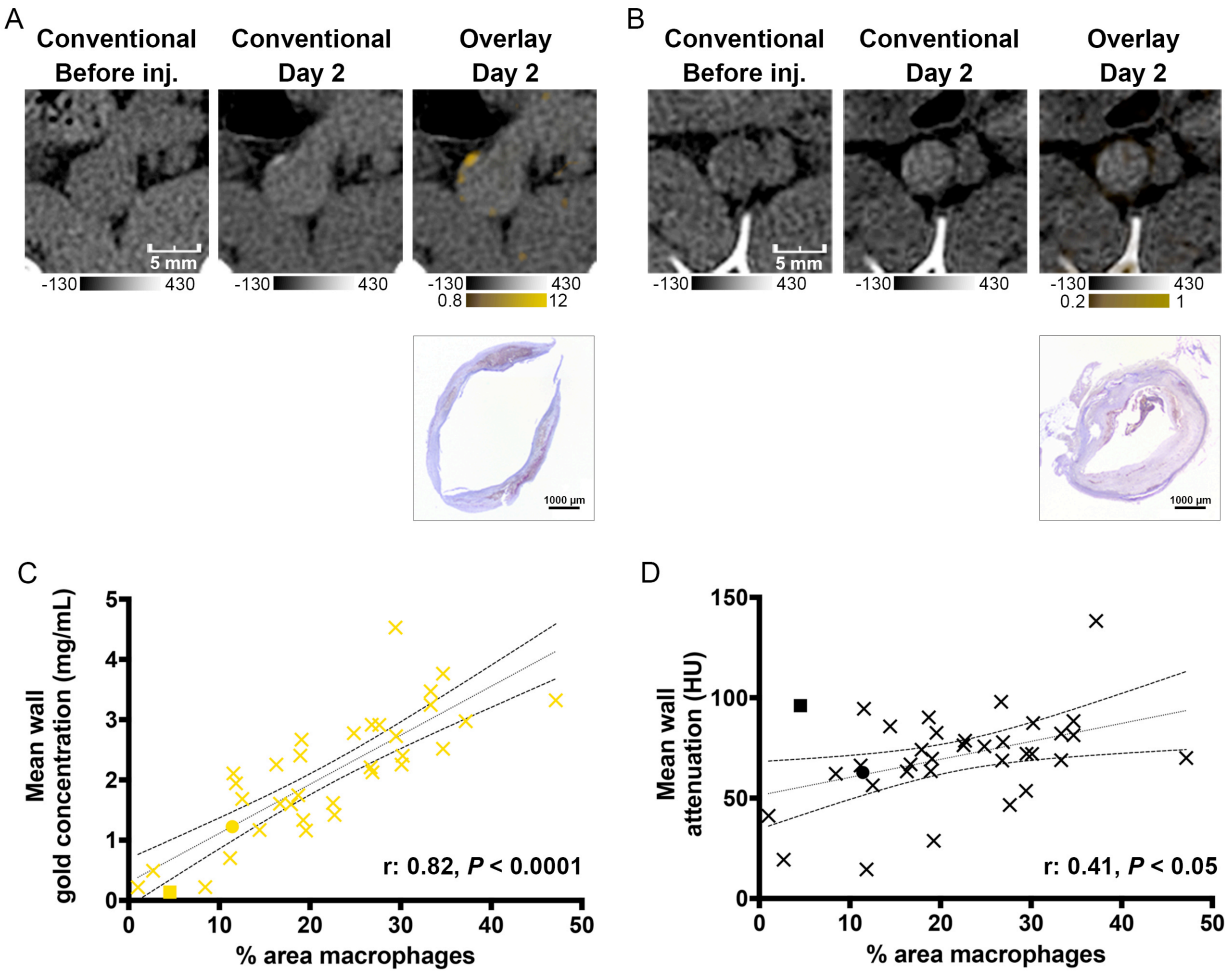


**Figure 6. Monocolor SPCCT imaging of atherosclerotic macrophage burden two days after injection, in comparison with immunostaining.** (A) Matched SPCCT images and immunostaining section of a non-calcified plaque, showing matches of the spotty enhancements next to the mesenteric artery branch. This section is represented by a yellow dot on (C), and black dot on (D). (B) Matched SPCCT images and immunostaining section of a calcified plaque, showing the low enhancement on the gold K-edge image confirmed by the low concentration of immunostained macrophages. This section is represented by a yellow square on (C), and black square on (D). (C-D) Correlation and linear regression analysis between the area immunostained for macrophages and (C) the concentration of gold or (D) the attenuation on conventional images.

*Ex vivo analyses*

The majority of the plaque (57%) was graded as IV, confirming presence of atheroma accordingly to the AHA classification (**Table 2**). More importantly, 23(66%) plaques were presented with calcifications. Macrophage foam cells were detected around lipid cores and also in high-infiltrated fibro-inflammatory cells at the intima inner surface, as confirmed by immunostaining with RAM11 (**Supplemental Figure 4**). No macrophage foam cells were

found in the media or the adventitia. In non-atherosclerotic rabbits, neither lipid core, calcification nor layer disorganization were observable (**Supplemental Figure 1**).

| Atherosclerotic plaques (n=35) | n(%) |
|---|---|
| **Intima fibrocellular infiltration** | 35 (100%) |
| **Macrophage foam cell** | 35 (100%) |
| **Smooth muscle cell** | 35 (100%) |
| **Lipid core** | 20 (57%) |
| **Calcification** | 23 (66%) |
| **AHA grade II** | 6 (17%) |
| **AHA grade III** | 9 (25%) |
| **AHA grade IV** | 20 (57%) |

**Table 2.** Atherosclerotic plaque characteristics prevalence and classification according to the AHA (American Heart Association), determined by histology.

TEM confirmed the presence of macrophages and foam cells in high concentrations around lipid cores as well as the presence of AuNP in the plaques of all atherosclerotic rabbits, while AuNP were not found in control, non-atherosclerotic rabbits. AuNP were distributed in high concentrations intracellularly next to lipid inclusions likely due to phagocytosis by the macrophage derived cells (**Supplemental Figure 5**). Note that such deposition was not observed neither extracellularly in the extracelluar matrix nor intracellularly aside from the foam cells (**Supplemental Figure 6**).

## DISCUSSION

Our results demonstrate specific detection and quantification of macrophage burden in atherosclerotic rabbits using gold K-edge imaging on a SPCCT system in combination with AuNP. We also show the feasibility of "bicolor imaging" for specific differentiation between enhancement of the lumen with one iodinated contrast agent and enhancement of the aortic wall with K-edge AuNP. Our results demonstrate the potential for simultaneous assessment of different diagnostic tasks in atherosclerosis, i.e. evaluation of the lumen in terms of stenosis measurement and thrombus detection, and evaluation of the plaque in terms of composition and vulnerability.

*In vivo* macrophage burden CT imaging has previously been reported with an iodinated nanoparticle formulation using conventional CT imaging in atherosclerotic rabbits (22). However, in this study, calcifications in the aortic wall could not be detected. Indeed, materials with different chemical compositions can be represented by similar pixel values on

conventional CT images, which means that detection of contrast uptake in atherosclerotic plaques can be confounded by the presence of calcifications that are frequently observed in CAD (4,23). When using conventional CT imaging, calcifications will thus interfere with macrophage burden quantification, which is usually observed in early-stage atherosclerosis (24) and subsequently hinder the assessment of vulnerable plaque. Even pre-injection imaging with CT would not be satisfactory because of strong artifacts surrounding the calcifications that could mask small focal enhancement. Therefore, there is a need for a specific imaging technique such as SPCCT K-edge imaging that as demonstrated by several proof-of-concept studies its capacity to specifically detect and quantify contrast agents (7–10,14–16,25,26).

An ideal SPCT contrast agent for the evaluation of coronary arteries needs to combine macrophage specificity and a high payload of an element suitable for K-edge imaging, such as ytterbium, gadolinium, or AuNP, among others (25–27). Previously, Cormode *et al.* reported using gold nanoparticles that gold K-edge imaging could detect the macrophage burden in an *ex vivo* mouse model (28). However, the animal model and the technical limitations of the system, particularly the low count rate capability and very long scanning time (~12-24 hours), were strong limitations for considering feasibility for CAD imaging. In the present study, using a SPCCT prototype system, we demonstrate *in vivo* that K-edge imaging is a good imaging technique to (1) visualize the macrophage burden even in the presence of calcifications, (2) characterize the plaques by demonstrating the presence of AuNP uptake in the macrophages, and (3) quantify the macrophage burden with greater accuracy than conventional CT imaging, thus fulfilling the molecular imaging expectations (29). Accordingly, unlike the attenuation of the aortic wall measured on conventional CT images, the quantity of AuNP in the aortic wall measured in gold K-edge images strongly correlated with the macrophage covered area by immunostaining.

Two key factors enable the uptake in macrophages. First, a long circulation time and penetration into diseased tissue as observed with PEG-coated nanoparticles (10,30), and second the high concentration of macrophages within atherosclerotic plaques (19,31). In our study, these factors were optimally met two days after injection when the specific visualization and quantification of overall macrophage burden on gold K-edge imaging demonstrated the uptake of AuNP by macrophage foam cells in the aortic wall of atherosclerotic rabbits. This period of time allowed macrophage foam cells to phagocytize enough agent to exceed the current sensitivity of K-edge imaging, *i.e.* a concentration in the range of mg/mL, as suggested before for molecular CT imaging (8,32). The uptake of the

AuNP by the macrophage foam cells in the aortic wall was also confirmed by (1) macrophage infiltration in corresponding histological sections, (2) AuNP uptake by macrophages foam cells in TEM, and (3) AuNP quantification by ICP-OES in *ex vivo* aorta. Another important feature of K-edge imaging is the possibility to perform "bicolor imaging", which is mostly done with optical imaging techniques (29,33). Using this feature we were able to differentiate the atherosclerotic lumen aorta enlargement labeled with an iodine-based contrast agent from the hallmarks of the inflammatory plaques labeled with AuNP. Therefore, we confirmed that K-edge imaging presents anatomical information of the lumen and molecular information of the inflammation plaques simultaneously, as suggested in previous studies (9,28), as opposite to alternative imaging modality such as F-18 FDG PET (18). Taken together, these key features make this modality a promising tool for CAD imaging.

**Study limitations**

The prediction of risk of plaque rupture from SPCCT imaging was beyond the scope of this study. However, the first step was to confirm the ability of K-edge imaging to be an effective imaging modality for evaluating macrophage burden. In addition, the long-term clearance of AuNP from atherosclerotic plaque was not assessed. Based on a previous work (10), their presence in the macrophages might be persistent over time, which would encourage the development of rapid targeted cleared K-edge contrast agents before human use.

**Conclusion**

SPCCT enabled gold K-edge imaging allows specific detection and quantification of the macrophage burden within calcified atherosclerotic plaques and "bicolor imaging" for simultaneous anatomical and molecular imaging of atherosclerosis.

## REFERENCES

1. Writing Group Members, Mozaffarian D., Benjamin EJ., et al. Executive Summary: Heart Disease and Stroke Statistics--2016 Update: A Report From the American Heart Association. Circulation 2016;133(4):447–54. Doi: 10.1161/CIR.0000000000000366.

2. Naghavi M., Libby P., Falk E., et al. From vulnerable plaque to vulnerable patient: a call for new definitions and risk assessment strategies: Part I. Circulation 2003;108(14):1664–72. Doi: 10.1161/01.CIR.0000087480.94275.97.

3. Libby P. Inflammation in atherosclerosis. Nature 2002;420(6917):868–74. Doi: 10.1038/nature01323.

4. Prati F., Mallus MT., Broglia L., Albertucci M. Integrated non-invasive imaging techniques. EuroIntervention J Eur Collab Work Group Interv Cardiol Eur Soc Cardiol 2010;6 Suppl G:G161-168. Doi: 10.4244/.

5. Taguchi K., Iwanczyk JS. Vision 20/20: Single photon counting x-ray detectors in medical imaging. Med Phys 2013;40(10):100901. Doi: 10.1118/1.4820371.

6. Willemink MJ., Persson M., Pourmorteza A., Pelc NJ., Fleischmann D. Photon-counting CT: Technical Principles and Clinical Prospects. Radiology 2018;289(2):293–312. Doi: 10.1148/radiol.2018172656.

7. Si-Mohamed S., Bar-Ness D., Sigovan M., et al. Review of an initial experience with an experimental spectral photon-counting computed tomography system. Nucl Instrum Methods Phys Res Sect Accel Spectrometers Detect Assoc Equip 2017. Doi: 10.1016/j.nima.2017.04.014.

8. Si-Mohamed S., Bar-Ness D., Sigovan M., et al. Multicolour imaging with spectral photon-counting CT: a phantom study. Eur Radiol Exp 2018;2(1):34. Doi: 10.1186/s41747-018-0063-4.

9. Cormode DP., Si-Mohamed S., Bar-Ness D., et al. Multicolor spectral photon-counting computed tomography: in vivo dual contrast imaging with a high count rate scanner. Sci Rep 2017;7(1):4784. Doi: 10.1038/s41598-017-04659-9.

10. Si-Mohamed S., Cormode DP., Bar-Ness D., et al. Evaluation of spectral photon counting computed tomography K-edge imaging for determination of gold nanoparticle biodistribution in vivo. Nanoscale 2017;9(46):18246–57. Doi: 10.1039/c7nr01153a.

11. Sigovan M., Si-Mohamed S., Bar-Ness D., et al. Feasibility of improving vascular imaging in the presence of metallic stents using spectral photon counting CT and K-edge imaging. Sci Rep 2019;9(1):19850. Doi: 10.1038/s41598-019-56427-6.

12. Symons R., De Bruecker Y., Roosen J., et al. Quarter-millimeter spectral coronary stent imaging with photon-counting CT: Initial experience. J Cardiovasc Comput Tomogr 2018;12(6):509–15. Doi: 10.1016/j.jcct.2018.10.008.

13. Symons R., Sandfort V., Mallek M., Ulzheimer S., Pourmorteza A. Coronary artery calcium scoring with photon-counting CT: first in vivo human experience. Int J Cardiovasc Imaging 2019;35(4):733–9. Doi: 10.1007/s10554-018-1499-6.

14. Si-Mohamed S., Thivolet A., Bonnot P-E., et al. Improved Peritoneal Cavity and Abdominal Organ Imaging Using a Biphasic Contrast Agent Protocol and Spectral Photon

Counting Computed Tomography K-Edge Imaging. Invest Radiol 2018;53(10):629–39. Doi: 10.1097/RLI.0000000000000483.

15. Si-Mohamed S., Tatard-Leitman V., Laugerette A., et al. Spectral Photon-Counting Computed Tomography (SPCCT): in-vivo single-acquisition multi-phase liver imaging with a dual contrast agent protocol. Sci Rep 2019;9(1):8458. Doi: 10.1038/s41598-019-44821-z.

16. Cuccione E., Chhour P., Si-Mohamed S., et al. Multicolor spectral photon counting CT monitors and quantifies therapeutic cells and their encapsulating scaffold in a model of brain damage. Nanotheranostics 2020;4:4(3): 129-141. Doi: 10.7150/ntno.45354.

17. Thivolet A., Si-Mohamed S., Bonnot P-E., et al. Spectral photon-counting CT imaging of colorectal peritoneal metastases: initial experience in rats. Sci Rep 2020;10(1):13394. Doi: 10.1038/s41598-020-70282-w.

18. Zhang Z., Machac J., Helft G., et al. Non-invasive imaging of atherosclerotic plaque macrophage in a rabbit model with F-18 FDG PET: a histopathological correlation. BMC Nucl Med 2006;6:3. Doi: 10.1186/1471-2385-6-3.

19. Phinikaridou A., Hallock KJ., Qiao Y., Hamilton JA. A robust rabbit model of human atherosclerosis and atherothrombosis. J Lipid Res 2009;50(5):787–97. Doi: 10.1194/jlr.M800460-JLR200.

20. Naha PC., Chhour P., Cormode DP. Systematic in vitro toxicological screening of gold nanoparticles designed for nanomedicine applications. Toxicol In Vitro 2015;29(7):1445–53. Doi: 10.1016/j.tiv.2015.05.022.

21. Schneiderman G., Pritchard WF., Ramírez CA., Colton CK., Smith KA., Stemerman MB. Rabbit aortic medial thickness under relaxed and specified simulated in vivo conditions. Am J Physiol 1983;245(4):H623-627. Doi: 10.1152/ajpheart.1983.245.4.H623.

22. Schneider CA., Rasband WS., Eliceiri KW. NIH Image to ImageJ: 25 years of image analysis. Nat Methods 2012;9(7):671–5. Doi: 10.1038/nmeth.2089.

23. Stary HC., Chandler AB., Dinsmore RE., et al. A definition of advanced types of atherosclerotic lesions and a histological classification of atherosclerosis. A report from the Committee on Vascular Lesions of the Council on Arteriosclerosis, American Heart Association. Circulation 1995;92(5):1355–74. Doi: 10.1161/01.cir.92.5.1355.

24. Horak D., Babic M., Jendelová P., et al. D-mannose-modified iron oxide nanoparticles for stem cell labeling. Bioconjug Chem 2007;18(3):635–44. Doi: 10.1021/bc060186c.

25. Hyafil F., Cornily J-C., Feig JE., et al. Noninvasive detection of macrophages using a nanoparticulate contrast agent for computed tomography. Nat Med 2007;13(5):636–41. Doi:

10.1038/nm1571.

26. Joshi NV., Vesey AT., Williams MC., et al. 18F-fluoride positron emission tomography for identification of ruptured and high-risk coronary atherosclerotic plaques: a prospective clinical trial. Lancet Lond Engl 2014;383(9918):705–13. Doi: 10.1016/S0140-6736(13)61754-7.

27. Aikawa E., Nahrendorf M., Figueiredo J-L., et al. Osteogenesis associates with inflammation in early-stage atherosclerosis evaluated by molecular imaging in vivo. Circulation 2007;116(24):2841–50. Doi: 10.1161/CIRCULATIONAHA.107.732867.

28. Kim J., Bar-Ness D., Si-Mohamed S., et al. Assessment of candidate elements for development of spectral photon-counting CT specific contrast agents. Sci Rep 2018;8(1):12119. Doi: 10.1038/s41598-018-30570-y.

29. Halttunen N., Lerouge F., Chaput F., et al. Hybrid Nano-GdF3 contrast media allows pre-clinical in vivo element-specific K-edge imaging and quantification. Sci Rep 2019;9(1):12090. Doi: 10.1038/s41598-019-48641-z.

30. Pan D., Schirra CO., Senpan A., et al. An early investigation of ytterbium nanocolloids for selective and quantitative "multicolor" spectral CT imaging. ACS Nano 2012;6(4):3364–70. Doi: 10.1021/nn300392x.

31. Cormode DP., Roessl E., Thran A., et al. Atherosclerotic plaque composition: analysis with multicolor CT and targeted gold nanoparticles. Radiology 2010;256(3):774–82. Doi: 10.1148/radiol.10092473.

32. Sinusas AJ., Bengel F., Nahrendorf M., et al. Multimodality cardiovascular molecular imaging, part I. Circ Cardiovasc Imaging 2008;1(3):244–56. Doi: 10.1161/CIRCIMAGING.108.824359.

33. Lobatto ME., Calcagno C., Millon A., et al. Atherosclerotic plaque targeting mechanism of long-circulating nanoparticles established by multimodal imaging. ACS Nano 2015;9(2):1837–47. Doi: 10.1021/nn506750r.

34. Libby P. Inflammation in atherosclerosis. Nature 2002;420(6917):868–74. Doi: 10.1038/nature01323.

35. Weissleder R., Mahmood U. Molecular imaging. Radiology 2001;219(2):316–33. Doi: 10.1148/radiology.219.2.r01ma19316.

36. Steinberg I., Huland DM., Vermesh O., Frostig HE., Tummers WS., Gambhir SS. Photoacoustic clinical imaging. Photoacoustics 2019;14:77–98. Doi: 10.1016/j.pacs.2019.05.001.

# SUPPLEMENTAL METHODS AND REFERENCES

## Animal acquisitions protocol

Anesthesia was induced with 0.25 mg/kg intramuscular injection of medetomidine (0.15 mg/mL, Orion Pharma, Orion Corporation, Espoo, Finland) and 15 mg/kg intramuscular injection of ketamine (10.0 mg/mL, Merial, Lyon, France) and maintained with isoflurane (concentration between 0.5-2.5%) in oxygen (0.4L/min) and air (0.3L/min). A 22-gauge auricular vein catheter was placed and rabbits were positioned on their backs. A veterinary handheld pulse oximeter and carbon dioxide detector (Model 9847V, Nonin Medical, Inc, Plymouth, Minnesota) with a remote pulse sensor were placed on the earlobe and used to monitor the heart beat and oxygen saturation. After the last imaging session, animals were euthanized using a lethal dose of Dolethal (Vetoquinol, Kontichsesteenweg, Aartselaar, BELGIUM).

## SPCCT imaging experiments

We performed an initial *in vitro* acquisition on three 1.5-mL polypropylene centrifuge tubes with different compositions: one containing calcium phosphate (used to model a highly dense calcification), one containing AuNP (AuNP, 4 mg/mL), and one containing an iodine-based contrast agent (iomeron, 4 mg/mL, Iomeprol; BRACCO, Milan, ITALY). The tubes were placed in a custom-made polyoxymethylene cylindrical phantom with a diameter of 13 cm and 10 holes of 1.5 cm in diameter, which was scanned as per the protocol described above.

## SPCCT image reconstruction

Conventional images were generated from the photon counts summed from the five energy bins, as is proposed with current non-PCDs CT systems. The specificity of the spectral image was the image chain based on a two-step approach (1): (1) generating sinograms for each energy bin and (2) generating each material image (water, iodine, and gold K-edge) separately using a filtered back-projection reconstruction based on a maximum likelihood material decomposition algorithm, as previously published (2). To minimize material decomposition errors, pile-up was corrected by a look-up table, which relates the actual photon flux to the one counted in the different energy bins. The reconstruction algorithm was adjusted for gold discrimination.

## SPCCT image analysis

For qualitative image analysis, 250 µm voxel size conventional and spectral images were used. For quantitative analysis, a 2 pixel sigma Gaussian filter was used to decrease the noise (standard deviation of the mean) by a factor between 2 and 4 without significantly changing the mean values (3). Gold K-edge images were overlaid on conventional images with appropriate windowing of the gold concentrations. A lookup table based windowing method was used to threshold calcium and bone on conventional images before AuNP injection. This allowed differentiation of calcium deposition from gold uptake at post-injection imaging time points.

**REFERENCES**

1. Schlomka JP., Roessl E., Dorscheid R., et al. Experimental feasibility of multi-energy photon-counting K-edge imaging in pre-clinical computed tomography. Phys Med Biol 2008;53(15):4031–47. Doi: 10.1088/0031-9155/53/15/002.

2. Heuscher D., Brown K., Noo F. Redundant data and exact helical cone-beam reconstruction. Phys Med Biol 2004;49(11):2219–38. Doi: 10.1088/0031-9155/49/11/008.

3. Si-Mohamed S., Thivolet A., Bonnot P-E., et al. Improved Peritoneal Cavity and Abdominal Organ Imaging Using a Biphasic Contrast Agent Protocol and Spectral Photon Counting Computed Tomography K-Edge Imaging. Invest Radiol 2018;53(10):629–39. Doi: 10.1097/RLI.0000000000000483.

## SUPPLEMENTAL FIGURES

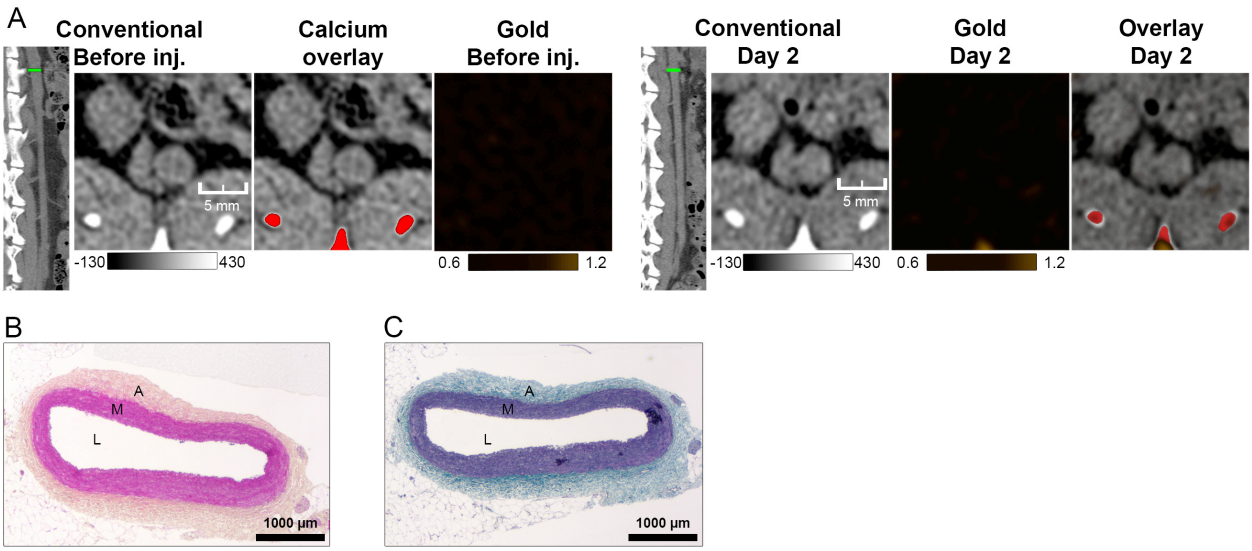


**Supplemental Figure 1.** Non-atherosclerotic control rabbit aorta imaging and histology. (A) Regular aorta diameters without any aneurisms, calcifications, or enhancement of the wall two days after injection was observed from axial and sagittal aorta imaging. Histology showed conservation of layers without any fibro-cellular and calcification infiltration (L: lumen, M: media, A: adventitia) on HES staining (for aortic wall layers)(B) and Wiegert staining (for elastin fibers)(C). Note that the intima is not observable because of the absence of infiltration in case of healthy rabbit model.

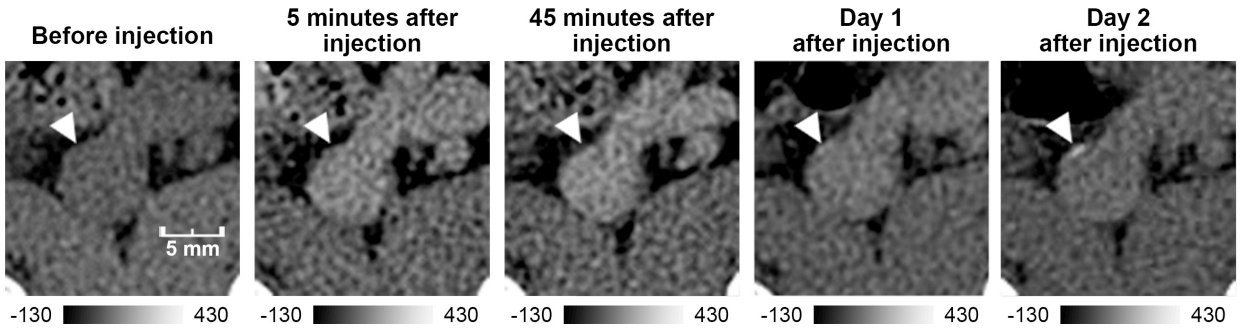


**Supplemental Figure 2. Follow-up imaging of a focal atherosclerotic plaque (white arrow head) shows highest enhancement at two days after injection.** From left to right: Axial (voxel size 250mm3) conventional before injection, 5 and 45 minutes after injection, one day and two days after injection.

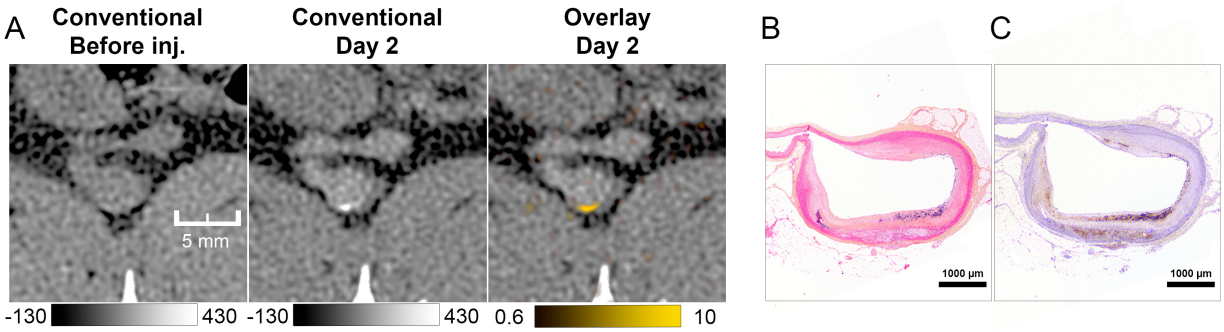


**Supplemental Figure 3. Monocolor SPCCT imaging of atherosclerotic rabbit aorta before and two days after injection of AuNP, at the level of the right renal artery.** Axial (voxel size 250mm3) conventional (first column) before injection, overlay between Gold K-edge image and conventional image (second column).

(A) Atherosclerotic plaque with semi-circumferential enhancement 2 days after injection on Gold K-edge image showed a clear depiction of macrophage burden. The mean concentration of gold was measured at 2.08 mg/mL, and the area of macrophages at 11.7%.

(B) Axial corresponding plaque section after HES staining showed a thick and fibrotic intima with high fatty streaks and macrophages infiltration, while the wall along the renal artery showed no sign of atherosclerosis as well as macrophage burden.

(C) Axial corresponding plaque section after immunohistochemistry for macrophages with a monoclonal RAM-11 antibody counterstained with hematoxylin. Intense focal infiltration of macrophages is showed, confirming the gold K-edge enhancement nearly depictable on conventional images, while no macrophage burden is shown within the left renal artery wall as expected.

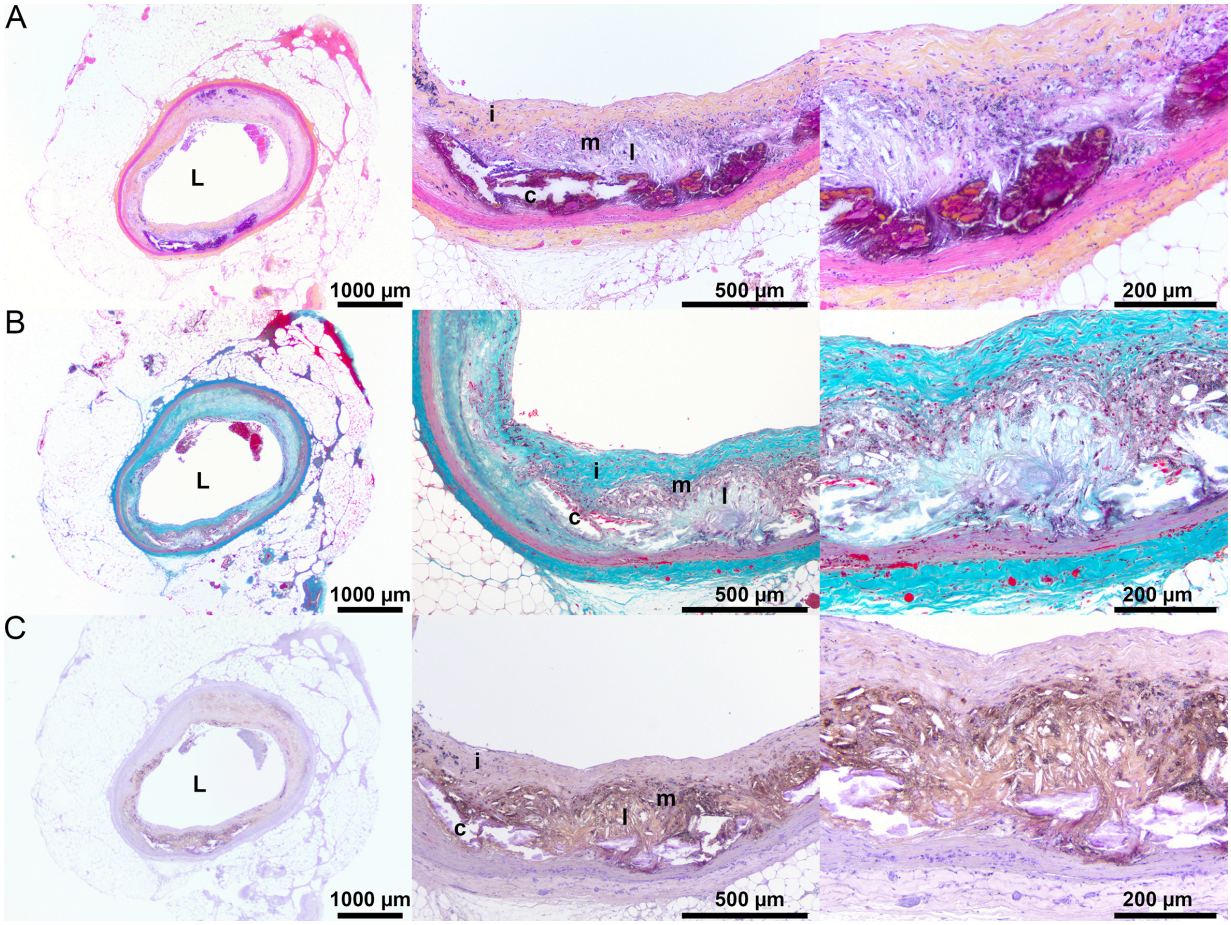


**Supplemental Figure 4. Histology of atheroma (similar to AHA type IV human plaque) in an atherosclerotic rabbit abdominal artery.** (A) First row: HES staining (for aortic wall layers), (B) Second row: Wiegert staining (for elastin fibers), (C) Third row: immunostaining with RAM-11 (for macrophages). Severe disorganization of the intima (i) was found because of large lipid-rich cores (l) containing cholesterol crystals, surrounded by macrophage (m) foam cells infiltration mainly at the inner surface, smooth muscle cells with and without lipid droplet inclusions and calcific degeneration at the intima outer edge (c).

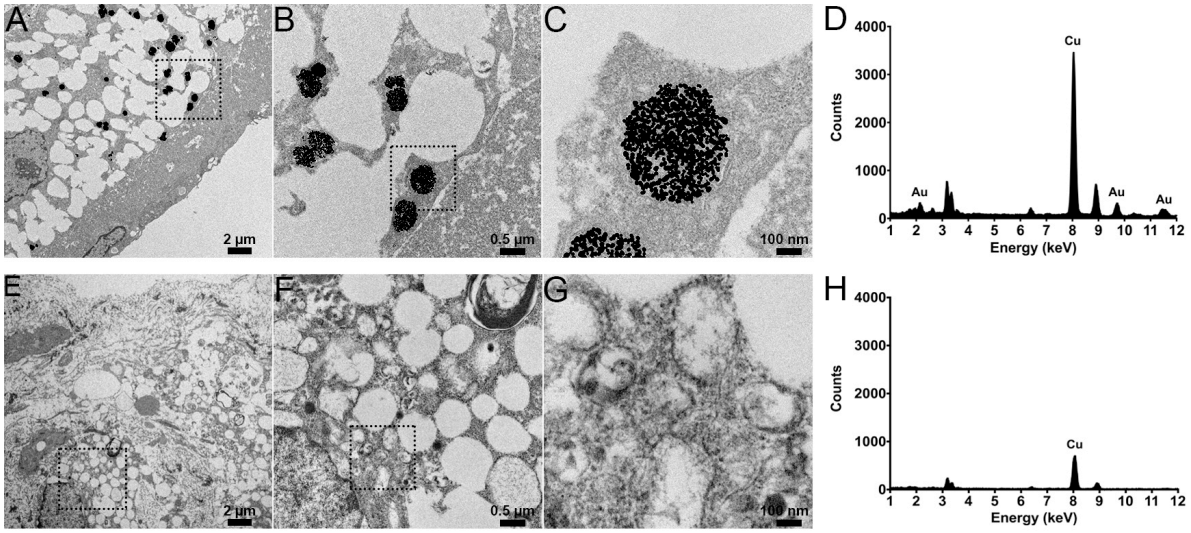


**Supplemental Figure 5. Transmission electron micrographs and EDS of atherosclerotic and control non atherosclerotic aorta two days after injection of AuNP over a range of magnifications.** A–D: Atherosclerotic rabbit aorta, E–H: Control non atherosclerotic rabbit aorta. (A-C) Numerous electron-dense granules were detected next to lipid inclusions in lysosomes of macrophages (foam cells) from atherosclerotic rabbit aorta, sacrificed two days after injection of AuNP. Note that nanoparticles have preserved their size and morphology. (D) The characteristic absorption spectrum of gold was detected with energy dispersion spectroscopy in the area of electron-dense granules. (E-H) No such granule was detected within macrophages from control rabbits, despite the presence of lipid inclusions in lysosomes. Energy dispersion spectroscopy in the area of electron-dense granules did not detect the spectrum of gold in non-atherosclerotic animals.

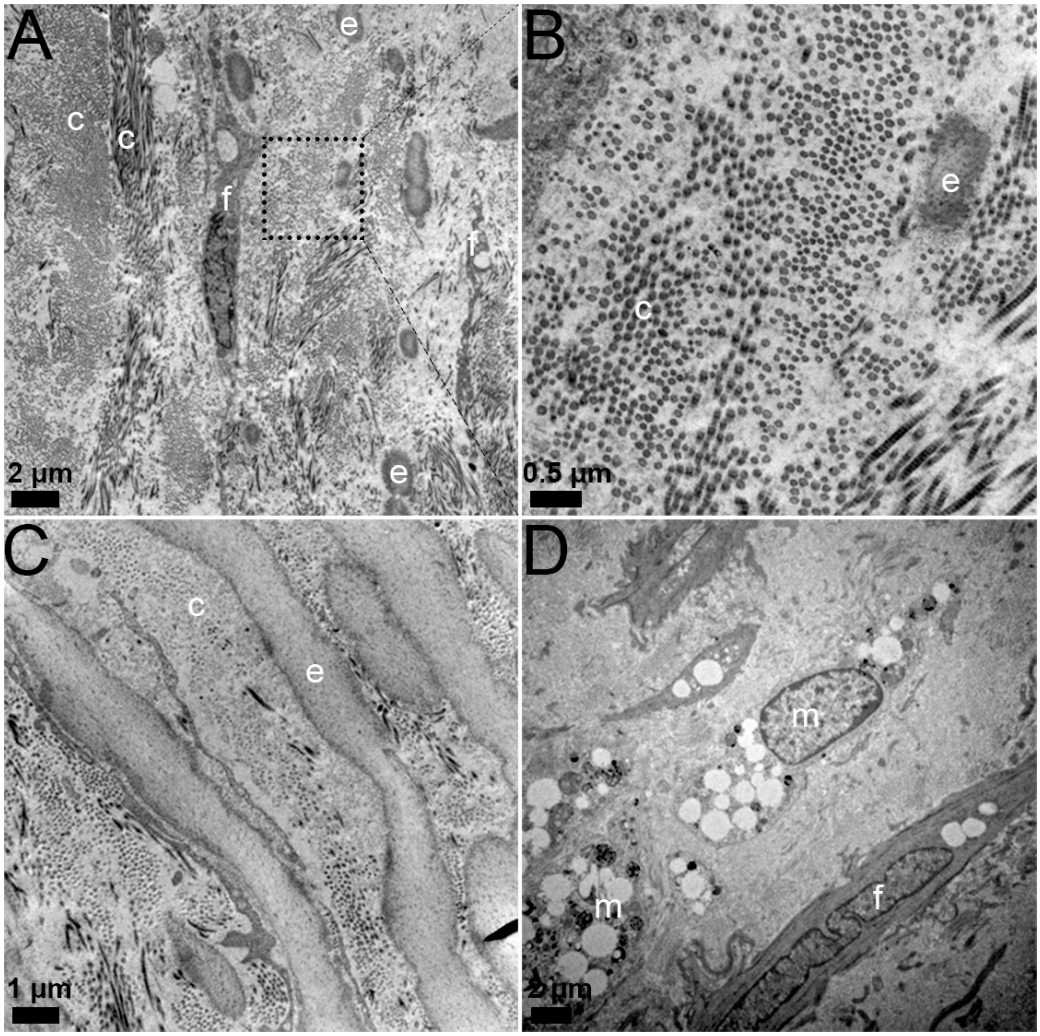


**Supplemental Figure 6. Transmission electron micrographs of atherosclerotic aorta two days after injection of AuNP over a range of magnifications** (A-C) Visualization of the extracellular matrix with collagen and elastin fibers nearby fibroblasts without evidence of nanoparticles deposition (c: collagen, e: elastin, f: fibroblast). (D) Visualization of a fibroblast without nanoparticles deposition, nearby numerous electron-dense granules within foam cells.

# Annex studies

# Annex Study 1

**Title: Feasibility of improving vascular imaging in the presence of metallic stents using spectral photon counting CT and K-edge imaging**

M.Sigovan[1], S. Si-Mohamed[1,2] (First equal with equal contribution), D. Bar-Ness[2], J. Mitchell[3], J.B. Langlois[4], P. Coulon[5], E. Roessl[6], I. Blevis[7], M. Rokni[7], G. Rioufol[1], P. Douek[1,2], L. Boussel[1,2]

1. Hospices Civils de Lyon, Louis Pradel Cardiology Hospital, Lyon, France
2. Univ Lyon, INSA-Lyon, Université Claude Bernard Lyon 1, UJM-Saint Etienne, CNRS, Inserm, CREATIS UMR 5220, U1206, Lyon, France
3. Cardiac surgery, Hospices Civils de Lyon, Lyon, France
4. CERMEP Centre d'imagerie du vivant, Lyon, France
5. CT Clinical Science, Philips, Suresnes, France
6. Philips Research Laboratories, Hamburg, Germany
7. Global Advanced Technologies, CT, Philips, Haifa, Israel

## ABSTRACT

Correct visualization of the vascular lumen is impaired in standard computed tomography (CT) because of blooming artifacts, increase of apparent size, induced by metallic stents and vascular calcifications. Recently, due to the introduction of photon-counting detectors in the X-ray imaging field, a new prototype spectral photon-counting CT (SPCCT) based on a modified clinical CT system has been tested in a feasibility study for improving vascular lumen delineation and visualization of coronary stent architecture. Coronary stents of different metal composition were deployed inside plastic tubes containing hydroxyapatite spheres to simulate vascular calcifications and in the abdominal aorta of one New Zealand White (NZW) rabbit. Imaging was performed with an SPCCT prototype, a dual-energy CT system, and a conventional 64-channel CT system (B64). We found the apparent widths of the stents significantly smaller on SPCCT than on the other two systems *in vitro* ($p<0.01$), thus closer to the true size. Consequently, the intra-stent lumen was significantly larger on SPCCT ($p<0.01$). In conclusion, owing to the increased spatial resolution of SPCCT, improved lumen visualization and delineation of stent metallic mesh is possible compared to dual-energy and conventional CT.

# Annex Study 2

**Title: Assessment of candidate elements for development of spectral photon-counting CT specific contrast agents**

J. Kim[1,2], D. Bar-Ness[3,4], S. Si-Mohamed[3,4], P. Coulon[5], I. Blevis[6], P. Douek[3,4], D.P. Cormode [1,2]

[1]Department of Radiology, University of Pennsylvania, USA
[2]Department of Bioengineering, University of Pennsylvania, USA
[3]Department of Medicine, Hôpital Cardio-Vasculaire et Pneumologique Louis Pradel, Lyon, France.
[4]Centre de Recherche en Acquisition et Traitement de l'Image pour la Santé (CREATIS), UMR CNRS 5220, Inserm U1044, University Lyon1 Claude Bernard, Lyon, France.
[5]CT Clinical Science, Philips, Suresnes, France.
[6]Global Advanced Technologies, CT, Philips, Haifa, Israel.

## ABSTRACT

Spectral photon-counting computed tomography (SPCCT) is a rapidly emerging imaging modality that provides energy-dependent information on individual x-ray photons, leading to accurate material decomposition and simultaneous quantification of multiple contrast generating materials. Development of SPCCT-specific contrast agents is needed to overcome the issues with currently used iodinated contrast agents, such as difficulty in differentiation from calcified structures, and yield SPCCT's full promise. In this study, the contrast generation of different elements is investigated using a prototype SPCCT scanner based on a modified clinical CT system and suitable elements for novel contrast agent development for SPCCT imaging are identified. Furthermore, nanoparticles were synthesized from tantalum as a proof of concept spectral photon-counting CT agent and tested for their *in vitro* cytotoxicity and contrast generation to provide insight into the feasibility of nanoparticle contrast agent development from these elements. We found that gadolinium, ytterbium and tantalum generate high contrast in spectral photon-counting CT imaging and may be suitable elements for contrast agent development for this modality. Our proof of concept results with tantalum-based nanoparticles underscore this conclusion due to their detectability with spectral photon-counting CT, as well as their biocompatibility.

# Annex Study 3

**Title: Comparison of five one-step reconstruction algorithms for spectral CT**

C.Mory[1], B. Sixou[2], S. Si-Mohamed[3], L. Boussel[3], S. Rit[1]

[1]Université de Lyon, CREATIS ; CNRS UMR5220 ; Inserm U1206 ; INSA-Lyon ; Université Lyon 1 ; Centre Léon Bérard, France.
[2]Université de Lyon, CREATIS; CNRS UMR5220; InsermU1206; INSA-Lyon; France.
[3]Université de Lyon, CREATIS ; CNRS UMR5220 ; Inserm U1206 ; INSA-Lyon ; Université Lyon 1, France; Radiology Department, Lyon University Hospital, France

## ABSTRACT

Over the last decade, dual-energy CT scanners have gone from prototypes to clinically available machines, and spectral photon counting CT scanners are following. They require a specific reconstruction process, consisting of two steps: material decomposition and tomographic reconstruction. The two steps can be done separately in either order, but in both cases, some information is lost along the way. As an alternative, "one-step inversion" methods have been proposed, which perform decomposition and reconstruction simultaneously. For most CT applications, reconstruction time is critical for practical usability, and one-step methods are typically slower than their two-step counterparts. The goal of this paper is to provide an independent comparison of five one-step inversion algorithms, focused mainly on convergence speed, but also on memory footprint, stability, and ease of use. We adapted and implemented a Bayesian method which uses non-linear conjugate gradient for minimization, three methods based on quadratic surrogates, and a primal-dual method based on MOCCA, a modified Chambolle-Pock algorithm. Experiments were performed on both simulated and real data. Some of these methods can be accelerated by using μ-preconditioning, i.e. by performing all internal computations not with the actual materials the object is made of, but with carefully chosen linear combinations of those. In this paper, we also evaluate the impact of three different - preconditioners on convergence speed. Our results show that the method of Mechlem *et al.* is much faster than the others, while being only slightly less stable and more complex: it requires less than 100 iterations, versus several thousand for other methods. It seems to be the only viable candidate for implementation into a real multi-energy scanner.

# General Discussion

Dans ce travail de thèse, la faisabilité et l'évaluation de l'imagerie K-edge représente l'axe principal de recherche. Les premiers essais *in vitro* réalisés au début de la thèse ont démontré la faisabilité de discrimination spectrale d'un et de deux agents de contraste candidats à l'imagerie K-edge. Ces premiers résultats, alors innovants, représentaient le début de l'imagerie K-edge dans des conditions d'acquisition et de reconstruction proches de celles d'un système de TDM clinique, malgré un champ d'exploration limité à 160 mm et une rotation du tube à 0.75 secondes. Non seulement l'imagerie K-edge était possible en TDM spectrale à comptage photonique, mais elle était aussi réalisable dans plusieurs scénarios, c'est-à-dire pour plusieurs agents de contraste dédiés *in vitro* et *in vivo* chez l'animal tels que pour l'or et le gadolinium.

Mes travaux ont donc porté sur l'évaluation des performances mais aussi la compréhension des limites et des facteurs les influençant, cette démarche s'intégrant dans des développements collaboratifs technologiques et méthodologiques toujours en cours avec le partenaire industriel « Philips Research » à Haifa et Hambourg ainsi qu'avec le projet transversal « scanner spectral à comptage photonique » du laboratoire Creatis (Université de Lyon 1)[1].

Malgré des performances satisfaisantes pour une utilisation préclinique, la technologie du prototype de TDM spectrale à comptage photonique présente des imperfections à ce jour en cours d'investigation et de correction comme :

**A) dans la chaine de détection**, dont les trois principales limites sont l'empilement ("pile-up"), le rayonnement diffusé et la connaissance du modèle spectral (réponse spectrale du détecteur). a) Le pile-up : est phénomène non linéaire, prédominant à fort flux de photons dont la solution à ce jour est de limiter le flux de photons (c'est-à-dire baisser les mA en allongeant le temps de rotation si besoin pour conserver la valeur de mAs). b) Le rayonnement diffusé : il cause des artéfacts en détectant les rayons déviés de leur trajectoire rectiligne (et donc détectés dans le mauvais pixel détecteur). Le rayonnement diffusé augmente avec l'augmentation de la taille de l'objet et peut-être limité en plaçant une grille anti-diffusion devant le détecteur. c) La connaissance du modèle spectral: c'est à dire la juste modélisation des phénomènes linéaires au sein du détecteur (plus précisément au sein du matériau semi-conducteur comme le Cadmium Zinc Telluride (CZT), équippant le prototype utilisé : partage de charge et fluorescence principalement (qui donnent les matrices de réponse). Par ailleurs, il faut également prendre en compte l'instabilité de comportements des pixels, cause d'artéfacts en anneau (ring artefacts). En effet, les PCDs sont très sensibles expliquant que l'on puisse observer au sein d'un même détecteur un comportement

inhomogène, c'est à dire une réponse spectrale différente pour chaque pixel d'où la nécessité d'une calibration systématique et chronophage avant chaque acquisition. Cette connaissance du modèle spectral reste un point clé des systèmes de TDM spectrale à comptage photonique et une mauvaise connaissance mène à des erreurs de quantification et du cross-talk (détection d'os dans la carte de gadolinium par exemple).

**B) dans les conditions de basse dose de rayons X** responsables d' erreur de quantification imposant une optimisation des protocoles d'acquisition. Le bruit crée des incertitudes pour lesquelles des procédés dits de régularisation pourront être employés (dans la décomposition des sinogrammes ou dans l'image). Par exemple, la méthode de Frequency Split est depuis peu disponible en routine courante sur le système (développement interne chez Philips non publié). Elle permet pour un faible nombre de photons d'améliorer la décomposition des cinq canaux en sinogrammes matériaux. Elle combine une décomposition à haute résolution spatiale avec une décomposition spectrale basse résolution moins bruitée. De nombreuses autres stratégies de reconstruction d'images « matériaux » et l'utilisation de processus de reconstruction itératifs existent. Par exemple, les méthodes dites "One-Step" reconstruisent directement des cartes matériaux à partir des comptes de photons bruts [2, 3]. Ces méthodes restent pour l'instant lourdes en calcul et coûteuses en temps. De plus, elles présentent une texture du bruit dans l'image différente de la reconstruction conventionnelle avec rétroprojection filtrée. Enfin, cette méthode ne permet pas la correction d'autres facteurs d'erreur de quantification comme le diffusé résiduel.

**C) dans la chaine de décomposition des matériaux** avec les imperfections liées à l'optimisation de l'algorithme d'espérance-maximisation (MLEM pour Maximum Likelihood - Maximisation Expectation), qui décompose l'information en cinq sinogrammes (un sinogramme par fenêtre énergétique) mesurés par les PCDs en deux, trois ou quatre sinogrammes par base ou matériaux. Le ML-EM est un algorithme d'optimisation qui résoud le problème en faisant l'hypothèse d'un bruit de mesure poissonnien (par opposition à gaussien souvent utilisé aussi) et qui peut être mis en défaut lors d'une mauvaise estimation du modéle spectral.

Le choix des produits de contraste dédiés à l'imagerie K-edge est fondamental dans le cadre du développement de la TDM spectrale à comptage photonique. En effet, les agents de contraste basés sur des atomes à haut numéro atomique (et donc candidats à l'imagerie K-edge) sont potentiellement nombreux du fait de l'essor des nanobiotechnologies. Cela rend le choix du bon candidat de plus en plus difficile, et nécessite la réalisation entre autres d'études

de sensibilité comme dans le travail de thèse. Dans les travaux présentés *in vitro*, la sensibilité pour le gadolinium en comparaison avec l'or était plus élevée. Pour rappel, des seuils de sensibilité étaient plus élevés pour le gadolinium (0.64 mg/mL) que l'or (0.71 mg/mL) pour un CNR à 2. Cela s'explique très probablement par le flux de photons plus élevé autour du K-edge du gadolinium (50.2 keV) lié au protocole d'acquisition contraint à un seul kilovoltage à 120 kVp dont l'énergie moyenne est autour de 70 keV et dont l'énergie la plus fortement représentée correspondant à la raie du Tungstène à 59 keV [4, 5]. L'augmentation du kilovoltage du tube à rayons X permettrait d'augmenter le flux de photons autour du K-edge de l'or (~80.3 keV). De plus, une méthode de filtration des photons de basse énergie à la sortie du tube à rayons X pourrait être implémentée pour décaler l'énergie moyenne du faisceau polychromatique vers les hautes énergies, comme le fait un filtre étain installé sur un système de TDM double énergie (Somatom Force®, Siemens Healthineers) augmentant de 29% l'énergie moyenne à 100 kVp (76.0 keV) et de 37% à 150 kVp (98.6 keV)[6]. Enfin, le travail annexe présenté met en évidence dans les conditions d'acquisition fixe du système des performances plus élevées pour les atomes de gadolinium, d'ytterbium et de tantalum contrairement à l'or. Compte-tenu d'une balance coût/efficacité en faveur des nanoparticules à base de gadolinium (2.36 $/g de sel), de tantalum (8.92 $/g de sel) et d'ytterbium (38.20 $/g de sel) contrairement à celle des nanoparticules à base d'or (122 $/g de sel)[5], le choix aurait pu donc se porter sur au moins l'une d'entre elles. Cependant, l'atome n'est pas le seul élément important dans le choix d'une nanoparticule. En effet, les propriétés physico-chimiques sont toutes aussi importantes et nécessitent d'être optimisées et dédiées à une application spécifique comme pour le marquage macrophagique.

Dans le travail de la thèse, le choix s'est porté sur les nanoparticules pégylées d'or en raison :

**A) du coating hydrophilique** par du polyethylene glycol (PEG), limitant l' aggrégation et opsonisation dès l'injection. Cette propriété permet de prolonger le temps de circulation sanguine et par conséquent de la fenêtre de visualisation particulièrement propice aux applications cardiovasculaires comme pour l'angiographie aortique, coronarienne mais aussi comme pour la perfusion myocardique. Cela permet aussi de favoriser la captation au cours du temps par les tissus ciblés comme les macrophages mais aussi l'accumulation au sein de tissus tumoraux sièges de néoangiogénèse (effet appelé perméabilité accrue et rétention), permettant ainsi d'augmenter localement la concentration d'atomes pour une meilleure sensibilité en TDM. Cette propriété est capitale pour pouvoir palier au manque de sensibilité de l'imagerie K-edge, au même titre que la concentration en atomes des nanoparticules.

**B) du pouvoirs opacifiant** : le numéro atomique de l'atome d'or (Z=79) permet un effet photoélectrique élevé dans les gammes d'énergie utilisées en TDM entre 40 et 130 keV notamment autour de son K-edge (80.7 keV) conférant aux nanoparticules d'or une propriété d'agent de contraste en TDM mais aussi en TDM spectrale à comptage photonique (imagerie K-edge)[7].

**C) de la cyto-compatibilité *in vitro* et innocuité *in vivo*** : l'évaluation *in vitro* de la nanoparticule pégylée utilisée a retrouvé une viabilité élevée sur trois lignées cellulaires dont des macrophage de souris (J774A.1) à la fois pour des faibles et hautes doses. L'élément le plus discriminant de la toxicité était le coating et non la taille ni la concentration parmi les douze différentes nanoparticules testées [8]. Dans nos travaux, les lapins injectés n'ont d'ailleurs pas manifesté d'effets secondaires mettant en péril leur santé à court et long terme. Enfin, il faut noter que certaines nanoparticules d'or sont déjà approuvées par la FDA pour usage diagnotique et thérapeutique [9, 10].

**D) de la viscosité :** la comparaison avec un produit de contraste iodé utilisé en clinique a montré une viscosité inférieure pour la nanoparticule (1.14 ± 0.03 mPa/s versus 1.28 ± 0.18 mPa/s) permettant une injection à haut débit pour les applications vasculaires [11].

**E) du pH** : la comparaison avec un produit de contraste iodé utilisé en clinique et une solution de tampon phosphate salin a montré un pH alcalin (7.46 ± 0.05) similaire entre les trois produits, la rendant propice à l'utilisation *in vivo* [11].

**F) de la captation par les macrophages** : la comparaison *in vitro* de douze nanoparticules d'or a montré une concentration très élevée de la nanoparticule pégylée au sein de macrophages de souris (J774A.1) à 24 heures après incubation en ICP-OES contrairement aux autres nanoparticules testées (exceptée 11-MUA)[8]. Cependant l'évaluation à six mois chez le modéle animal sain a mis en évidence une rétention persistante au sein des macrophages du systéme réticulo-endothélial constituant une véritable limite avant translation chez l'homme. Cette phagocytose est principalement expliquée par le coating et le diamètre hydrodynamique de la nanoparticule de 18 nm. La clairance à court ou moyen terme de cette nanoparticule tout en conservant un ciblage macrophagique reste donc un verrou à lever.

**G) de la stabilité *in vivo* au cours du temps** : l'analyse en TEM à six mois a mis en évidence des nanoparticules de forme et taille similaires que lors de leur confection en faveur d'une stabilité au sein de la cellule après phagocytose [11].

**H) de la capacité de fabrication** : cet argument est primordial dans le choix de la nanoparticule et peut limiter l'étude de faisabilité et d'évaluation de l'imagerie K-edge chez le

moyen et gros animal. Dans le travail de thèse, plus de 70 mL de nanoparticules concentrées à 65 mgAu/mL ont été injectées sans problématique de stabilité ni de contamination pendant le stockage et lors de l'utilisation, témoignant d'une plateforme standardisée adaptée [5].
Le choix de la nanoparticule pégylée d'or nous a donc semblé être le plus judicieux et adapté à l'étude de la faisabilité de l'imagerie K-edge pour l'évaluation à la fois de la lumière artérielle et de la plaque d'athérome *in vivo* dans un modéle animal sain ou malade comme envisagé dans les travaux de thèse.

Dans le dernier travail applicatif ciblé à l'imagerie de l'athérosclérose, le modéle de lapin athéromateux utilisé présentait l'avantage de combiner 2 signes distinctifs de la pathologie artérielle athéromateuse, c'est-à-dire les modifications morphologiques et fonctionnelles de la paroi avec d'une part un épaississement pariétal, des calcifications et une disparité de calibre artériel et d'autre part une infiltration macrophagique signant les procesus inflammatoires au sein de la plaque d'athérosclérose. L'imagerie bicouleur simultanée de la lumière artérielle (opacifiée par un produit de contraste vasculaire iodé non spécifique) et de la composante inflammatoire de la plaque (marquée par les nanoparticules d'or) a conforté les résultats et perspectives précédemment avancés sur un modéle de souris apo E–KO en combinaison avec une nanoparticule HDL chargée en atomes d'or utilisant un système de TDM à comptage photonique limité à l'imagerie *ex vivo* (temps d'acquisition de 12-24 heures) [12]. La prise de contraste en imagerie K-edge a été détectée dès le premier jour mais rendue optimale le 2$^{ème}$ jour après injection, c'est-à-dire dans des temps relativement proches de ceux retrouvés en combinaison avec les nanoparticules superparamagnétiques d'oxyde de fer (USPIO) en IRM [13]. Dans le cas de notre travail, cette latence est expliquée par l'absence ou la faible captation au cours de la phase de rémanence vasculaire du produit par les macrophages (d'une durée de l'ordre de 6-12 heures)[14], ainsi que par le temps d' accumulation des nanoparticules dans les macrophages nécessaire à générer un contraste suffisant pour être détecter et quantifier en imagerie K-edge, soit une concentration autour de 1 mg/mL comme évoqué *in vitro* [4]. Dès lors, les performances de l'imagerie K-edge pour détecter les processus inflammatoires de la plaque d'athérosclérose pourraient être fortement optimisées en améliorant la sensibilité de détection mais aussi en optimisant la captation macrophagique comme l'a démontré par exemple le composant N1177 (nanoparticule crystalline à base d'iode) qui permet de réaliser une imagerie de la charge macrophagique dans la plaque à 2 heures après injection en TDM standard [15]. Cependant, l'imagerie K-edge de l'iode n'est pas possible chez l'Homme en raison du manque de photons autour de son énergie K-edge (33.3 keV). Même si l'imagerie générée par un modéle de décomposition

en eau et iode permet la visualisation de l'iode, celle-ci est limitée par la présence du calcium qui se répartit de manière quasi-équivalente dans les images des deux matériaux avec pour conséquence une surestimation de l' iode et donc de la charge macrophagique.

L'analyse histologique faite sur les plaques a confirmé la présence de gouttelettes lipidiques, de coeurs lipidiques et de macrophages spumeux confirmant la nature athéromateuse des plaques selon la classification de *Stary et al.* [16]. Les explorations en microscopie électronique ont mis en évidence la présence de nanoparticules au sein des macrophages spumeux localisés principalement dans l'intima au contact des coeurs lipidiques et non au sein de ceux contrôles supportant la présence de processus inflammatoires au sein de la plaque. Cependant, ni la caractérisation ni le ciblage des macrophages (notamment des macrophages M1) n'a été réalisé, contrairement à une précédente étude en IRM [17], pouvant limiter la signification en terme de vulnérabilité de la plaque compte-tenu de différentes voies d'activation des macrophages et de leur implication opposée, même si la répartition au sein de l'intima des macrophages est très suggestive d'une sous-population de macrophages M1. La perspective d'une imagerie moléculaire K-edge de la charge macrophagique M1 pourrait cependant être discutée.

Enfin, l'analyse des plaques en imagerie et en histologie n'a pas noté de signe de rupture comme attendu compte tenu de l'absence d' induction chimique ce qui laisse la perspective de réaliser une imagerie moléculaire K-edge de la plaque d'athérosclérose rompue après induction chimique. Cela permettrait de conforter le rôle à jouer de l'imagerie K-edge dans le domaine de l'imagerie moléculaire, et cela même avec les seuils de sensibilité actuels.

**REFERENCES**

1. Laboratoire CREATIS Projet transversal : Spectral Photon-Counting CT. Httpswwwcreatisinsa-Lyonfrsite7frprojetstransversaux
2. Mory C, Sixou B, Si-Mohamed S, et al (2018) Comparison of five one-step reconstruction algorithms for spectral CT. Phy Med Bio
3. Souhil T, sous la direction de Christian Morel (2019) Thèse: Développement de méthodes itératives pour la reconstruction en tomographie spectrale. http://www.theses.fr/2019AIXM0160
4. Si-Mohamed S, Bar-Ness D, Boussel L, Douek P (2018) Multicolor imaging with SPCCT: an in vitro study. Eur Radiol Exp 1
5. Kim J, Bar-Ness D, Si-Mohamed S, et al (2018) Assessment of candidate elements for development of spectral photon-counting CT specific contrast agents. Sci Rep 8:12119. https://doi.org/10.1038/s41598-018-30570-y
6. Greffier J, Pereira F, Hamard A, et al (2020) Effect of tin filter-based spectral shaping CT on image quality and radiation dose for routine use on ultralow-dose CT protocols: A phantom study. Diagn Interv Imaging 101:373–381. https://doi.org/10.1016/j.diii.2020.01.002
7. Dong YC, Hajfathalian M, Maidment PSN, et al (2019) Effect of Gold Nanoparticle Size on Their Properties as Contrast Agents for Computed Tomography. Sci Rep 9:14912. https://doi.org/10.1038/s41598-019-50332-8
8. Naha PC, Chhour P, Cormode DP (2015) Systematic in vitro toxicological screening of gold nanoparticles designed for nanomedicine applications. Toxicol Vitro Int J Publ Assoc BIBRA 29:1445–1453. https://doi.org/10.1016/j.tiv.2015.05.022
9. Nanospectra Biosciences, Inc. (2016) A Pilot Study of AuroLase(tm) Therapy in Patients With Refractory and/or Recurrent Tumors of the Head and Neck. clinicaltrials.gov

10. Plasmonic Nanophotothermal Therapy of Atherosclerosis - Full Text View - ClinicalTrials.gov. https://clinicaltrials.gov/ct2/show/NCT01270139. Accessed 22 Oct 2020

11. Si-Mohamed S, Cormode DP, Bar-Ness D, et al (2017) Evaluation of spectral photon counting computed tomography K-edge imaging for determination of gold nanoparticle biodistribution in vivo. Nanoscale. https://doi.org/10.1039/c7nr01153a

12. Cormode DP, Roessl E, Thran A, et al (2010) Atherosclerotic plaque composition: analysis with multicolor CT and targeted gold nanoparticles. Radiology 256:774–782. https://doi.org/10.1148/radiol.10092473

13. Sigovan M, Boussel L, Sulaiman A, et al (2009) Rapid-clearance iron nanoparticles for inflammation imaging of atherosclerotic plaque: initial experience in animal model. Radiology 252:401–409. https://doi.org/10.1148/radiol.2522081484

14. Chhour P, Naha PC, O'Neill SM, et al (2016) Labeling monocytes with gold nanoparticles to track their recruitment in atherosclerosis with computed tomography. Biomaterials 87:93–103. https://doi.org/10.1016/j.biomaterials.2016.02.009

15. Hyafil F, Cornily J-C, Feig JE, et al (2007) Noninvasive detection of macrophages using a nanoparticulate contrast agent for computed tomography. Nat Med 13:636–641. https://doi.org/10.1038/nm1571

16. Stary HC, Chandler AB, Dinsmore RE, et al (1995) A definition of advanced types of atherosclerotic lesions and a histological classification of atherosclerosis. A report from the Committee on Vascular Lesions of the Council on Arteriosclerosis, American Heart Association. Arterioscler Thromb Vasc Biol 15:1512–1531

17. Bessaad A, Sigovan M, Alsaid H, et al (2010) M1-activated macrophages migration, a marker of aortic atheroma progression: a preclinical MRI study in mice. Invest Radiol 45:262–269. https://doi.org/10.1097/RLI.0b013e3181d78030

# Outlook

L'expérience acquise ces quatre dernières années avec un système à visée préclinique laisse entrevoir de nombreuses perspectives. Tout d'abord, l'upgrade récent de notre système dans le cadre du projet européeen SPCCT H2020 par le constructeur Philips permet à ce jour de réaliser une imagerie clinique avec des protocoles d'acquisition standard (voltage : 80-120 kVp, charge : 10-300 mAs, temps de rotation : 0.33 secondes, champ de vue large : 500 mm, couverture : 176 mm). Ces possibilités techniques nous ont permis de débuter une étude de la lumière artérielle et de la plaque carotidienne chez l'Homme, avec sur les premières images conventionnelles des informations morphologiques très précises comme la visualisation de microcalcifications (réalisant parfois un aspect de poudre de microcalcifications) ou d'ulcérations sub-millimétriques avec une excellente délimitation de la lumière grâce à une image à très haute résolution (taille du voxel : 325 µm x 325 µm x 1 mm, figure ci dessous). Aussi nous allons démarré une étude pour l'évaluation de la lumière et la plaque coronarienne, en comparaison avec les méthodes d'imagerie invasives de référence (coronarographie, échographie endo-coronarienne). Cependant, ces premières études ne sont basées que sur l'utilisation de produit de contraste iodé ne mettant donc pas à profit l'imagerie K-edge.

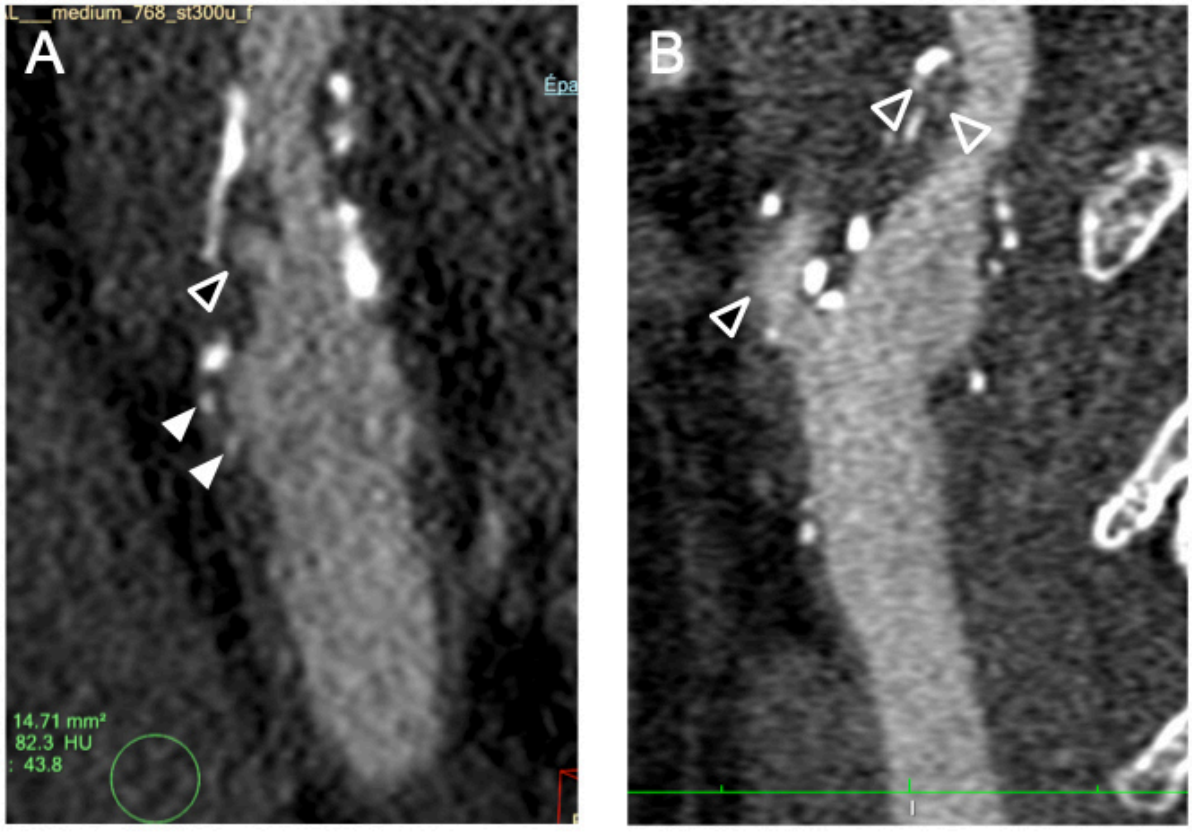


**Figure.** Imagerie conventionnelle carotidienne chez un patient de 55 ans aux antécédents d'accident cérébral vasculaire (AVC). L'imagerie à haute résolution permet la visualisation de microcalcifications (tête de flèche blanche) sans ou avec peu de blooming artefact dont

certaines sont réparties en amas voire en poudre (tête de flèche controur blanc), associées à des ulcérations (tête de flèche noire, contour blanc) signant une vulnérabilité de la plaque très probablement incriminée dans l'AVC.

Dans le cadre de l'imagerie K-edge, nos travaux *in vivo* (dont certains non publiés) ont nécessité l'injection en bolus de dix à vingt fois la dose de produit de contraste à base de gadolinium utilisés chez l'Homme (2-4 mL/kg, gadotéridol, 0.5 M) afin d'obtenir une imagerie angiographique de premier passage optimale (soit une concentration intra-aortique ~10-12 mg/mL avec un débit à 2 mL/s). Cet élément limite à ce jour leur utilisation intraveineuse chez l'Homme. Cela est expliqué non seulement par la présence de bruit significatif en imagerie K-edge mais aussi par la faible concentration en atomes des produits de contraste gadolinés (entre ~78 et ~157 mg/mL) comparativement à ceux iodinés (350 à 400 mg/mL).

Nous participons par ailleurs au développement de produits plus concentrés à base de gadolinium notamment dans le cadre du projet européen H2020. Par exemple, des études de faisabilité ont été réalisées sur le petit (souris) et moyen (lapin) animal en association avec des chélates de gadolinium hautement concentrés (gadoteridol, 1.25 M, Université de Turin)[1] et de tétraméres de Gadolinium ($Gd_4$, Université de Turin)[2]. Suite aux résultats des ces études, nous avons envisagé la fonctionnalisation des tétramères de Gadolinium avec la tropoélastine pour le marquage spécifique de la plaque athéromateuse. En effet, parmi les cibles autres que les macrophages au sein de la plaque, les fibres d'élastine au sein de la média sont de bonnes candidates, comme l'a montré le groupe de René BOTNAR (King's College London) en IRM à partir de produits dérivés d'un monomère de gadolinium fixé à l'élastine et à la tropoélastine [3, 4]. Lors des processus inflammatoires de l'athérosclérose, les fibres d'élastine au sein de la matrice extra-celllulaire présentent un catabolisme important sujet à un ciblage par l'élastine et la tropoélastine (ce dernier étant plus spécifique des fibres d'élastine), témoin d'un remodelage vasculaire marqueur de la vulnérabilité de la plaque.

De plus, l'ouverture du champ d'exploration du système nous offre la possibilité d'aborder l'imagerie du gros animal. Les premiers travaux s'intéresseront à l'imagerie K-edge de la pathologie ischémique myocardique dans un modèle d'ischémie-reperfusion chez le porc en combinaison avec des produit de contraste gadolinés approuvés cliniquement ainsi que des nanoparticules de gadolinium et d'or.

**Pour conclure,** les travaux de la thèse ont démontré la faisabilité de l'utilisation de la TDM spectrale à comptage photonique avec des agents de contraste dédiés à l'imagerie K-edge chez l'animal sain et athéromateux. Les limites de sensibilité de l'imagerie K-edge pour la détection de ces agents et de la biodistribution des nanoparticules d'or devront cependant être levées avant toute translation chez l'Homme.

**REFERENCES**

1. Si-Mohamed S, Sigovan, S, Digilio S, et al (2017) Potential for highly specific perfusion imaging using gadoteridol and K-edge Spectral Photon Counting CT. RSNA

2. Tripepi M, Capuana F, Gianolio E, et al (2018) Synthesis of High Relaxivity Gadolinium AAZTA Tetramers as Building Blocks for Bioconjugation. Bioconjug Chem 29:1428–1437. https://doi.org/10.1021/acs.bioconjchem.8b00120

3. Phinikaridou A, Andia ME, Indermuehle A, et al (2014) Vascular remodeling and plaque vulnerability in a rabbit model of atherosclerosis: comparison of delayed-enhancement MR imaging with an elastin-specific contrast agent and unenhanced black-blood MR imaging. Radiology 271:390–399. https://doi.org/10.1148/radiol.13130502

4. Phinikaridou A, Lacerda S, Lavin B, et al (2018) Tropoelastin: A novel marker for plaque progression and instability. Circ Cardiovasc Imaging 11:. https://doi.org/10.1161/CIRCIMAGING.117.007303

# Publications and Communications

**Articles in Journals**

1. Si-Mohamed S, Bar-Ness D, Boussel L, Douek P (2018) Multicolor imaging with SPCCT: an in vitro study. Eur Radiol Exp

2. Kim J, Bar-Ness D, Si-Mohamed S, et al (2018) Assessment of candidate elements for development of spectral photon-counting CT specific contrast agents. Sci Rep 8:12119. https://doi.org/10.1038/s41598-018-30570-y

3. Si-Mohamed S, Bar-Ness D, Sigovan M, et al (2017) Review of an initial experience with an experimental spectral photon-counting computed tomography system. Nucl Instrum Methods Phys Res 873:27–35. https://doi.org/10.1016/j.nima.2017.04.014

4. Cormode DP, Si-Mohamed S (first author with equal contribution), Bar-Ness D, et al (2017) Multicolor spectral photon-counting computed tomography: in vivo dual contrast imaging with a high count rate scanner. Sci Rep 7:4784. https://doi.org/10.1038/s41598-017-04659-9

5. Si-Mohamed S, Cormode DP, Bar-Ness D, et al (2017) Evaluation of spectral photon counting computed tomography K-edge imaging for determination of gold nanoparticle biodistribution in vivo. Nanoscale 9:18246–18257. https://doi.org/10.1039/c7nr01153a

6. Si-Mohamed S, Sigovan M, Hsu JC, et al (2020) In vivo molecular K-edge imaging of vulnerable atherosclerotic plaque using spectral photon-counting CT. Radiology. Under review.

7. Sigovan M, Si-Mohamed S (first author with equal contribution), Bar-Ness D, et al (2019) Feasibility of improving vascular imaging in the presence of metallic stents using spectral photon counting CT and K-edge imaging. Sci Rep 9:19850. https://doi.org/10.1038/s41598-019-56427-6

8. Mory C, Sixou B, Si-Mohamed S, et al (2018) Comparison of five one-step reconstruction algorithms for spectral CT. Phys Med Biol 63:235001. https://doi.org/10.1088/1361-6560/aaeaf2

**Book chapters**

- Chapter title « Clinical perspectives of Spectral Photon-Counting CT: PART II ».
Si-Mohamed S, Boussel L, Douek P.
Book: Spectral, Photon Counting Computed Tomography: Technology and Applications. Under the supervision of Taguchi K, Blevis I, Iniewski K CRC Press; 1st Edition. Year: 2020

- Chapter title « Caractérisation tissulaire en double et multi-énergie en imagerie cardiaque ».
Si-Mohamed S, Boussel L, OU P, Douek P. 2020 (under final review), Book: Elsevier Masson. EMC cardiologie. Year: 2020

- Chapter title « Tomodensitométrie spectrale à comptage photonique ».
Si-Mohamed S. Book: Imagerie thoracique de l'adulte, 4ème édition, sous la direction de Philippe Grenier. Year: 2018

**International Conference Proceedings**

1. [O] Non invasive specific macrophage spectral photon counting CT K-edge imaging in atherosclerosis using pegylated gold nanoparticles. Authors: Si-Mohamed S, Cormode D, Sigovan M, Breuilly M, Naha P, Carnaru M, Chalabreysse L, Coulon P, Erhard K, Daerr H, Yagil Y, Boussel L, Douek P. *5th Workshop on Medical Applications of Spectroscopic X-ray Detectors. CERN. Geneva, 2019*

2. [O] Non invasive specific macrophage spectral photon counting CT K-edge imaging in atherosclerosis using pegylated gold nanoparticles. Authors: Si-Mohamed S, Cormode D, Sigovan M, Breuilly M, Naha P, Carnaru M, Chalabreysse L, Coulon P, Erhard K, Daerr H, Yagil Y, Boussel L, Douek P. *RSNA, Chicago, 2019*

3. [P] Potential for highly specific perfusion imaging using gadoteridol and K-edge Spectral Photon Counting CT. Authors: Si-Mohamed S, Sigovan M, Bar-Ness D, Digilio G, Aime S, Poggi L, Boussel L, Douek P. *RSNA, Chicago, 2017*

4. [P] Potential for coronary K-edge imaging with Spectral Photon Counting CT. Authors: Si-Mohamed S, Perrier L, M. Sigovan, D Sigovan M, Bar-Ness D, Coulon P, Douek P, Boussel L. *RSNA, Chicago, 2017*

*5.* [O] Multi-contrast agent quantitative separation via K-edge imaging using Spectral Photon Counting CT. Authors: Bar-Ness D, Si-Mohamed S, Sigovan M, Cormode DP, Langlois JB, Naha ON, Lavenne F, Coulon P, Bartels M, Brendel B, Daerr H, Thran A, Rokni M, Roessl E, Blevis I, Boussel L, Douek P. *RSNA, Chicago, 2017*

6. [O] Noninvasive evaluation of coronary artery stenosis : in vitro comparison of a Spectral Photon Counting CT and spectral Dual Layer CT. Authors: Coulon P, Si-Mohamed S, Bar-Ness D, Sigovan M, Vlassenbrok A, Boussel L, Douek P. *RSNA, Chicago, 2017*

7. [O] Initial experience in improving stent analysis and intra stent lumen assessment using Spectral Photon Counting CT and K-edge imaging. Authors: Sigovan M, Bar-Ness D, Si-Mohamed S, Langlois JB, Coulon P, Bartels M, Brendel B, Daerr H, Thran A, Rokni M, Roessl E, Blevis I, Douek P, Boussel L. *RSNA, Chicago, 2017*

*8.* [O] In vivo quantitative dynamic angiography with gold nanoparticles and Spectral Photon Counting CT. Authors : Si-Mohamed S, Cormode DP, Sigovan M, Bar-Ness D, Langlois JB, Naha ON, Lavenne F, Coulon P, Bartels M, Brendel B, Daerr H, Thran A, Rokni M, Roessl E, Blevis I, Boussel L, Douek P. *RSNA, Chicago, 2016*

**9.** [O] In vivo quantification of gold nanoparticles biodistribution kinetics with Spectral Photon Counting CT via K-edge imaging. Authors : Si-Mohamed S, Cormode DP, Sigovan M, Bar-Ness D, Langlois JB, Naha ON, Lavenne F, Coulon P, Bartels M, Brendel B, Daerr H, Thran A, Rokni M, Roessl E, Blevis I, Boussel L, Douek P.*RSNA, Chicago, 2016*

**National Conference and Meetings**

**1.** [O] Potentiel du scanner spectral à comptage photonique pour l'imagerie vasculaire en présence de stents metalliques. Authors: Sigovan M, Si-Mohamed S Bar-Ness D, Langlois JB, Coulon P, Bartels M, Brendel B, Daerr H, Thran A, Rokni M, Roessl E, Blevis I, Douek P, Boussel L. *Journées Françaises de la Radiologie, Paris, 2017*

2. [O] Evaluation de l'imagerie K-edge avec un scanner spectral à comptage photonique pour la détermination de la distribution de nanoparticules d'or in vivo. Authors: Si-Mohamed S, Cormode DP, Bar-Ness D, Sigovan M, Coulon P, Roessl E, Blevis I, Douek P, Boussel L. *Journées Françaises de la Radiologie, Paris, 2017*

3. [O] Potentiel de la méthode dite de k-edge pour l'imagerie coronarienne en scanner spectral à comptage photonique. Authors: Si-Mohamed S, Perrier L, M. Sigovan, D Sigovan M, Bar-Ness D, Coulon P, Douek P, Boussel L. *Journées Françaises de la Radiologie, Paris, 2017*

4. [O] Discrimination quantitative de multiple agents de contraste avec un scanner spectral à comptage photonique. Authors: Si-Mohamed S, Bar-Ness D, Sigovan M, Coulon P, Roessl E, Blevis I, Altman A, Cormode D, Gelgamire J, Boussel L, Douek P. *Journées Françaises de la Radiologie, Paris, 2017*

*5.* [O] Angiographie k-edge dynamique quantitative de nanoparticules d'or par scanner spectral à comptage photonique in vivo. Authors: Si-Mohamed S, Garrivier T, Cormode DP, Sigovan M, Bar-Ness D, Naha PC, Coulon P, Boussel L, Douek P. *Journées Françaises de la Radiologie, Paris, 2017*

[O] Oral communication
[P] Poster presentation**.**